



TECHNISCHE
UNIVERSITÄT
WIEN

Vienna University of Technology

DISSERTATION

Measurements of prompt J/ψ and $\psi(2S)$ production and polarization at CMS

ausgeführt zum Zwecke der Erlangung des akademischen Grades einer Doktorin
der technischen Wissenschaften unter der Leitung von

UNIV.DOZ. DIPL.-ING. DR.TECHN. CLAUDIA-ELISABETH WULZ

und

DR. JOSEF STRAUSS

als verantwortlich mitwirkender Assistent

am Institut für Hochenergiephysik (HEPHY)
der Österreichischen Akademie der Wissenschaften (ÖAW)
und am Atominstitut (E141)

eingereicht an der

TECHNISCHEN UNIVERSITÄT WIEN
FAKULTÄT FÜR PHYSIK

von

DIPL.-ING. ILSE KRÄTSCHMER

Matrikelnummer: 0525179

Wien, am 11. Mai 2015

Kurzbeschreibung

Quarkonia bestehen aus einem schweren Quark und dem entsprechenden Antiquark. Sie sind daher das einfachste System, um die Bildung eines gebundenen Zustandes aus Quarks durch die starke Wechselwirkung zu untersuchen. In der Nicht-Relativistischen QuantenChromodynamik (NRQCD), einem von QCD inspirierten Modell, werden die Entstehung eines Quark-Antiquark-Paares und die darauf folgende Entwicklung des Paares zu einem gebundenen Zustand getrennt voneinander behandelt. Diese Aufspaltung in zwei Schritte wird als NRQCD Faktorisierung bezeichnet. Sie ist auf den Vergleich mit experimentellen Ergebnissen angewiesen, da die Entwicklung des anfänglichen Quark-Antiquark-Paares zu einem gebundenen Zustand nicht störungstheoretisch berechnet werden kann.

Diese Dissertation beschreibt die Messungen der Produktionswechselwirkungsquerschnitte und Polarisierungen der prompten J/ψ und $\psi(2S)$ Mesonen, welche gebundene $c\bar{c}$ -Zustände sind, die entweder direkt oder über einen kurzlebigen Zwischenzustand entstanden sind. Die Messungen basieren auf Daten, die in Proton-Proton-Kollisionen mit einer Schwerpunktsenergie von 7 TeV im Jahr 2011 am CMS Experiment am LHC aufgezeichnet wurden. Die Wechselwirkungsquerschnitte der prompten J/ψ und $\psi(2S)$ Mesonen wurden in vier äquidistanten Rapiditätsintervallen sowie in einem weiteren Rapiditätsbereich, $|y| < 1.2$, gemessen. Dabei wurden vier unterschiedliche Polarisierungen (bevorzugte Spinausrichtungen) berücksichtigt. Die Wirkungsquerschnitte wurden bis zu einem transversalen Impuls, p_T , von 120 GeV (J/ψ) bzw. 100 GeV ($\psi(2S)$) bestimmt. Zusätzlich wurde das Verhältnis der zwei Wechselwirkungsquerschnitte zueinander untersucht.

Die Polarisierung wird immer in Bezug auf ein Referenzsystem gemessen. Insgesamt drei verschiedene dieser Referenzsysteme (HX, CS, PX) wurden gewählt, in denen die Polarisierung der prompten J/ψ und $\psi(2S)$ Mesonen als Funktion von p_T und $|y|$ bestimmt wurde. Zusätzlich wurde auch eine vom System unabhängige Methode angewandt. Die Messungen wurden bis zu $p_T = 70$ GeV im Fall des J/ψ und 50 GeV für das $\psi(2S)$ durchgeführt. Es wurde keine starke Polarisierung gemessen, was im Widerspruch zu den Berechnungen der NRQCD steht, die bei hohem p_T eine starke transversale Polarisierung vorhersagen.

Die Ergebnisse von CMS über die Produktion von Quarkonia haben erheblich zum Verständnis der Bildung von gebundenen Zuständen aus schweren Quarks beigetragen, insbesondere da sie eine kinematische Region austesten, wo die NRQCD Faktorisierung als zuverlässig angesehen wird.

Abstract

Quarkonia, bound states of a heavy quark and its antiquark, are the ideal probe to study how quarks form bound states via strong interactions. Non Relativistic QuantumChromodynamics (NRQCD) is a QCD inspired model that factorizes the production of a bound state into two steps: the creation of the initial quark-antiquark pair and the transformation of the initial pair to a bound state. The NRQCD factorization approach relies on experimental data to describe the non-perturbative evolution of the initial pair to a bound state.

This thesis describes the measurements of the production cross sections and polarizations of the prompt J/ψ and $\psi(2S)$ mesons, which are $c\bar{c}$ states that are produced either directly or via the decay of a short-lived intermediate state. The measurements are based on a dimuon data sample collected by the CMS experiment at the LHC in proton-proton collisions at $\sqrt{s} = 7$ TeV, corresponding to a total integrated luminosity of 4.9 fb^{-1} . The prompt J/ψ and $\psi(2S)$ production cross sections are determined in four equidistant rapidity ranges as well as over a wider integrated rapidity interval of $|y| < 1.2$. Four different polarization (preferred spin alignment) scenarios are considered. The cross sections have been measured up to transverse momenta, p_T , of 120 GeV and 100 GeV for the J/ψ and $\psi(2S)$, respectively, thereby tremendously extending the p_T reach of previous CMS measurements. Moreover, the ratio of $\psi(2S)$ to J/ψ cross sections was explicitly determined.

Polarization is always measured with respect to a reference frame. The polarizations of the prompt J/ψ and $\psi(2S)$ mesons are determined in three reference frames (HX, CS, PX) as functions of p_T and $|y|$. In addition, a frame-invariant approach is applied. The results are obtained in two (three) rapidity bins and extend up to $p_T = 70$ (50) GeV in case of the J/ψ ($\psi(2S)$). The measured polarization values are close to zero, showing no evidence of any strong polarization. This is in disagreement with existing NRQCD calculations that predict strong transverse polarization, especially at high p_T values.

The quarkonium results provided by CMS have significantly contributed to improve the understanding of hadron formation, especially because they probe the theoretical calculations in a kinematic region where NRQCD factorization is believed to be most reliable.

ACKNOWLEDGEMENTS

I would like to thank my supervisors Claudia Wulz for her guidance and support, and Jožko Strauss for his calm and realistic view of life. I am also very grateful to my masters' thesis advisor Chris Fabjan, who paved the way for my work in particle physics.

I thank Anna Lipniacka for kindly revising this thesis, as well as for being the friendly constantly smiling chair(wo)man during my first presentation in the community of particle physics.

I want to thank my colleagues at HEPHY, in particular Valentin Knünz for being the best possible colleague at all times; Wolfgang Adam for his support, inputs and feedback; Johannes Brandstetter for having been a good minion; Robert Schöfbeck, Wolfgang Waltenberger and Wolfgang Kiesenhofer for their help with seemingly unsolvable problems; Rudi Frühwirth for his insights in statistics; Herbert Rohringer for his unique insights in physics and life; and Erica Brondolin, Ece Aşilar and Elena Ginina for many inspiring lunch hours.

I also want to thank Pietro Faccioli, Carlos Lourenço, João Seixas and Hermine Wöhri for the numerous fruitful discussions, lots of patience and all the beautiful and charming hours we enjoyed in Geneva, Lisbon and Vienna.

I thank the Austrian Science Fund (FWF) for funding me (project number: P 24167), so I could go to the most amazing places around the world and talk about my work.

I owe endless thanks to my family and friends, who provided numerous opportunities to not work on my Ph.D.; in particular to Elke and Gotti for our garden and my parents for giving me all possible opportunities.

Most importantly, I want to thank Thomas for making me coffee every morning and for coping with my zombie-like behaviour in the mornings.

CONTENTS

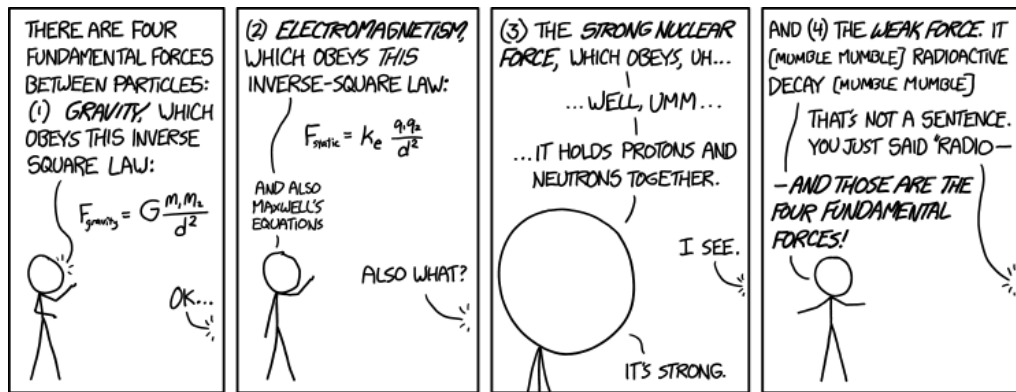
1	Introduction	1
2	Quarkonium physics	5
2.1	Quarkonium production	8
2.1.1	Color Singlet Model	10
2.1.2	NRQCD factorization approach	10
2.1.3	Fragmentation function approach	11
2.2	Quarkonium polarization	12
2.3	Importance of understanding quarkonium production	18
3	Experimental setup	21
3.1	The Large Hadron Collider	21
3.1.1	LHC performance	23
3.1.2	Physics at the LHC	23
3.2	The Compact Muon Solenoid	24
3.2.1	Inner tracking system	26
3.2.2	Calorimeter	26
3.2.3	Superconducting magnet	28
3.2.4	Muon system	28
3.2.5	Data acquisition and triggering	30
3.2.6	Muon reconstruction and identification	33
3.2.7	CMS detector performance	35
4	Prompt $\psi(nS)$ polarizations	37
4.1	Event selection	38
4.1.1	Online selection	38

4.1.2	Offline selection	38
4.1.3	Phase-space coverage	41
4.1.4	Definition of the kinematic cells of the measurement	41
4.2	Single muon and dimuon efficiencies	41
4.2.1	Single muon efficiencies	44
4.2.2	Efficiency of the dimuon vertex fit χ^2 probability requirement	45
4.2.3	Muon pair correlations	46
4.3	Polarization framework	48
4.4	Fit to mass and pseudo-proper decay length	52
4.4.1	Mass fit	53
4.4.2	Pseudo-proper decay length fit	54
4.4.3	B-fractions	60
4.5	Background model	60
4.6	Systematic uncertainties	64
4.6.1	Uncertainty on the framework	66
4.6.2	Uncertainty on the background model	67
4.6.3	Uncertainty due to the TnP model	67
4.6.4	Uncertainty due to the parametrization of the single muon efficiencies	67
4.6.5	Uncertainty due to the efficiency of the dimuon vertex fit χ^2 probability requirement	67
4.6.6	Uncertainty related to the muon pair correlations	67
4.6.7	Uncertainty due to the definition of the prompt signal region	68
4.6.8	Summary of systematic uncertainties	68
4.7	Cross-checks	68
4.8	Results	71
5	Prompt $\psi(nS)$ cross sections	75
5.1	Definition of the kinematic cells of the measurement	76
5.2	Single muon and dimuon efficiencies	76
5.2.1	Efficiency of the dimuon vertex fit χ^2 probability requirement	76
5.2.2	Muon pair correlations	77
5.3	Acceptance	78

5.4	Fit to mass and pseudo-proper decay length	79
5.4.1	Free and fixed parameters	80
5.4.2	B-fractions	85
5.4.3	Fit to mass and pseudo-proper decay length for $ y < 1.2$	87
5.5	Systematic uncertainties	87
5.5.1	Uncertainties on the extraction of the prompt signal yield	87
5.5.2	Uncertainties due to the TnP approach	91
5.5.3	Uncertainties on the parametrization of the single muon efficiencies	91
5.5.4	Uncertainties related to the muon pair correlations	93
5.5.5	Summary of the systematic uncertainties	95
5.5.6	Systematic uncertainties for $ y < 1.2$	95
5.6	Results	97
5.6.1	Ratio of $\psi(2S)$ to J/ψ cross sections	99
6	Discussion of results	101
6.1	Prompt $\psi(nS)$ polarization	101
6.2	Prompt $\psi(nS)$ production cross sections	105
6.2.1	Ratio of $\psi(2S)$ to J/ψ cross sections	108
6.3	Impact of the results	108
7	Conclusions	111
7.1	Summary	111
7.2	Outlook	113
	Bibliography	115
	Acronyms	123
	List of figures	127
	List of tables	131
	Curriculum Vitae	133

CHAPTER 1

INTRODUCTION



<http://xkcd.com/1489/>

The strong force binds quarks into nucleons that build up the atomic nuclei and thus keeps our visible world together at the innermost level. The fundamental understanding of how the strong force forms bound states is, however, still lacking. The simplest system to study the formation of bound states are quarkonia, particles that consist of a heavy quark-antiquark pair ($c\bar{c}$, $b\bar{b}$).

Quarkonium production is best described within Non Relativistic Quantum Chromodynamics (NRQCD) [1], a model inspired by QCD. Since the quarks are heavy, the production of a bound quarkonium state is conjectured to proceed in two steps, which is referred to as NRQCD factorization: the creation of the initial quark-antiquark pair at short distances, which can be calculated in the context of perturbative QCD, and the non-perturbative long-distance transformation of the initial pair to a bound state.

Before the precise measurements of the $\psi(nS)$ and Υ production cross sections at the Tevatron, the production of quarkonia was believed to proceed through a color-neutral quark-antiquark pair. The results from CDF [2] triggered the hypothesis that also the contributions coming from colored pairs are significant and cannot be neglected. While the cross sections were well described by including the color-octet contributions, the measured isotropic quarkonium polarization (preferred spin alignment) [3, 4, 5, 6, 7] did not agree with the theoretical predictions of a large transverse polarization, a situation often denoted as *quarkonium polarization puzzle*. Moreover, the polarization results were found to be inconsistent when comparing the different experiments. This triggered the development of an improved methodology making use of the full polarization information provided in data [8, 9, 10, 11, 12]. The advent of large LHC data samples in combination with this improved analysis methodology offered perfect conditions to finally solve the quarkonium puzzle and provide a clear experimental picture of quarkonium polarization. The CMS experiment at the LHC is particularly well suited for studies of quarkonium production cross sections and polarizations because of its high transverse momentum coverage, its efficient identification of interesting quarkonium events and its excellent ability to resolve the momentum of quarkonium decay products as well as the associated vertex.

The CMS experiment has published several highly recognized results on quarkonium physics. In this thesis, two of the numerous results are discussed: the production cross sections and the polarizations of prompt J/ψ and $\psi(2S)$ mesons. The results have been obtained in a team effort, involving scientists from CERN, the Institute of High Energy Physics (HEPHY) in Vienna, the Laboratory of Instrumentation and Experimental Particle Physics (LIP) in Lisbon and Beijing University. They were extensively scrutinized by the full CMS Collaboration. The prompt $\psi(nS)$ polarization was published in Ref. [13]. The prompt $\psi(nS)$ production cross section was accepted for publication by *Phys. Rev. Lett.* on April 13, 2015.

My work on the prompt $\psi(nS)$ polarizations included the development of the mass and pseudo-proper decay length fits as well as the background model, the calculation of the data-driven systematic uncertainties and carrying out some of the cross checks. Concerning the prompt $\psi(nS)$ production cross section measurement, I was the leading analyst responsible for the full analysis procedure. Moreover, I determined single muon identification and trigger efficiencies using the J/ψ as well as the Z resonance, not only in the context of the analyses presented in this thesis [14], but also as a general service to the CMS collaboration [15].

Chapter 2 introduces the concept of quarkonia, their production and polarization and the current experimental and theoretical situations. The LHC and the CMS experiment are described in Chapter 3. In Chapters 4 and 5, the measurements of the prompt J/ψ and $\psi(2S)$ production cross sections and polarizations are explained in detail. Chapter 6 discusses the results and their impact on the description of quarkonium production.

Note that σ denotes the standard deviation in this thesis, unless it is explicitly stated to represent the cross section.

CHAPTER 2

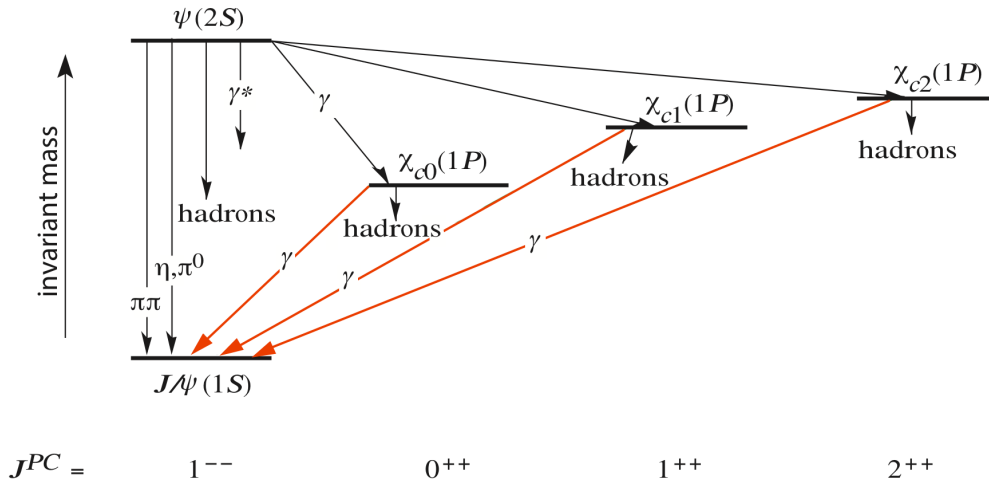
QUARKONIUM PHYSICS

We live in a wonderful world that is full of beauty, charm and adventure.

– Jawaharlal Nehru

Quarkonia are strongly bound states of a heavy quark and its antiquark, i.e. $c\bar{c}$ (charmonium) and $b\bar{b}$ (bottomonium) states. Top quarks cannot form quarkonium states due to their large masses. They decay electroweakly before a bound state can form. The first quarkonium state to be found was the J/ψ , which was discovered in 1974 by two separate groups [16, 17] and proved the existence of the charm quark. Shortly afterwards, the bottom counterpart, the $\Upsilon(1S)$, was discovered [18].

Quarkonia are characterized by the quantum numbers for spin S , the orbital angular momentum L and the total angular momentum $J = S + L$. The possible configurations are referred to as J^{PC} , where P represents the parity of the quarkonium, $P = (-1)^{L+1}$ and C is the charge conjugation, $C = (-1)^{L+S}$. They can also be identified in the spectroscopic notation by $n^{2S+1}L_J$, where n is the principal quantum number. Figure 2.1 displays the charmonium and bottomonium spectra, showing only the subset of quarkonium states and decays relevant to this thesis. The shown mesons are CP -even, J^{++} and J^{--} , with a mass below the open charm and beauty thresholds. They can be divided into S-wave ($L = 0$) and P-wave ($L = 1$) states. The S-wave states are $J^{PC} = 1^{--}$ vector mesons: the J/ψ and its radial excitation $\psi(2S)$, sometimes also called ψ' , in case of the charmonium; and the $\Upsilon(1S)$ with its radial excitations $\Upsilon(2S)$ and $\Upsilon(3S)$ in case of the bottomonium. The two charmonium states, J/ψ and $\psi(2S)$, are denoted by $\psi(nS)$ with $n = 1, 2$ while the three bottomonium states, $\Upsilon(1S)$, $\Upsilon(2S)$ and $\Upsilon(3S)$, are denoted by $\Upsilon(nS)$ with $n = 1, 2, 3$. The P-wave states are J^{++} pseudovector mesons with $J = 0, 1, 2$, denoted by χ_{cJ} in case of the charmonium and $\chi_{bJ}(1P)$ and its radial excitations $\chi_{bJ}(2P)$ and $\chi_{bJ}(3P)$ in case of the bot-



(a) Charmonium spectrum

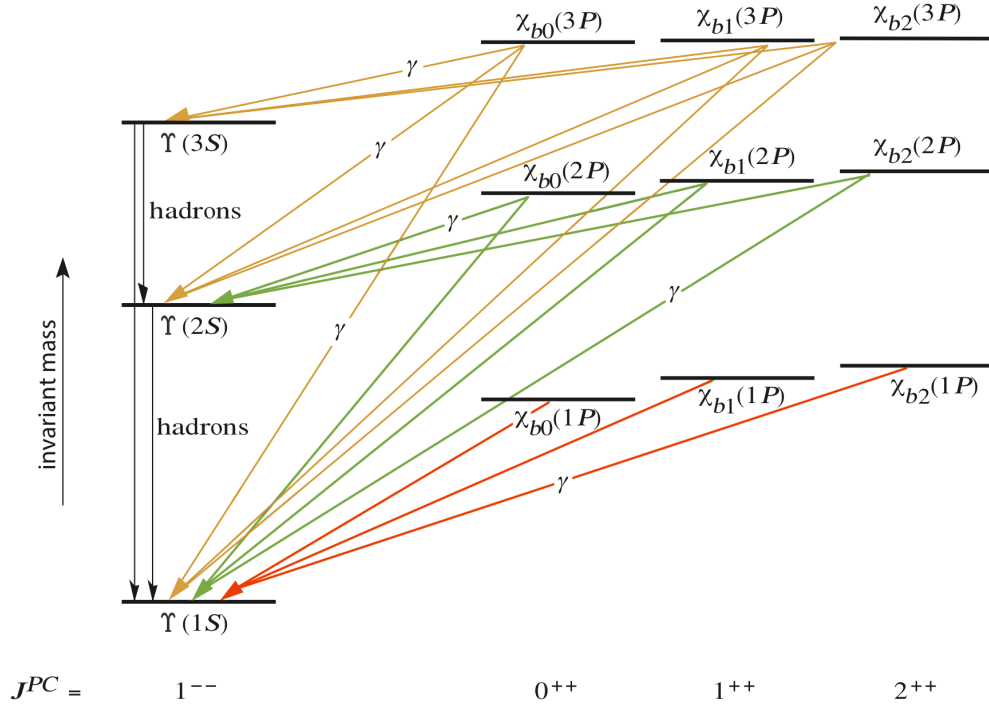
(b) Bottomonium spectrum: Note that the triplet structure of the $\chi_b(3P)$ states has not yet been experimentally established.

Figure 2.1: Quarkonium spectra showing only the relevant subset of quarkonium states (adapted from [19]): (a) Charmonium spectrum and decay modes, (b) bottomonium spectrum and decay modes. The vertical axis represents the invariant mass of the states.

tomonium. The P-wave states can decay into the S-wave states by radiating a photon.

A large fraction of the J/ψ 's produced in hadron-hadron collisions originate from the decay of heavier charmonium states. Since the lifetime of the parent state is small, these feed-down contributions together with the directly produced J/ψ 's, form the so-called prompt component of the J/ψ . About 67% of the prompt J/ψ 's are directly produced at low p_T while about $8.1 \pm 0.3\%$ come from the $\psi(2S)$ and $25 \pm 5\%$ from the χ_{cJ} states [20].

Additionally, J/ψ 's can be produced in decays from b-hadrons with average decay times of the order of 10^{-12} s [19]. The $\psi(nS)$'s originating from these decays can be identified easily through the secondary vertex, displaced from the primary vertex by an average distance of the order of $10^2 \mu\text{m}$. This contribution is called the nonprompt component.

In case of the bottomonium, there is no delayed production mechanism, but the structure of feed-down contributions is more complicated due to the increased number of states. Figure 2.2 shows the magnitude of the feed-down fractions from the P-wave to the S-wave bottomonium states, recently measured by LHCb [21]. Quite surprisingly, the fraction of $\Upsilon(3S)$ mesons coming from $\chi_b(3P)$ states is measured to be around 40%. The $\Upsilon(3S)$ was regarded as almost feed-down free before.

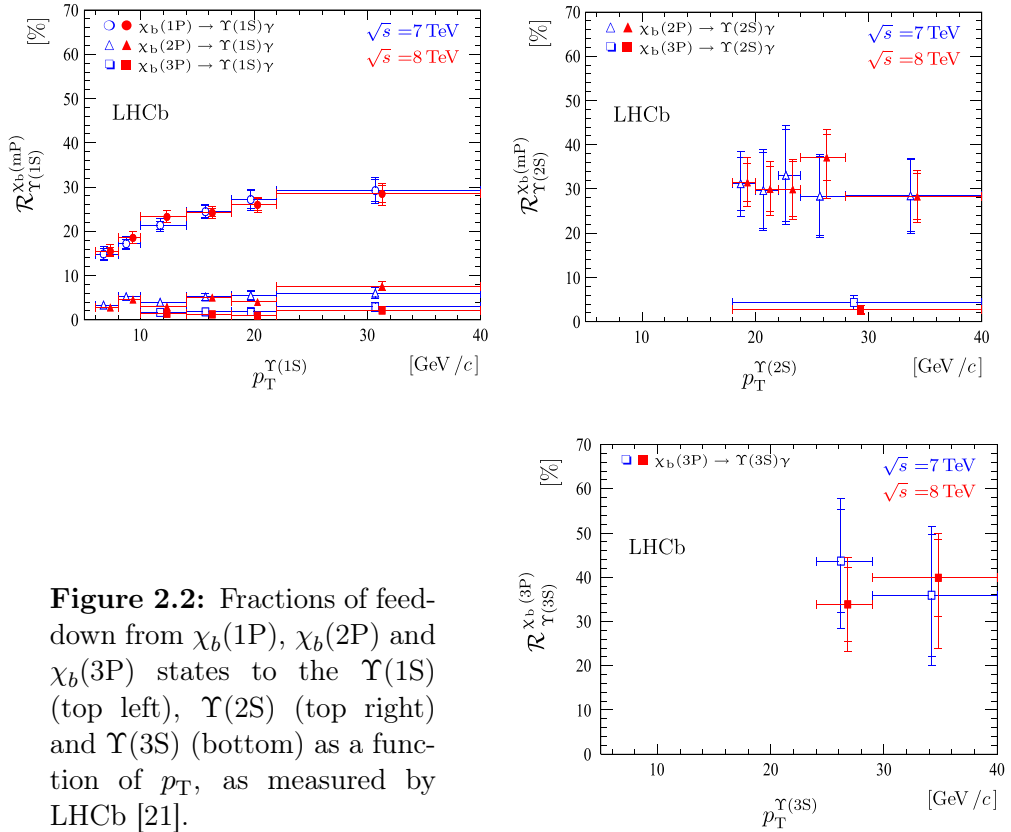


Figure 2.2: Fractions of feed-down from $\chi_b(1P)$, $\chi_b(2P)$ and $\chi_b(3P)$ states to the $\Upsilon(1S)$ (top left), $\Upsilon(2S)$ (top right) and $\Upsilon(3S)$ (bottom) as a function of p_T , as measured by LHCb [21].

Table 2.1: Properties of quarkonium mesons [19].

Meson	J^{PC}	$n^{2S+1}L_J$	Mass [MeV]	Full Width
J/ψ	1^{--}	1^3S_1	$3\,096.916 \pm 0.011$	92.9 ± 2.8 keV
$\chi_{c0}(1P)$	0^{++}	1^3P_0	$3\,414.75 \pm 0.31$	10.3 ± 0.6 MeV
$\chi_{c1}(1P)$	1^{++}	1^3P_1	$3\,510.66 \pm 0.07$	0.86 ± 0.05 MeV
$\chi_{c2}(1P)$	2^{++}	1^3P_2	$3\,556.20 \pm 0.09$	1.97 ± 0.11 MeV
$\psi(2S)$ or ψ'	1^{--}	2^3S_1	$3\,686.09 \pm 0.04$	304 ± 9 keV
$\Upsilon(1S)$	1^{--}	1^3S_1	$9\,460.30 \pm 0.26$	54.02 ± 1.25 keV
$\chi_{b0}(1P)$	0^{++}	1^3P_0	$9\,859.44 \pm 0.42 \pm 0.31$	-
$\chi_{b1}(1P)$	1^{++}	1^3P_1	$9\,892.78 \pm 0.26 \pm 0.31$	-
$\chi_{b2}(1P)$	2^{++}	1^3P_2	$9\,912.21 \pm 0.26 \pm 0.31$	-
$\Upsilon(2S)$	1^{--}	2^3S_1	$10\,023.26 \pm 0.31$	31.98 ± 2.63 keV
$\chi_{b0}(2P)$	0^{++}	2^3P_0	$10\,232.50 \pm 0.40 \pm 0.50$	-
$\chi_{b1}(2P)$	1^{++}	2^3P_1	$10\,255.46 \pm 0.22 \pm 0.50$	-
$\chi_{b2}(2P)$	2^{++}	2^3P_2	$10\,268.5 \pm 0.22 \pm 0.50$	-
$\Upsilon(3S)$	1^{--}	3^3S_1	$10\,355.20 \pm 0.50$	20.32 ± 1.85 keV
$\chi_b(3P)$	-	-	$10\,534.0 \pm 9.0$	-

The polarization and production mechanisms of the χ states can be very different from the ones of the directly produced S-wave quarkonia because of their different parity and angular momentum properties.

The properties of the mesons shown in Fig. 2.1 are summarized in Table 2.1.

The leptonic decay modes of J/ψ ($\psi(2S)$) have a branching ratio of about 5.9% (7.9%) for the dimuon as well as the dielectron channel. For $\Upsilon(1S)$, the corresponding branching ratios are 2.4% for the dielectron decay and 2.5% for the dimuon decay [19]. This thesis focuses on the production and polarization of $\psi(nS)$ states decaying into $\mu^+\mu^-$. The next sections on quarkonium production and polarization will therefore mainly discuss the charmonium case.

2.1 Quarkonium production

Quarks and their interactions are described by the theory of strong interactions, Quantum Chromodynamics (QCD). As only heavy and thus slow (non-relativistic) quarks are involved, Non Relativistic (NR) QCD is used. A quarkonium has several different intrinsic scales: the heavy quark mass m_Q ; the momentum of the heavy quark in the quarkonium rest frame of the order of $m_Q v$, where v is the relative velocity of the heavy quark inside the quarkonium ($v^2 \approx 0.3$ for J/ψ and $v^2 \approx 0.1$ for the Υ); and the binding energy $m_Q v^2$ [22]. Quarkonium production is assumed to proceed in two steps as shown in Fig. 2.3. First, a heavy quark-antiquark ($Q\bar{Q}$) pair is produced, which occurs at the scale m_Q . The initial $Q\bar{Q}$ pair, which can either be color-neutral and/or carry color depending on the production model, then evolves into the physically observable color-neutral

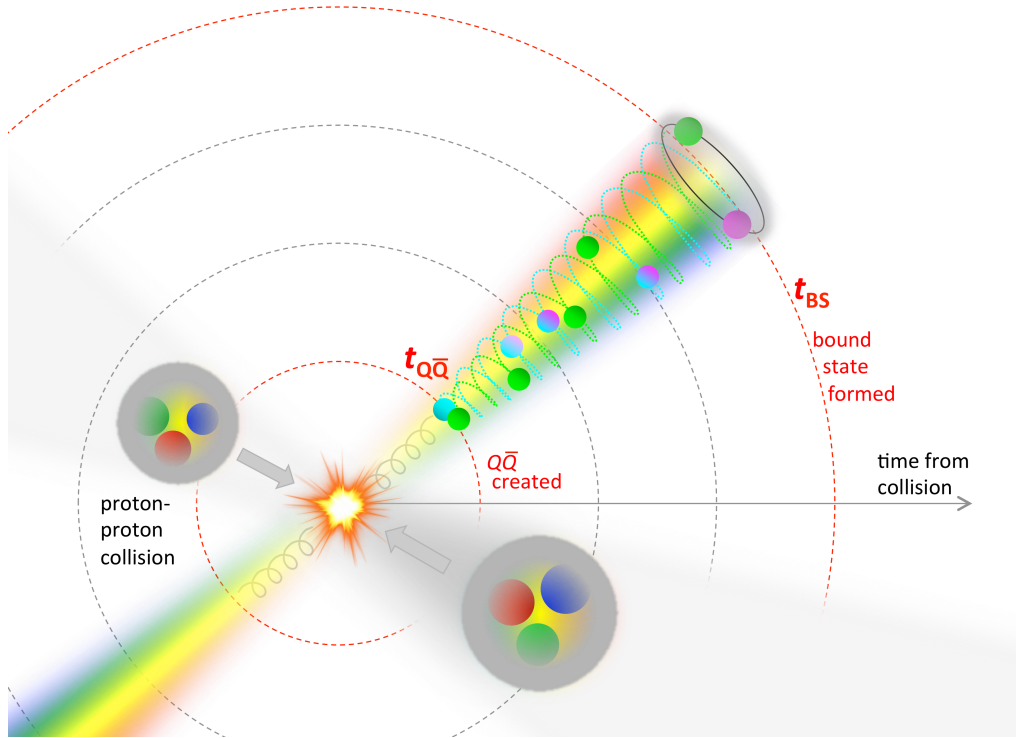


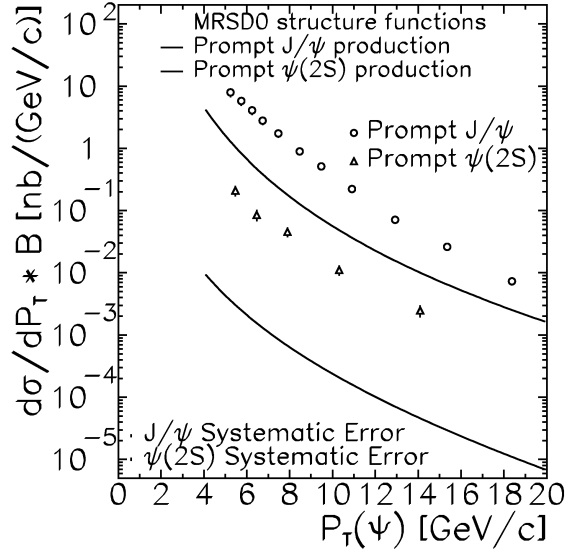
Figure 2.3: The two steps of quarkonium production. The initial $Q\bar{Q}$ pair is created at time $t_{Q\bar{Q}}$ shortly after the collision of the color-neutral protons, consisting of three quarks. The $Q\bar{Q}$ pair then evolves to a bound state whose formation happens at a very different timescale, t_{BS} . The initial pair shown here carries color charge (green and anti-red/cyan) and transforms to a physically observable color-neutral (green and anti-green/magenta) state. The remaining energy of the colliding protons not used for the creation of the $Q\bar{Q}$ pair is shown as colored jets [23].

quarkonium state, \mathcal{Q} , which involves the scales $m_Q v$ and $m_Q v^2$. The first step can be calculated perturbatively while the second one involves non-perturbative physics. The quarkonium therefore enables the testing and understanding of the interplay between the perturbative and non-perturbative regimes and the formation of strongly bound states [22].

There are several theoretical models proposed to describe quarkonium production. Only the following will be discussed here:

- Color Singlet Model (CSM)
- NRQCD factorization approach
- Fragmentation function approach

Figure 2.4: Prompt J/ψ and $\psi(2S)$ differential cross sections times branching ratios for $|y| < 0.6$, as measured by CDF, in comparison to CSM predictions [2].



2.1.1 Color Singlet Model

Until the 1990's, quarkonium production was believed to be reasonably well described by the CSM [24], where the observable quarkonium has the same spin and orbital momentum quantum numbers (color-singlet) as the initially produced ($Q\bar{Q}$) pair. The CSM is not only theoretically inconsistent, but also does not describe the measured cross sections. Figure 2.4 shows that there is a large discrepancy between the prompt J/ψ and $\psi(2S)$ production cross sections measured by the Collider Detector at Fermilab (CDF) experiment at the Tevatron [2] and the CSM predictions for directly produced $\psi(nS)$. The difference in the J/ψ cross section could be attributed to the feed-down contributions from decays of the heavier quarkonium states. The $\psi(2S)$ state, however, is unaffected by feed-down decays and shows a factor 50 higher cross section than calculated by the CSM. This large discrepancy was dubbed the *CDF $\psi(2S)$ anomaly*.

2.1.2 NRQCD factorization approach

In 1995, Bodwin, Braaten and Lepage [1] developed the presently widely accepted, but not yet fully proven NRQCD factorization approach. In this effective field theory, the quarkonium can either evolve from a color-singlet $Q\bar{Q}$ pair with identical quantum numbers L and S to the final bound quarkonium state or from color-octet states. The quarkonium production cross section $\sigma(\mathcal{Q})$ is described by the factorization

$$\sigma(\mathcal{Q}) = \sum_n \mathcal{S}[Q\bar{Q}(n)] \cdot \langle \mathcal{O}^{\mathcal{Q}}(n) \rangle, \quad (2.1)$$

with $n = {}^{2S+1}L_J^{[c]}$, where c is the color multiplicity ($c = 1, 8$).

The cross section is thus factorized into Short-Distance Coefficients (SDCs), $\mathcal{S}[Q\bar{Q}(n)]$, describing the production of the initial $Q\bar{Q}$ pair, and the Long-Distance Matrix Elements (LDMEs), $\langle\mathcal{O}^{\mathcal{Q}}(n)\rangle$, which give the probability that a bound state is formed. The SDCs are kinematics-dependent functions calculable in perturbative QCD. They correspond to inclusive partonic cross sections given in expansions of the strong coupling constant α_s convolved with parton distribution functions for the colliding hadrons and are therefore process-dependent.

The LDMEs are non-perturbative and thus cannot be calculated. They must be determined by comparisons to measurements of quarkonium production cross sections and polarizations. The color-singlet matrix element corresponding to the leading order of v can, however, be extracted phenomenologically from an electromagnetic decay rate. It is important to realize that if only this color-singlet state in the expansion is considered, the CSM is obtained. The CSM is therefore a special case of NRQCD.

The LDMEs are conjectured to be constant, i.e. independent of the $Q\bar{Q}$ momentum, and universal, i.e. process-independent. They scale with powers of v . The factorization can therefore be seen as a double expansion in α_s and v . The expansion in v is truncated at order v^4 and is more accurate for the bottomonium than the charmonium since v^2 is smaller by a factor of 1/3. The series may converge more slowly for excited states as the relative velocity in an excited quarkonium is larger than in the ground state [25]. The truncation results in three independent color-octet LDMEs $\langle\mathcal{O}^{\mathcal{Q}}(^1S_0^{[8]})\rangle$, $\langle\mathcal{O}^{\mathcal{Q}}(^3S_1^{[8]})\rangle$ and $\langle\mathcal{O}^{\mathcal{Q}}(^3P_J^{[8]})\rangle$, which are suppressed by the order v^4 for the S-wave quarkonia [26]. In the case of the higher mass χ states, only one color-octet LDME, $\langle\mathcal{O}^{\mathcal{Q}}(^3S_1^{[8]})\rangle$, contributes at v^4 .

The factorization is proven to hold up to Next-to-Next-to-Leading Order (NNLO), but not for all orders in α_s , which is very important since α_s associated with soft gluons is significant [22]. Existing proofs of the factorization require transverse momenta to be larger than the quarkonium mass, $m_{\mathcal{Q}}$.

The NRQCD factorization approach seemed to reproduce the CDF charmonium production cross sections well. However, when fixing the LDMEs by fitting the cross section measurements and then predicting the quarkonium polarizations, the NRQCD factorization approach was not successful, as discussed in Sect. 2.2.

2.1.3 Fragmentation function approach

In the fragmentation function approach [27, 28, 29], cross sections for producing quarkonia at $p_{\text{T}} \gg m_{\mathcal{Q}}$ are written as a sum of perturbative single-parton production cross sections convolved with single-parton fragmentation functions [30]. The proof for this factorization is outlined in Ref. [28]. The parton production cross sections include all information on the incoming state and are reorganized in terms of $m_{\mathcal{Q}}/p_{\text{T}}$. The fragmentation functions correspond to non-perturbative probability distributions of the actual transformation of a heavy quark pair into a quarkonium, which have to be determined phenomenologically.

The fragmentation function approach alone lacks predictive power. The fragmentation functions are therefore expressed in the context of the NRQCD framework as a sum of the perturbative QCD fragmentation functions and a finite number of NRQCD LDMEs [25].

The reorganization of the cross section in terms of m_Q/p_T provides a systematic method for resumming perturbative logarithms that are potentially large.

2.2 Quarkonium polarization

The quantum numbers of the initial $Q\bar{Q}$ pair strongly influence the formation of the final bound state, as can be seen in Eqn. 2.1. Conclusions on the properties of the initial $Q\bar{Q}$ pair can be drawn from the alignment of the total angular momentum vector \vec{J} with respect to a certain quantization axis z . The spin alignment or polarization is reflected in the angular decay distribution of the quarkonium in its rest frame.

In case of vector particles, such as the S-wave quarkonium states with $J = 1$, there are three possible J_z eigenstates: $J_z = -1, 0, +1$. A single elementary production subprocess can be described by the superposition of these three eigenstates [9]

$$|\mathcal{Q}\rangle = a_{-1}|-1\rangle + a_0|0\rangle + a_{+1}|+1\rangle, \quad (2.2)$$

where a_{-1} , a_0 and a_{+1} are the component amplitudes.

Applying the basic principles of helicity and parity conservation and rotation invariance leads to the angular decay distribution

$$W(\cos\vartheta, \varphi|\vec{\lambda}) \propto \frac{1}{(3 + \lambda_\vartheta)} (1 + \lambda_\vartheta \cos^2\vartheta + \lambda_\varphi \sin^2\vartheta \cos 2\varphi + \lambda_{\vartheta\varphi} \sin 2\vartheta \cos\varphi), \quad (2.3)$$

where $\vec{\lambda} = (\lambda_\vartheta, \lambda_\varphi, \lambda_{\vartheta\varphi})$ represent the frame-dependent polarization parameters and ϑ and φ are the polar and azimuthal angles of the positively charged muon, μ^+ , with respect to the z -axis of the chosen reference frame [9]. The definition of ϑ and φ is illustrated in Fig. 2.5.

The x - z -plane of the reference frame corresponds to the production plane spanned by the momenta of the colliding beams, \vec{b}_1 and \vec{b}_2 , as shown in Fig. 2.6-left. The y -axis is defined to be along the direction of the cross-product of the momentum vectors of the colliding beams, $\vec{b}_1 \times \vec{b}_2$, as seen in the quarkonium rest frame. In this thesis, three reference frames are considered, which are defined by a specific choice in the orientation of the z -axis in the production plane: the Helicity (HX) frame in which the z -axis coincides with the direction of the quarkonium momentum; the Collins-Soper (CS) frame [31] in which the z -axis coincides with the direction of the relative velocity of the colliding beams in the quarkonium rest frame; and the Perpendicular Helicity (PX) frame [32] in which the z -axis is perpendicular to the CS axis. Their definition is illustrated in Fig. 2.6-right. At high transverse momentum, p_T , and mid-rapidity, the HX and CS frames are perpendicular to each other; the PX frame coincides with the HX frame. At p_T close to zero and forward rapidity, the HX and CS frames coincide.

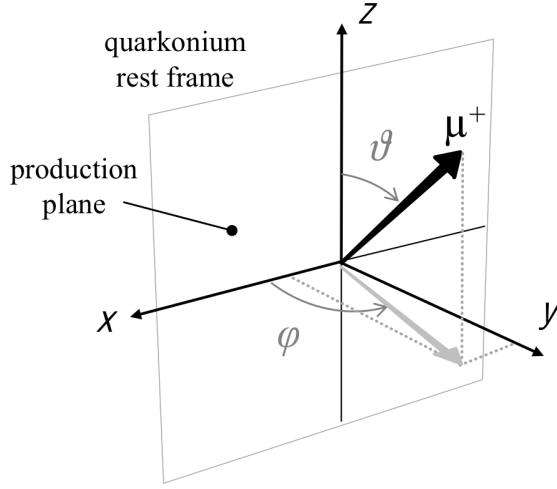


Figure 2.5: Definition of the polar and azimuthal angles ϑ and φ with respect to a quantization axis z [9]: It is the convention to use the positive muon, μ^+ , to define the angles.

When the eigenstate J_z equals ± 1 , fully transverse polarization ($\lambda_\vartheta = 1$, $\lambda_\varphi = 0$ and $\lambda_{\vartheta\varphi} = 0$) is obtained, which corresponds to a peanut-shaped angular decay distribution. The eigenstate $J_z = 0$ results in a fully longitudinal polarization ($\lambda_\vartheta = -1$, $\lambda_\varphi = 0$ and $\lambda_{\vartheta\varphi} = 0$) and a doughnut-shaped angular distribution. The angular distributions of the two extreme cases and the corresponding polarization parameters are shown in Fig. 2.7. The unpolarized distribution is isotropic with all polarization parameters equal to zero. However, there is no combination of a_{-1} , a_0 and a_{+1} such that λ_ϑ , λ_φ and $\lambda_{\vartheta\varphi}$ are all zero. This means that the angular decay distribution can never be intrinsically isotropic. Only a lucky mixture of subprocesses can lead to a cancellation of all three observed polarization parameters [9].

When more than one subprocess contributes to the production mechanism, such as in the case of mesons that are either directly produced or produced in feed-

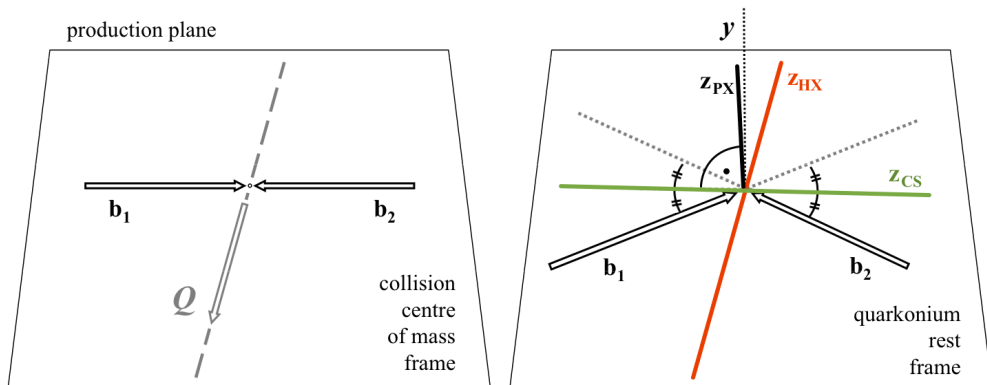


Figure 2.6: Definition of the production plane (left) and the polar axis of the reference frames HX, CS and PX (right). The y -axis of the frames is always perpendicular to the production plane defined by the colliding beams \vec{b}_1 and \vec{b}_2 in the quarkonium rest frame [9].

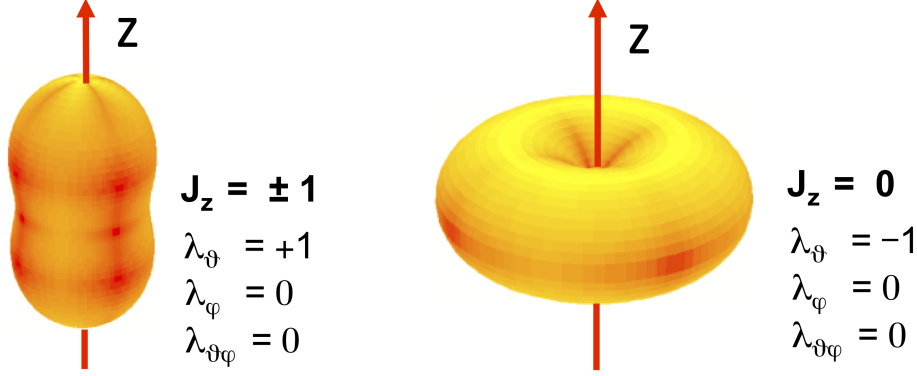


Figure 2.7: Fully transverse (left) and fully longitudinal (right) angular decay distributions with respect to the quantization axis z [9].

down decays, the most general observable angular decay distributions can be written as a weighted sum over the distributions of the different subprocesses [9].

As the polar anisotropy parameter λ_θ never exceeds the value 1 in any reference frame, constraints for the other parameters can be deduced

$$|\lambda_\varphi| \leq \frac{1}{2}(1 + \lambda_\theta) \text{ and} \quad (2.4)$$

$$|\lambda_{\theta\varphi}| \leq \frac{1}{2}(1 - \lambda_\varphi). \quad (2.5)$$

This implies that $|\lambda_\varphi| \leq 1$ and $|\lambda_{\theta\varphi}| \leq \frac{\sqrt{2}}{2}$ [9, 12, 33]. Figure 2.8 shows the constraints to the phase-space for quarkonia coming from feed-down decays or from any origin.

The polarization parameters λ_θ , λ_φ and $\lambda_{\theta\varphi}$ change depending on the kinematics and therefore also on the reference frame. Indeed, the measured polarization can show a kinematic dependence due to the fact that the chosen reference frame does not coincide with the natural frame, where λ_θ is maximal and λ_φ and $\lambda_{\theta\varphi}$ are equal to zero. This dependence does not reflect the underlying production physics, but is an artifact associated to the reference frame chosen in the measurement.

Additional parameters not depending on the reference frame can be defined. They enable the distinction between the intrinsic kinematic dependence and the one introduced by the measurement. A common frame-invariant quantity is $\tilde{\lambda}$,

$$\tilde{\lambda} = \frac{\lambda_\theta + 3\lambda_\varphi}{1 - \lambda_\varphi}. \quad (2.6)$$

It characterizes the shape of the angular decay distribution, which is independent of the chosen reference frame. Apart from complementing the information that is given by the three frame-dependent parameters, $\tilde{\lambda}$ is also invaluable as a

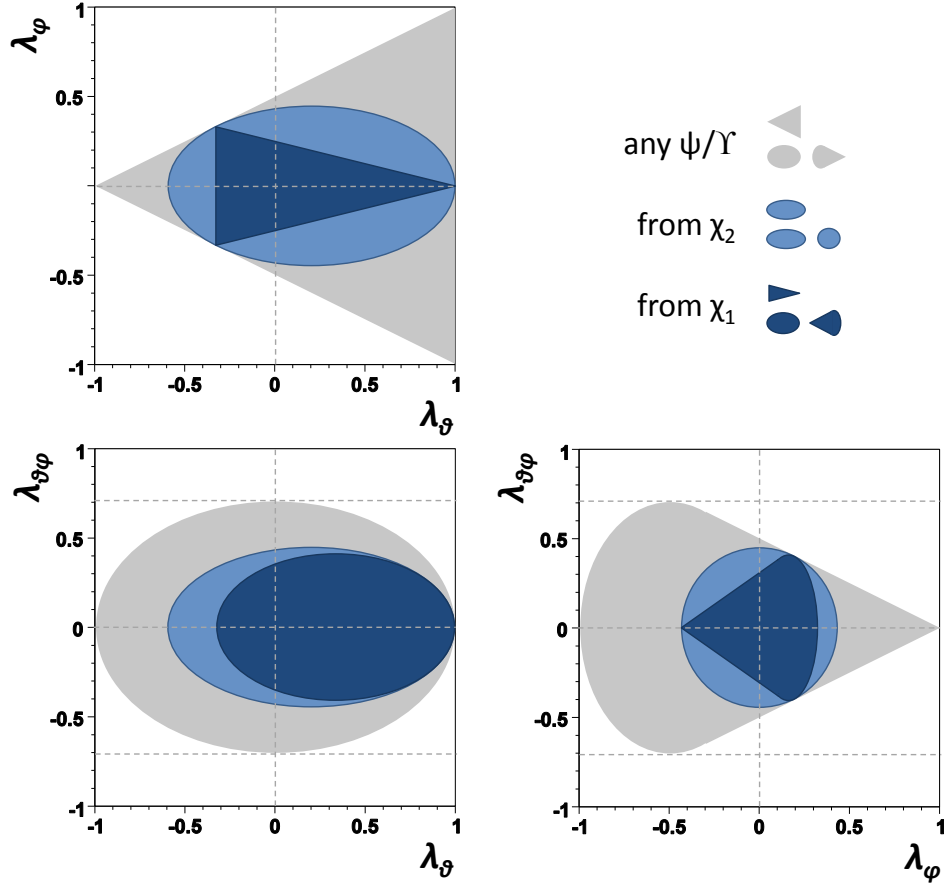


Figure 2.8: Allowed phase-space regions of the polarization parameters in case of the dilepton decay of quarkonium states of any origin (gray), coming from χ_2 (light blue) and coming from χ_1 decays (dark blue) [33].

systematic check. The comparison of $\tilde{\lambda}$ in different reference frames can reveal systematic effects beyond those already accounted for.

In the pre-LHC era, only a fraction of the information available from data was determined. Usually, the λ_ϑ parameter alone in only one reference frame was measured, which led to inconsistent and incomplete results. Figure 2.9-left shows the λ_ϑ parameter for J/ψ measured by CDF in two run periods [3, 4]. The discrepancy between the results cannot be explained by the slight difference in center-of-mass energy from Run I to Run II or the slightly different rapidity regions. Also in case of the $\Upsilon(1S)$, shown in Fig. 2.9-right, the discrepancy between the CDF [6] and $D0$ experiments [7] cannot be attributed to the difference in rapidity coverage.

Moreover, these polarization measurements did not agree with the, then state-of-the-art, Leading Order (LO) NRQCD predictions [34], as is shown in Fig. 2.10-left for the J/ψ . The large discrepancy between data and theory was dubbed the *polarization puzzle*.

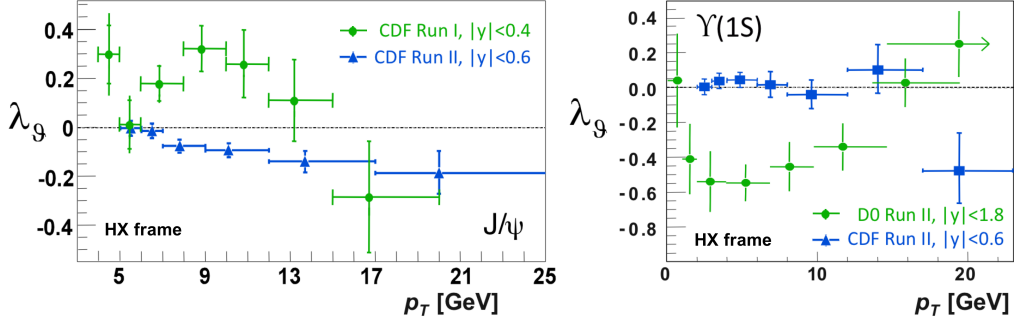


Figure 2.9: Polarization parameter λ_g for the prompt J/ψ (left) and the $\Upsilon(1S)$ (right) states in the HX frame, measured by the CDF [3, 4, 6] and D0 [7] experiments.

One attempt to solve the puzzle was to extend the LO to Next-to-Leading Order (NLO) NRQCD calculations [36, 37, 38, 39, 40, 41, 35]. The discrepancy remained as shown in Fig. 2.10-right. Given that the measurements were inconsistent, the discrepancy was always attributed to the experimental results [9].

The methodology discussed here was put forward in a series of papers [8, 9, 10, 11, 12] aimed at solving the quarkonium puzzle. The same formalism can also be applied to the measurements of the polarization of P-wave states with $J = 0, 1, 2$ as is shown in Ref. [33]. For not too low momentum, the χ polarization can be measured directly from the angular distribution of the dilepton decay in the rest frame of the S-wave state. The methodology has led to a new understanding of quarkonium production as well as consistent measurements of quarkonium polarization, as can be seen for the case of the $\Upsilon(nS)$ states in Fig. 2.11. No significant polarization is observed. The results are in good agreement with the NLO NRQCD calculations [43] in case of the $\Upsilon(1S)$ and $\Upsilon(2S)$ states, as shown in Fig. 2.12. The $\Upsilon(3S)$ mesons, however, show some discrepancy between the experimental results and the theoretical calculations. In case of the $\Upsilon(1S)$

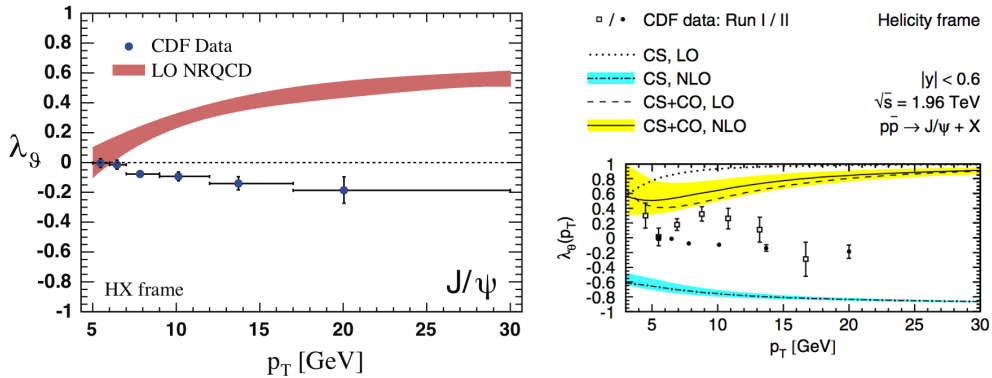


Figure 2.10: Polarization parameter λ_g for the prompt J/ψ in the HX frame, measured by CDF [3], compared to LO [34] (left) and NLO (right) NRQCD predictions [35].

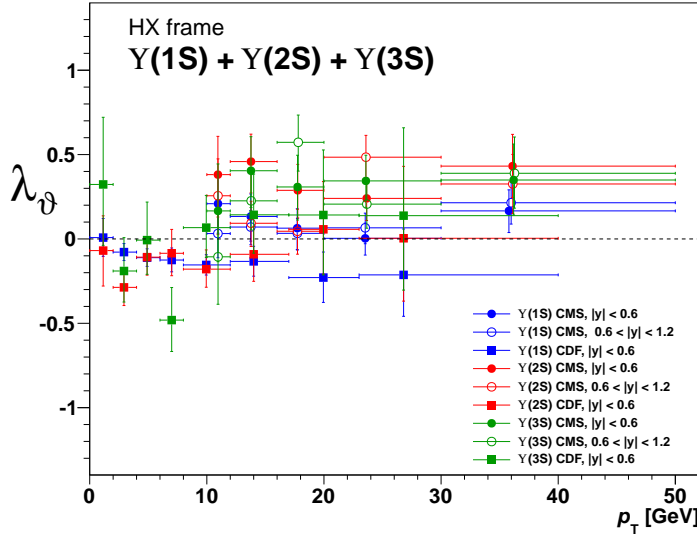


Figure 2.11: Polarization parameter λ_θ in the HX frame, measured by CMS [42] and CDF [6], in case of the $\Upsilon(nS)$ states.

and $\Upsilon(2S)$ states, the feed-down contributions are included in the theoretical calculations, but not in case of the $\Upsilon(3S)$. These contributions have not been measured and therefore introduce additional free parameters in the fit that is performed to obtain the LDMEs. This additional freedom results in a much better agreement of the prediction for the $\Upsilon(3S)$ with data [44].

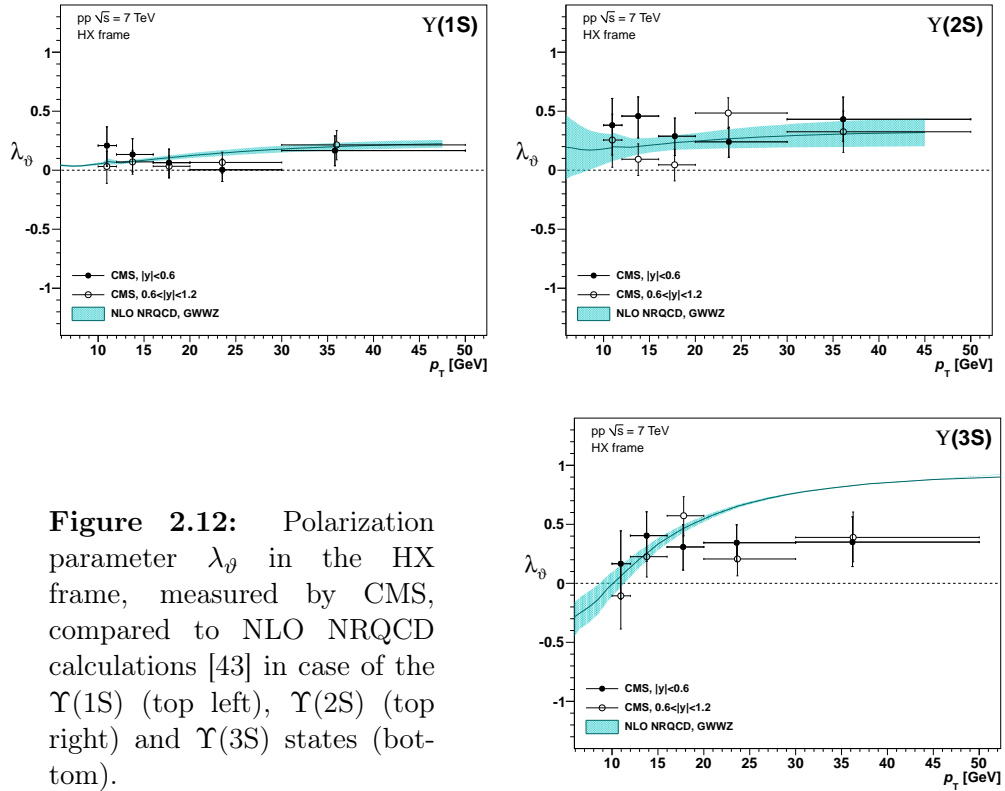


Figure 2.12: Polarization parameter λ_θ in the HX frame, measured by CMS, compared to NLO NRQCD calculations [43] in case of the $\Upsilon(1S)$ (top left), $\Upsilon(2S)$ (top right) and $\Upsilon(3S)$ states (bottom).

2.3 Importance of understanding quarkonium production

Quarkonium production addresses fundamental issues of QCD since it allows for the study of the interplay between the short-distance and long-distance strong force scales. While the short-distance QCD processes can reliably be calculated with perturbative methods, quantitative studies of long-distance QCD are rare and extremely difficult. The only way to understand the long-distance effects and how quarks form strongly bound states is via the study of quarkonium production, where the perturbative and non-perturbative regimes can be separated.

The NRQCD factorization approach is the most successful theory in describing quarkonium production. The theory is dependent on experimental inputs as the LDMEs can only be determined by comparison to data. The NRQCD factorization is not proven to all orders of α_s and relies on the experiment to prove or disprove the factorization in absence of further theoretical progress. Once the complete independence of the bound-state formation process from the creation mechanism of the initial $Q\bar{Q}$ pair is firmly established by studying quarkonium cross sections and polarizations in different processes, such as in photoproduction or in association with other particles, quarkonium production can be used to understand other processes.

The process $H \rightarrow J/\psi + \gamma$ is considered the golden channel for the direct measurement of the Higgs coupling to the charm quark. A measurement of the $Hc\bar{c}$ coupling is possible with the high luminosity upgrade of the LHC, where the luminosity will be increased by a factor of 10 beyond its design value by 2020. It can test whether the Higgs boson couples to the second generation quarks with the strength predicted by the Standard Model (SM). Figure 2.13-left displays the relative deviation in the branching ratio $H \rightarrow J/\psi + \gamma$ as a function of the scaling parameter κ_c that describes the deviation of the charm quark coupling to the Higgs boson from the SM values. The variation in the branching ratio can reach 100% for values of κ_c a few times the SM value, which is experimentally very promising [45].

In case of $Hb\bar{b}$ coupling, the branching ratio $H \rightarrow \Upsilon(1S) + \gamma$ deviates by a large amount for values of κ_b that are only slightly shifted from the SM value of unity. The rate of the $H \rightarrow \Upsilon(1S) + \gamma$ process in the SM is far too small to be observed at the high luminosity LHC, meaning that any observed events would indicate new physics beyond the SM [45].

However, if the mechanism of the bound state formation of a S-wave quarkonium state is not the same when it is produced on its own or in association with a photon, no conclusions can be drawn from the measurement of $H \rightarrow Q + \gamma$.

Quarkonium production in nuclear collisions is considered a crucial instrument to probe the Quark-Gluon Plasma (QGP) formation. According to QCD, hadronic matter undergoes a phase transition to a deconfined quark and gluon state, QGP,

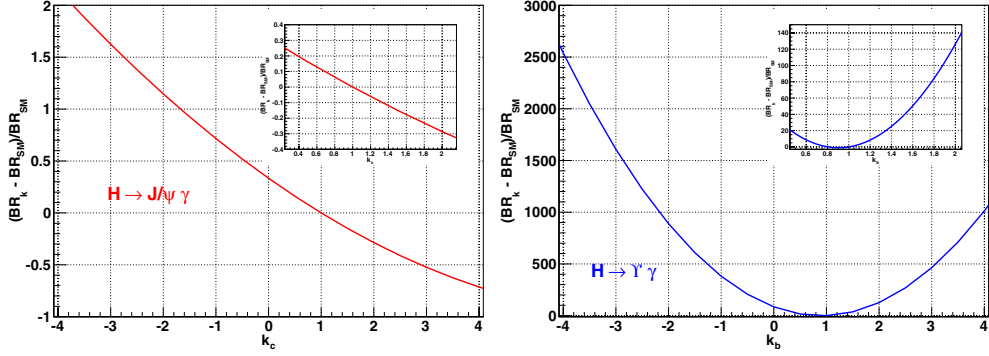


Figure 2.13: Relative deviations in the branching ratio H to $J/\psi + \gamma$ (left) and $\Upsilon(1S) + \gamma$ (right) as function of the scaling parameter κ_Q that describes the deviation of the heavy-quark couplings to the Higgs boson from their SM values [45].

above a certain temperature. This is possible to study experimentally in heavy ion collisions.

The production of strongly bound quarkonia is prohibited if the initial $Q\bar{Q}$ is created in a deconfined environment. Since the bound-state formation still remains possible in peripheral collisions, the production of quarkonia is only strongly suppressed [46]. The magnitude of suppression depends on the binding energy of the state. Higher quarkonium excitations dissolve at a lower temperature, leading to characteristic melting patterns that were predicted by assuming, among other things, specific mechanisms of quarkonium production [47].

The level of quarkonium melting has to be measured with respect to a clean baseline, the proton-proton (pp) collisions, to be able to disentangle the initial from the final state effects [48]. A good understanding of the quarkonium production in pp collisions will therefore help to interpret the results from heavy ion collisions.

CHAPTER 3

EXPERIMENTAL SETUP

A theory is something nobody believes, except the person who made it. An experiment is something everybody believes, except the person who made it.

– Albert Einstein

The analyses presented in this thesis are performed with data taken in pp collisions at the CMS experiment at the LHC. This chapter introduces the LHC and CMS, as well as the CMS detector systems, data acquisition chain and reconstruction software that are relevant for the analyses discussed in this thesis. Further details on the LHC and CMS can be found in Refs. [49, 50, 51, 52].

3.1 The Large Hadron Collider

The Large Hadron Collider (LHC) is the world's biggest and most powerful particle collider with a nominal center-of-mass energy $\sqrt{s} = 14$ TeV for pp collisions. It is located at the European Organization for Nuclear Research, known as Conseil Européen pour la Recherche Nucléaire (CERN), near Geneva. The LHC tunnel has a circumference of 26.7 km and is situated 45 to 170 m underground crossing the Swiss-French border. The LHC uses two separate superconducting rings and a twin-bore or *two-in-one* magnet design to steer the counter rotating proton beams in a close space. It accelerates and collides proton beams up to $\sqrt{s} = 14$ TeV as well as lead ions with a design energy of $\sqrt{s} = 2.76$ TeV/nucleon [49]. Since this thesis is based on data taken in pp collisions, all processes will be described for protons, but are equally true for lead ions.

The LHC is the last part in a long chain of accelerators which is shown in Fig. 3.1. The proton source, a bottle of hydrogen, is located at one end of the Linear ACcelerator (LINAC2). The protons are accelerated up to 50 MeV in the LINAC2

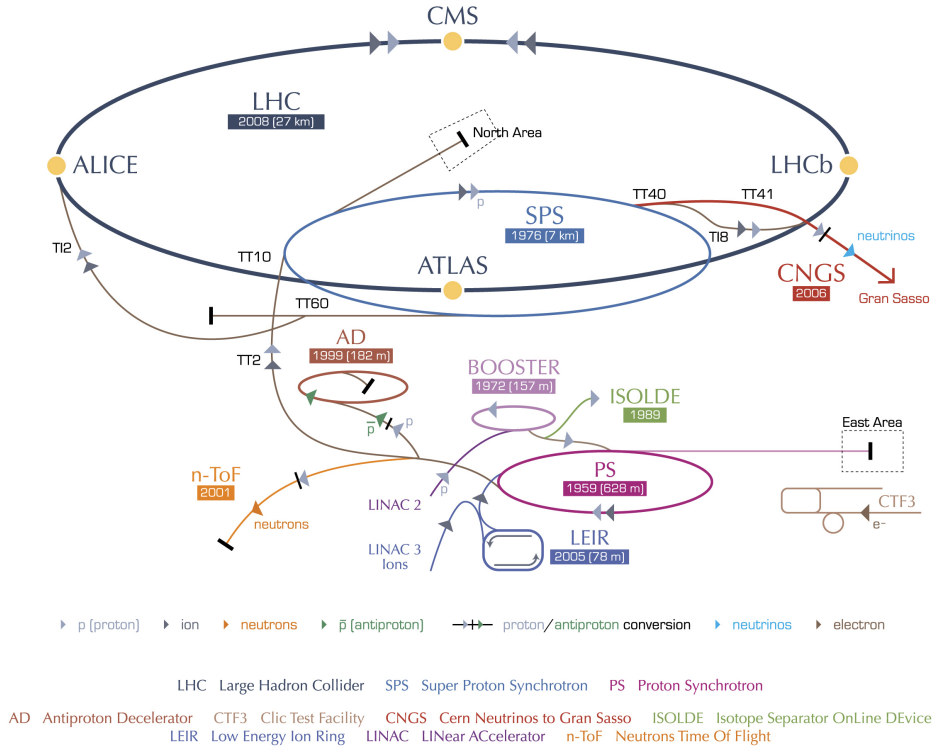


Figure 3.1: CERN accelerator complex. The protons start in the LINAC2, move through the PSB, the PS and SPS before they are injected into the LHC where they are brought to collision [53].

before they are injected into the Proton Synchrotron Booster (PSB). At the energy of 1.4 GeV, they are transferred to the Proton Synchrotron (PS). Here, proton bunches are formed with the correct spacing for the LHC (nominally 25 ns). The protons are further accelerated to 25 GeV before they are fed to the Super Proton Synchrotron (SPS). The SPS requires three to four cycles of the PS to be filled. The protons are then injected into the LHC at an energy of 450 GeV. The filling of the LHC requires twelve SPS cycles and follows a certain scheme to ensure the correct beam structure needed for beam dumping, calibration and synchronization. The LHC further accelerates the proton bunches up to a maximum energy of 7 TeV and makes them collide in four interaction points [49].

A detector is located at each interaction point: There are two general purpose experiments, A Toroidal LHC ApparatuS (ATLAS) and the Compact Muon Solenoid (CMS). They cover a wide range of physics topics. The Large Hadron Collider beauty experiment (LHCb) experiment is focused on b-physics while A Large Ion Collider Experiment (ALICE) is built for heavy ion collisions to explore the first moments of the universe.

Table 3.1: LHC parameters during Run I and their design values [54].

Parameter	2010	2011	2012	Design value
Beam energy [TeV]	3.5	3.5	4	7
Bunch spacing [ns]	150	50	50	25
Max. number of bunches	368	1380	1380	2808
Max. bunch intensity (protons per bunch)	1.2×10^{11}	1.45×10^{11}	1.7×10^{11}	1.15×10^{11}
Peak luminosity [$\text{cm}^{-2}\text{s}^{-1}$]	2.1×10^{32}	3.7×10^{33}	7.7×10^{33}	1×10^{34}

3.1.1 LHC performance

The LHC started with the first pp collisions at the energy of 3.5 TeV per beam in March 2010 and ended the so-called *Run I* with protons at the end of 2012 with $\sqrt{s} = 8$ TeV. The following two years, the LHC as well as the other accelerators were shut down for maintenance and upgrade work. The accelerator chain up to the SPS was restarted mid 2014. In May 2015, the LHC begins taking physics data again at $\sqrt{s} = 13$ TeV.

The number of events generated in LHC collisions per second for a process with a given cross section σ_p is denoted as

$$\mathcal{R}_p = \mathcal{L} \times \sigma_p \quad (3.1)$$

where \mathcal{L} is the luminosity. The luminosity is one of the most important parameters of an accelerator. It depends only on the beam parameters and is given by

$$\mathcal{L} = \frac{N_b^2 n_b f \gamma_r}{4\pi \varepsilon_n \beta^*} F, \quad (3.2)$$

where N_b represents the number of particles per bunch, n_b the number of bunches per beam, f the revolution frequency, γ_r is the relativistic gamma factor, ε_n the normalized transverse emittance, β^* the betatron function at the collision point and F the geometric luminosity reduction factor due to the crossing angle at the interaction point [49]. The nominal luminosity at the LHC is $10^{34} \text{ cm}^{-2}\text{s}^{-1}$.

The integrated luminosity measures the data size collected over time. The LHC delivered 0.04 fb^{-1} in 2010 and 5.6 fb^{-1} in 2011 at $\sqrt{s} = 7$ TeV. In 2012, the LHC ran at $\sqrt{s} = 8$ TeV and provided an integrated luminosity of 23 fb^{-1} (about 1 fb^{-1} per week).

The most important parameters of the LHC during Run I and their design values are summarized in Tab. 3.1.

3.1.2 Physics at the LHC

Our current understanding of the universe is encapsulated in the SM of particle physics which describes the fundamental particles and the force carriers. Even

though the SM has been very successful in explaining and predicting experimental results, the theory is incomplete and unable to account for certain phenomena such as dark matter or neutrino masses.

The LHC was built to probe the SM and look for signs of physics Beyond the Standard Model (BSM). The LHC experiments conduct precision measurements of the SM to better constrain its parameters and understand SM processes and backgrounds. Moreover, these precision measurements can be used to look for tiny deviations from SM predictions that might hint at new physics. A recent example is the angular analysis of $B \rightarrow K^* \mu^+ \mu^-$ performed by LHCb that is in tension with the SM prediction at a level of 3.7σ [55].

Additionally, direct searches for BSM are performed such as searches for supersymmetric particles, new massive vector bosons, extra dimensions and dark matter. So far, no signs of new physics have been observed. But physicists feel confident that the next long pp run will bring some expected and unexpected discoveries, in particular after the success of Run I.

The SM was rediscovered by the LHC experiments with higher precision than previous experiments in a very short time after the start-up of the LHC. In December 2011, the discovery of the first new SM particle at the LHC was announced by ATLAS: the excited quarkonium state $\chi_b(3P)$ [56]. The most anticipated result of the LHC is however the first observation of the long-sought after Higgs boson at the mass of 125 GeV by the ATLAS [57] and CMS collaborations [58]. The new data taken this year will help clarify and precisely probe the exact properties of the discovered Higgs boson.

3.2 The Compact Muon Solenoid

The Compact Muon Solenoid (CMS) is a multipurpose particle physics experiment designed to study a wide range of physics topics. As the name of the experiment already implies, the focus when designing the detector lay on a good muon identification and momentum resolution. The detector has a length of 21.6 m, a diameter of 14.6 m and weighs 12 500 t [52]. Figure 3.2 shows the overall layout of CMS. The silicon-based tracking system is the heart of the detector. It is surrounded by the electromagnetic and hadronic calorimeters and a 3.8 T field solenoid. The outermost part of the detector are the muon chambers consisting of different layers of muon detection systems.

Each subsystem of the CMS detector is specifically designed to exploit different properties of the particles to measure energy and momentum. The inner tracking system accurately measures the positions and momenta of charged particles while the calorimeters determine their energies: Electrons and photons are stopped in the electromagnetic calorimeter; hadrons are contained within the hadron calorimeter. Muons are detected in the muon chambers. Thus, all particles leave a characteristic signature in the detector (shown in Fig. 3.3) that can be used to identify them.

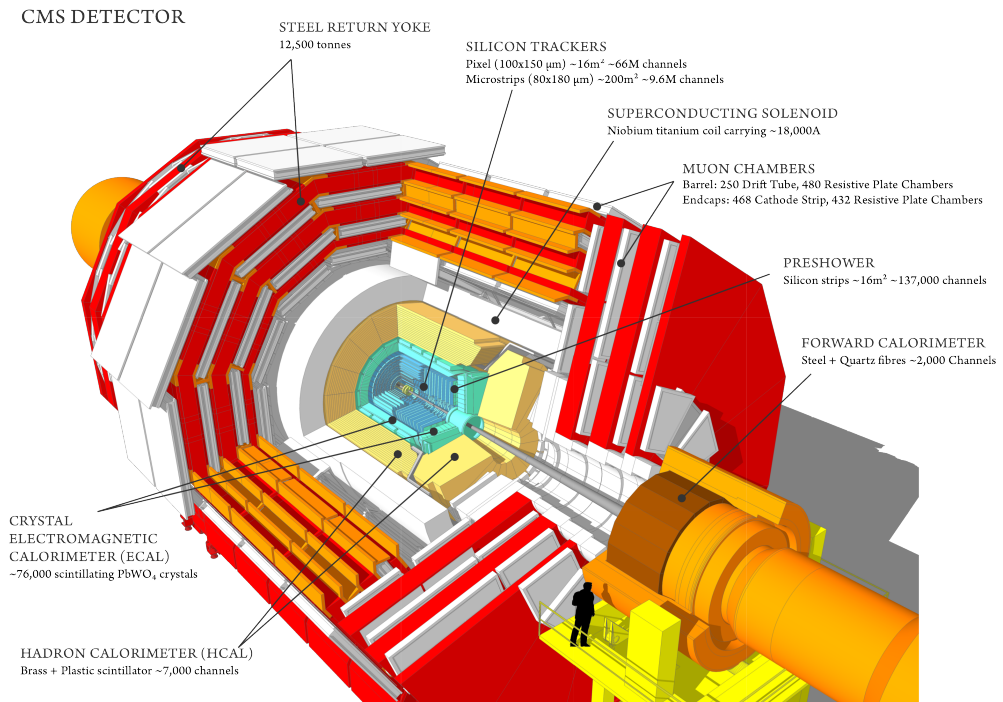


Figure 3.2: Layout of the CMS detector. The inner tracking system is surrounded by the ECAL, HCAL and the solenoid. The outermost part are the muon chambers interleaved with steel plates from the return yoke [59].

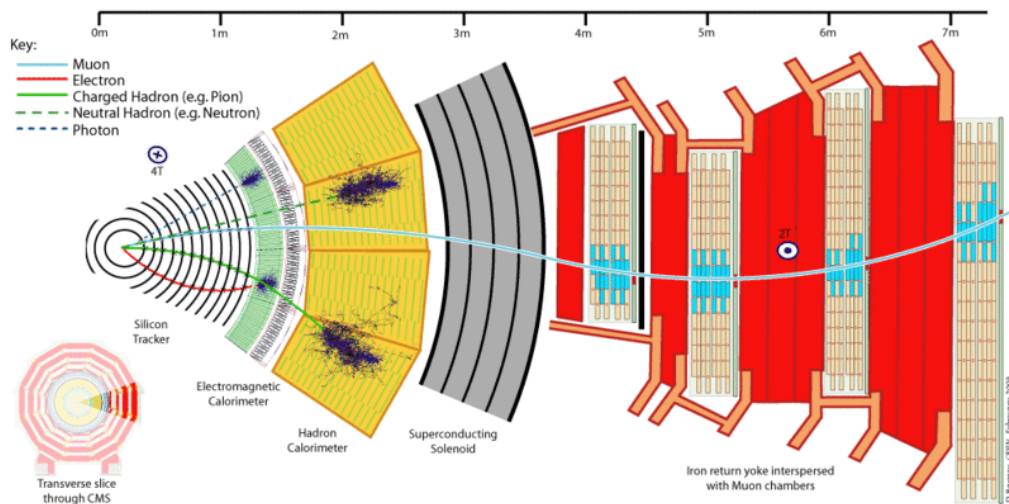


Figure 3.3: Particle identification in the CMS detector. Muons are detected in the inner tracker and in the muon stations. Electrons and photons are stopped in the ECAL while hadrons are contained inside the HCAL. Tracks of neutral particles indicated by the dashed lines are not detected [60].

The coordinate system used by CMS originates at the nominal collision point. The y-axis points vertically upwards and the x-axis radially inwards towards the center of the LHC while the z-axis runs along the beam direction towards the Jura mountains. The azimuthal angle φ is defined from the x-axis in the x-y-plane, the polar angle ϑ from the z-axis. The momentum and energy transverse to the beam direction, p_T and E_T , are calculated using only the x- and y-components [50]. The pseudo-rapidity η and rapidity y are given by

$$\eta = -\ln \tan\left(\frac{\vartheta}{2}\right) \text{ and} \quad (3.3)$$

$$y = \ln \frac{\sqrt{m^2 + p_T^2} \cosh^2(\eta) + p_T \sinh(\eta)}{\sqrt{m^2 + p_T^2}} \quad (3.4)$$

for a particle with the mass m .

3.2.1 Inner tracking system

The inner tracker provides a precise and efficient measurement of the charged particle momentum as well as a precise reconstruction of vertices. At the LHC design luminosity, of the order of 1 000 charged particles travel through the tracker each bunch crossing. Therefore, the tracker is required to have a high granularity and a fast response. Moreover, it has to withstand the severe radiation that the intense particle flux causes. To meet the requirements on granularity, speed and radiation hardness, the tracker is entirely silicon based [52].

Figure 3.4 shows the layout of the inner tracker. It consists of silicon pixel and strip detectors. The pixel detectors (PIXEL) are placed in three cylindrical layers at radii of 4.4, 7.3 and 10.2 cm from the beam line, where the particle flux is the highest (ca. 10^7 per second at $r \approx 10$ cm). They are completed by two disks of pixel detectors at each side. The PIXEL is surrounded by the Tracker Inner Barrel (TIB) spanning from 20 to 55 cm. It is composed of four layers of strip detectors. The Tracker Outer Barrel (TOB) is the outermost tracking detector in the barrel, covering the remaining region up to 116 cm with six layers of strip detectors. The size of the strips continuously increases with decreasing particle flux from 10 cm x 80 μm in the TIB to 25 cm x 183 μm in the TOB.

The tracking system in the barrel is completed by nine strip layers in each of the two Tracker EndCaps (TECs), thus extending the acceptance up to $|\eta| < 2.5$. Since the TIB is shorter than the TOB to avoid shallow track crossing angles, three additional inner disks called Tracker Inner Disk (TID) are placed between the TIB and the TECs [52]. A detailed description of the tracker system can be found in Refs. [61, 62].

3.2.2 Calorimeter

The calorimeter surrounding the inner tracker consists of two parts, the Electro-magnetic CALorimeter (ECAL) and Hadron CALorimeter (HCAL). The ECAL

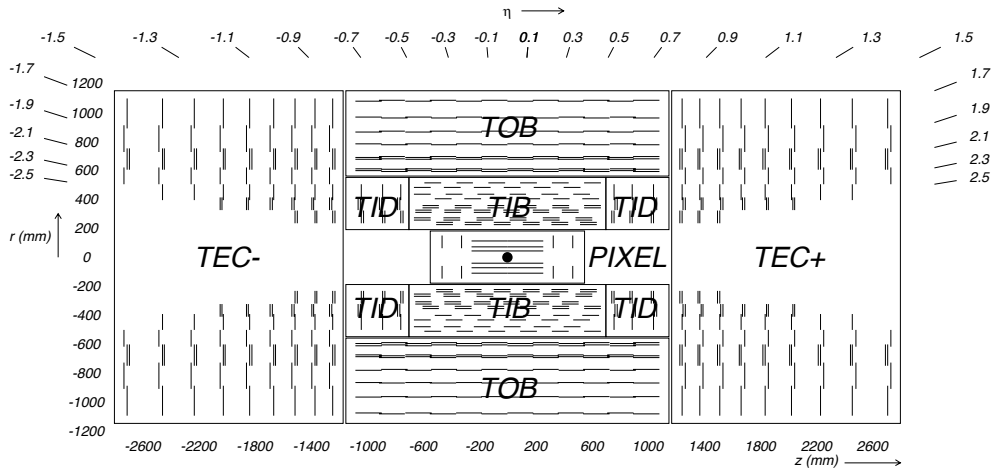


Figure 3.4: Cross section of the CMS tracking system. The PIXEL detector is surrounded by the Tracker Inner Barrel (TIB) and Tracker Outer Barrel (TOB). The endcaps consist of the Tracker Inner Disk (TID) and Tracker EndCap (TEC) systems. Each line represents a detector module [52].

is designed to measure the energies of electrons, photons and jets with great precision while hadrons deposit most of their energy in the HCAL.

The ECAL is made out of 61 200 homogeneous lead tungstate (PbWO_4) crystals in the barrel and 7 324 in each of the endcaps. It provides a good energy resolution up to $|\eta| < 3$. The chosen high density crystals are very fast, radiation hard, and have fine granularity. When electromagnetic particles pass through the crystals, blue-green scintillation light is emitted in about 25 ns, which is of the same order of magnitude as the nominal LHC bunch crossing time. The photodetectors used to detect the relatively low light output are required to be fast, radiation tolerant and to be able to operate in the high magnetic field. Silicon Avalanche PhotoDiodes (APDs) are chosen for the barrel region while Vacuum PhotoTriodes (VPTs) are used in the endcaps. A preshower detector is placed in front of the endcaps to reject π^0 particles [50, 52].

The extent of the HCAL is radially limited by the outer radius of the ECAL ($R = 1.77$ m) and the inner extent of the superconducting solenoid ($R = 2.7$ m). This also puts a restriction on the total amount of material that can absorb hadronic showers. Containing all hadronic showers inside the HCAL is important for the calculation of the energy imbalance or so-called missing energy, which is needed to detect very weakly interacting particles. Centrally ($|\eta| < 1.26$), the shower containment is improved by an outer hadron calorimeter consisting of an array of scintillators which is placed outside the magnetic coil. Additionally, two forward calorimeters covering the region $3 < |\eta| < 5$ were installed 11.2 m away from the interaction point to measure energetic forward jets [52].

The HCAL is a sampling detector with alternating layers of absorber and active scintillator material. Brass was chosen as absorber material as the interaction

length of particles in brass is reasonably short. Plastic scintillator tiles are used as active material and are read out by embedded WaveLength-Shifting (WLS) fibers [50, 52].

3.2.3 Superconducting magnet

The superconducting solenoid enclosing the HCAL is one of the key characteristic features of CMS. The high magnetic field of 3.8 T is chosen to achieve a momentum resolution that can determine the particle momentum up to ≈ 1 TeV. This high flux density requires the use of a superconducting material, in case of CMS a high purity aluminum stabilized Niobium-Titanium conductor. The field lines are closed by a steel yoke that is interleaved with the muon detectors.

3.2.4 Muon system

The muon system is important to identify muons and improve their momentum resolution at high p_T . For muons with p_T up to around 200 GeV, the best resolution is obtained by only using information from the inner tracker while additionally using the measurement in the muon detectors improves the resolution for higher p_T muons [50].

The muon system consists of three types of gaseous detectors arranged in five wheels in the barrel and two endcap disks, as is shown in Fig. 3.5. The types of detectors are chosen due to their robustness, reliability and moderate costs as the muon system covers the large active area of 25 000 m² [50].

In the cylindrical barrel region, the magnetic field is uniform and the muon rate is low. Drift Tubes (DTs) are used and arranged in four stations (MB1-MB4) interleaved with the return yoke plates of the magnetic field and a second type of muon detectors, the Resistive Plate Chamber (RPC). In the stations MB1 and MB2, one DT is placed between two RPCs while the other two stations consist of one DT and one RPC. In the endcaps, where the magnetic field is non-uniform and the muon rate is high, Cathode Strip Chambers (CSCs), additionally supported with RPCs, are used. They are arranged in four disks (ME1-ME4) interspersed with the return yoke plates and placed perpendicular to the beam line. The DTs and CSCs in combination with the RPCs provide two independent and complementary sources for the muon trigger system [50].

The complete muon stations cover a pseudo-rapidity range from -2.4 to 2.4, corresponding to an almost full geometric coverage $10^\circ < \vartheta < 170^\circ$.

Drift tube chambers

DT chambers are filled with a gas mixture of 85% Ar and 15% CO₂. Muons entering the DTs ionize the gas along their path. The resulting electrons and ions drift to their corresponding electrodes with a maximum drift path of 21 mm. Using the position of the hits and accounting for the drift time, the coordinates of

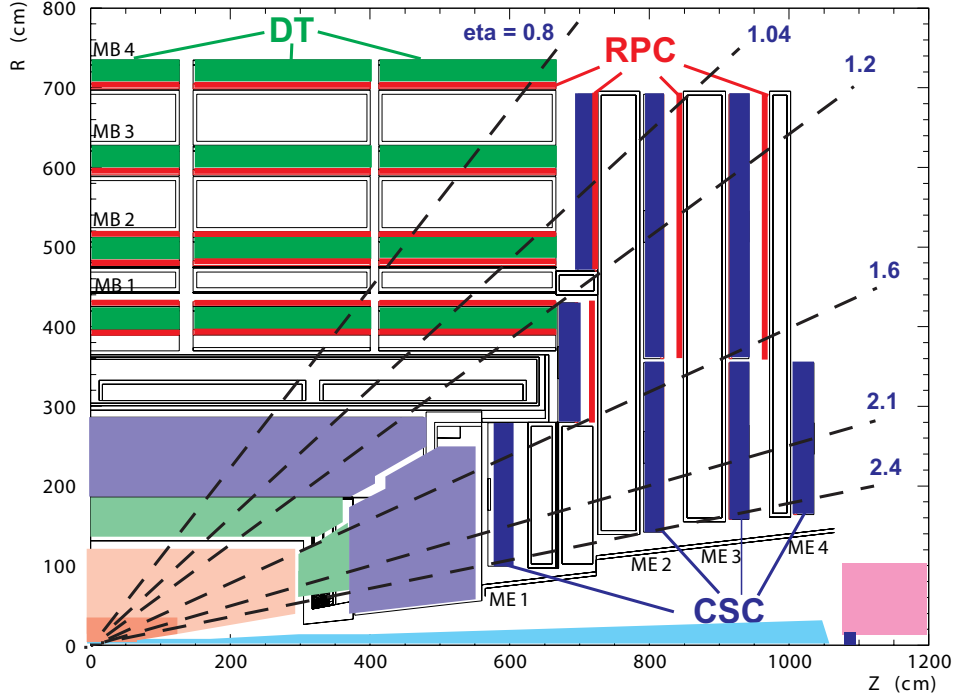


Figure 3.5: Layout of one quarter of the symmetrical muon system [50]: Drift Tubes (DTs) and Resistive Plate Chambers (RPCs) are installed in four stations (MB1-MB4) in the barrel region. The endcaps consist of RPCs and Cathode Strip Chambers (CSCs), also arranged in four stations (ME1-ME4). The muon stations are separated by the steel plates of the return yoke. The dashed lines indicate the η regions.

a muon can be determined with a resolution of approximately $100 \mu\text{m}$ in position and 1 mrad in the radial direction [52].

Cathode strip chambers

CSCs are multiwire proportional chambers which can operate at high rates and in large non-uniform magnetic fields. They have a trapezoidal shape and are arranged in rings overlapping in ϕ (except the third ring of the first endcap disk) to avoid gaps in the muon acceptance. In total, 468 CSCs are installed in four layers perpendicular to the beam axis in the two endcap regions. The resolution is typically about $200 \mu\text{m}$ in position and of the order of 10 mrad in the radial direction.

Resistive plate chambers

RPCs support the DT and CSC systems up to $|\eta| = 1.6$. RPCs are parallel-plate detectors filled with a non-flammable gas mixture of 96.2% $\text{C}_2\text{H}_2\text{F}_4$, 3.5% iC_4H_{10} and 0.3% SF_6 . They are operated in avalanche mode and have an excellent time

resolution of the order of 1 ns, but coarser position resolution than the CSCs and DTs. They are able to unambiguously identify the correct bunch crossing to which a muon track is associated [52].

3.2.5 Data acquisition and triggering

The LHC delivers billions of events per second. Nominally, a proton bunch crossing occurs every 25 ns, corresponding to a bunch crossing rate of 40 MHz. There may be several collisions at each crossing of the proton bunches depending on the luminosity. In 2012, when the LHC, running with a bunch crossing time of 50 ns, reached almost the design luminosity, there were on average 21 of these Pile-Up (PU) events [63]. The large amount of data cannot be processed or stored and therefore has to be reduced drastically by about a factor of 10^6 , down to the order of 10^2 Hz. The data reduction is achieved by a trigger system selecting physically interesting collision data. The triggering takes place in two subsequent steps: the hardware-based Level-1 (L1) trigger followed by the High Level Trigger (HLT) system [50].

Level-1 trigger

The completely hardware-based L1 trigger reduces the L1 output rate to about 100 kHz using programmable custom electronics. The L1 has to reach a fast and computationally inexpensive decision whether to keep or reject an event. Therefore, only information from the calorimeter and the muon stations is used at L1. If a positive decision is reached, the data are transferred from the buffer, where they are stored, to the HLT [50].

Figure 3.6 shows the architecture of the L1 trigger, which is divided into local, regional and global components. The local triggers or trigger primitive generators are based on energy deposits in the different calorimeter parts and hit patterns in the muon chambers. Regional triggers combine the information from the local triggers and rank the trigger objects, such as electron and muon candidates, based on their energy or momentum and quality. The information is then sent to the Global Calorimeter Trigger (GCT) and the Global Muon Trigger (GMT), which determine the highest-rank calorimeter and muon objects to transfer to the Global Trigger (GT). The GT takes the final decision to reject or accept an event. The core of the GT is the Global Trigger Logic used to calculate algorithms. It can execute simple algorithms, such as applying p_T and η thresholds. In total, 128 algorithms can be executed in parallel [50].

High level trigger

In case of a positive L1 decision, the data are transferred from the buffers residing on the detector, digitized and formatted. The data fragments from the different detector elements are then assembled and passed to one of the about 1 000 commercial processors running the HLT software code. The HLT reduces the output rate to the order of 10^2 Hz by applying filters and different algorithms.

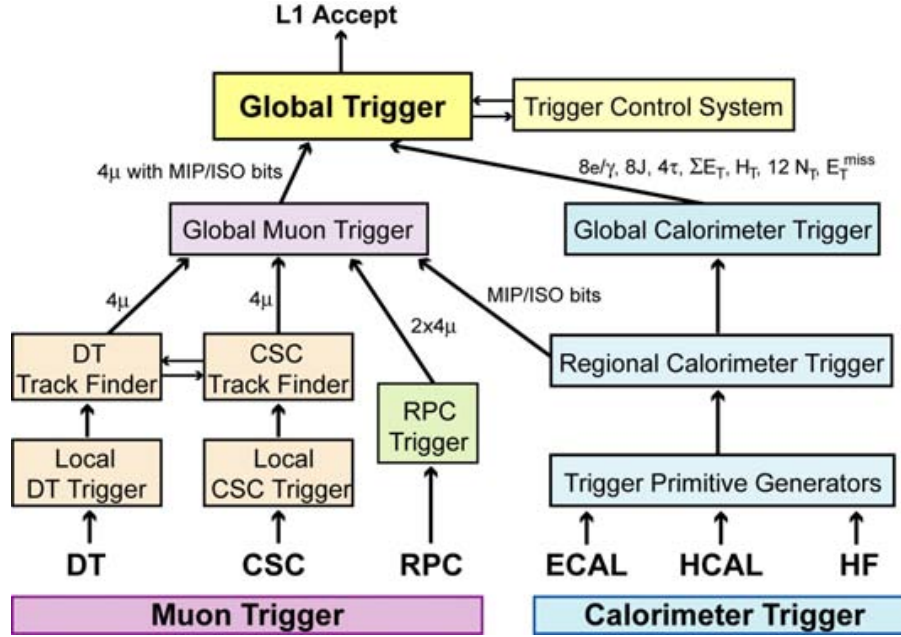


Figure 3.6: Architecture of the L1 trigger. The L1 trigger is divided into local or primitive, regional and global components. The information from the global muon and calorimeter triggers is passed to the global trigger that takes the final decision [52].

It has access to the complete read-out data of the events, but only objects and regions that are actually needed are reconstructed to be able to reject an event as soon as possible. In case of a muon trigger, first tracks in the muon chambers are reconstructed using the muon candidates provided by L1. Then, in a second step, the muon trajectories are extended into the tracker, thus greatly improving the muon momentum measurement.

Only data accepted by the HLT are used for the physics analyses. Detailed information about the HLT can be found in Ref. [64].

Dimuon trigger

In CMS, quarkonia are reconstructed using their dimuon decay. The simplest trigger solution, a trigger based on a single muon, is not applicable due to its high rates, in particular at low p_T . Therefore, the triggers that select quarkonium events require two muons coming from the same vertex. But above a certain luminosity, even requesting a dimuon is not enough to get acceptable trigger rates. Additional requirements are needed, such as setting thresholds on the dimuon kinematics or restricting the mass.

In 2010, the luminosity was low enough to implement a single trigger covering the mass region of all quarkonium states without restrictions on the dimuon

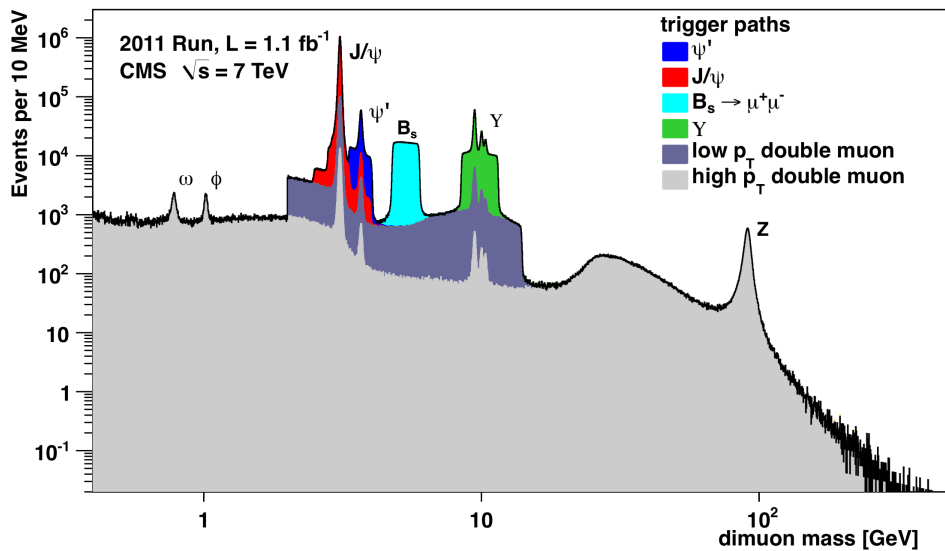
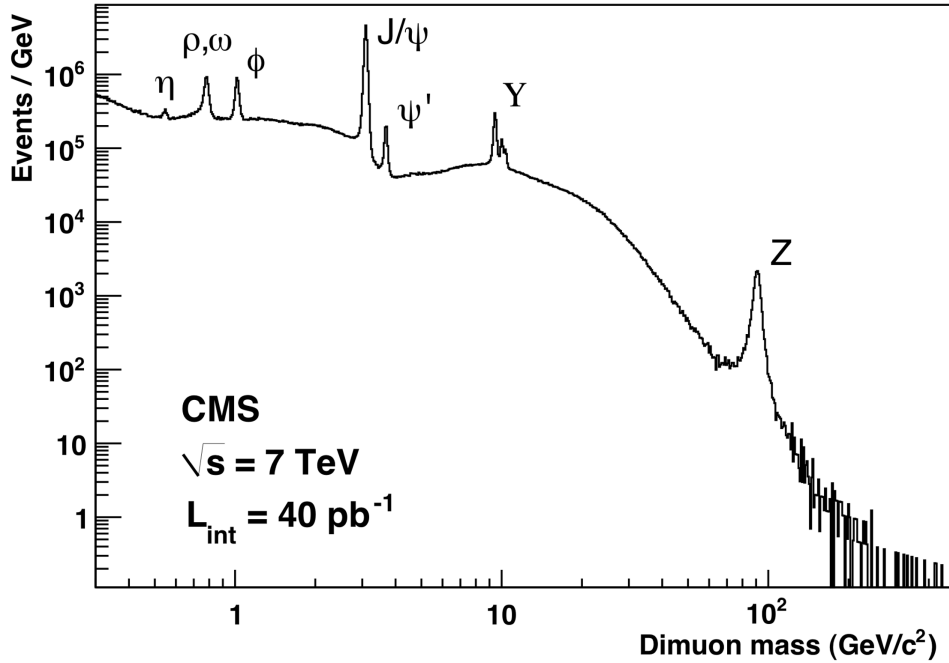


Figure 3.7: Invariant dimuon mass spectra showing events collected by a single dimuon trigger in 2010 (top) and collected by several dedicated triggers covering the mass windows of different resonances in 2011 (bottom) [65].

kinematics (`HLT_DoubleMu0_Quarkonium` seeded with `L1_DoubleMu0`), as can be seen in Fig. 3.7-top. In 2011, the luminosity increased putting forward the need of additional requirements to keep the trigger rates within the allocated bandwidth. The L1 seed was extended with a high-quality requirement for both muons (`L1_DoubleMu0_HighQ`). At the HLT, two requirements were implemented to reject combinatorial dimuons not coming from the same vertex: a dimuon vertex fit χ^2 probability greater than 0.5% and a distance of closest approach between the two muons of less than 5 mm. Moreover, the trigger was split into three different ones covering the mass window of the J/ψ , $\psi(2S)$ and the $\Upsilon(nS)$ states. The J/ψ and $\Upsilon(nS)$ trigger paths were restricted to the barrel region, $|y| < 1.25$, while the $\psi(2S)$ trigger path had no $|y|$ restrictions. The p_T thresholds, indicated by X, varied throughout the year, depending on the luminosity:

- `HLT_DimuonX_Jpsi_Barrel` with X = 10, 13 GeV,
- `HLT_DimuonX_PsiPrime` with X = 7, 9, 11 GeV,
- `HLT_DimuonX_Upsilon_Barrel` with X = 5, 7, 9 GeV,

Additionally, so-called cowboy dimuons, muon pairs that bend towards each other in the magnetic field, are rejected to keep the trigger rate low. Figure 3.7-bottom shows the mass spectrum of the events collected with dimuon triggers in 2011.

For 2012, a loose restriction on the pseudo-rapidity of both muons ($|\eta| < 2.1$) was implemented at L1 (`L1_DoubleMu0er_HighQ`). Thanks to data parking, where the data were only reconstructed later, during the shutdown period of the LHC, the requirements at HLT were relaxed compared to 2011. The barrel restriction was removed and the p_T thresholds lowered:

- `HLT_DimuonX_Jpsi` with X = 8, 10 GeV,
- `HLT_DimuonX_PsiPrime` with X = 5, 7 GeV,
- `HLT_DimuonX_Upsilon` with X = 5, 7 GeV.

No prescales were applied during any of the runs from 2010 to 2012 because too many events at high p_T , where the interesting physics lies, would have been rejected.

3.2.6 Muon reconstruction and identification

The standard CMS muon reconstruction for pp collisions first reconstructs tracks independently in the inner tracker (tracker tracks) and in the muon system (standalone-muon or Level-2 (L2) muon tracks). Then, two different approaches are used:

1. The tracker-track is extrapolated and matched to segments reconstructed in the muon detector in the inside-out approach to reconstruct the so-called tracker muon.

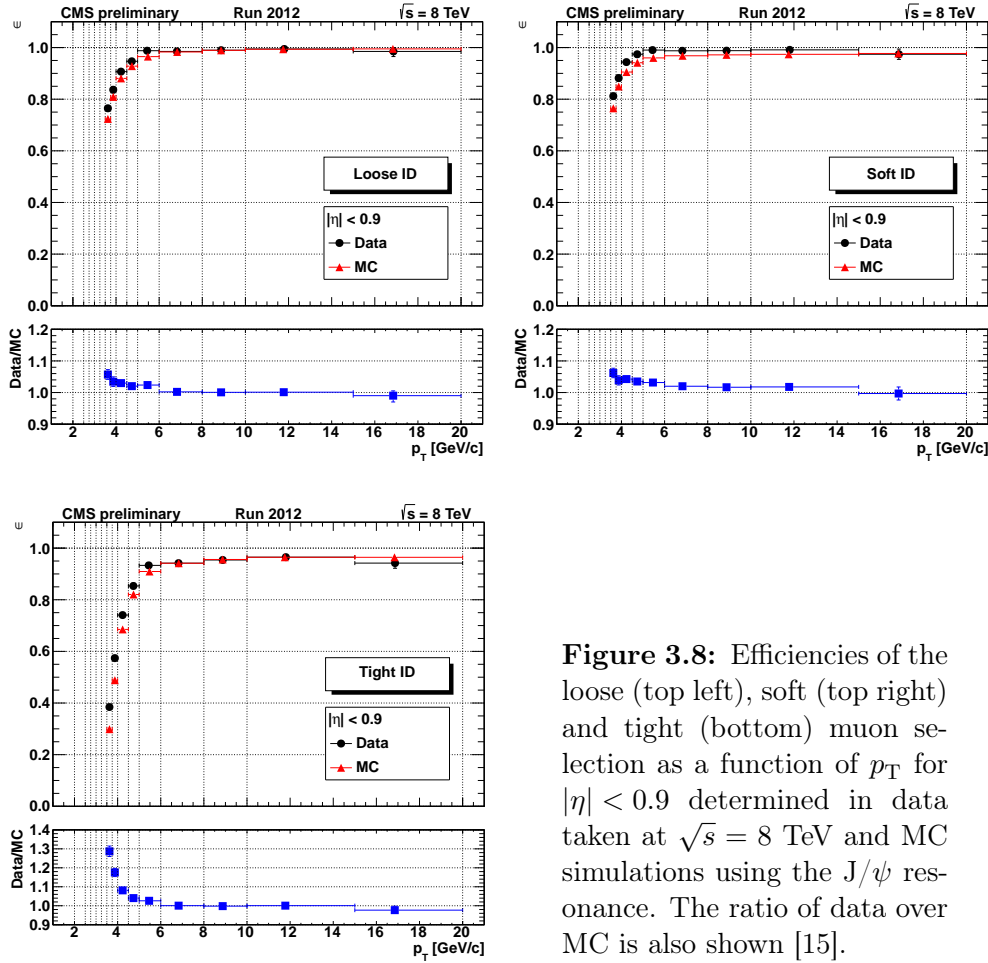


Figure 3.8: Efficiencies of the loose (top left), soft (top right) and tight (bottom) muon selection as a function of p_T for $|\eta| < 0.9$ determined in data taken at $\sqrt{s} = 8$ TeV and MC simulations using the J/ψ resonance. The ratio of data over MC is also shown [15].

2. The outside-in approach finds a tracker-track for each standalone-muon track and performs a combined fit of the tracker and muon-detector hits to reconstruct a so-called global or Level-3 (L3) muon [66].

There are four different muon identification algorithms commonly used in CMS:

1. The loose muon selection requires the particle to be identified as muon by the particle flow event reconstruction [67] and as global as well as tracker muon.
2. The soft muon selection requests a tracker muon with tight requirements on the matched muon segment, on the number of hits, the track χ^2 , and the impact parameters.
3. The tight muon selection equals the loose muon selection, but has additional requirements on the hits, global track χ^2 , and the impact parameters.
4. The high- p_T selection requests the muon candidate to be a global and tracker muon with tight selections, optimized to be efficient for muons with high p_T .

Efficiencies of the muon identification algorithms are studied with the Tag-and-Probe (TnP) method [68]. The tag, a very well identified muon which triggered the event, is combined with the probe, a tracker track or a loosely-identified muon, to lie in the mass window of a known resonance. At low p_T , the J/ψ resonance is used while the Z is used for higher p_T . The efficiency of the muon identification is obtained by simultaneously fitting the tag-probe invariant mass distributions for the probes passing and the ones failing the muon identification algorithm.

In case of the J/ψ , special efficiency triggers requesting a high quality global muon plus either an additional track in the silicon tracker or a L2 muon are implemented to be able to study the muon efficiencies in an unbiased way. They are prescaled to keep the trigger rate low.

Figure 3.8 shows typical examples of the single muon efficiencies for three different muon identification algorithms determined with the J/ψ resonance at $\sqrt{s} = 8$ TeV as a function of p_T . The efficiencies exhibit a steep turn-on curve until they reach the plateau region, which has an efficiency close to 100% for loose and soft muons and typically 95% for tight muons. The exceptions are the non-instrumented regions around $|\eta| = 0.25$ and 0.8 (the regions between 2 DT wheels) and $|\eta| = 1.2$ (the transition region between the barrel and endcaps), where the efficiency drops for the soft and tight muons. Data and Monte Carlo (MC) simulations agree well in the plateau, but show a discrepancy in the turn-on region. This arises from a small difference in the p_T resolution of muons in data and MC that gets enhanced by the large variations in efficiency between the individual bins in this region [66].

In quarkonium physics, the soft muon selection, which is specifically designed for low p_T muons, is usually applied. The efficiencies are obtained using the J/ψ resonance, even in the higher p_T regions.

3.2.7 CMS detector performance

The performance of CMS during Run I was outstanding. CMS recorded between 91% and 93% of the luminosity delivered by the LHC during pp collisions. Figure 3.9-top shows the integrated luminosities in the years 2010, 2011 and 2012. CMS collected 43.17 pb^{-1} of data in 2010 and 5.73 fb^{-1} in 2011 at $\sqrt{s} = 7$ TeV. In 2012, the integrated luminosity was 21.79 fb^{-1} recorded at $\sqrt{s} = 8$ TeV [54]. Figure 3.9-bottom shows the peak luminosities during Run I. The maximum peak instantaneous luminosity increased from $2.1 \times 10^{32} \text{ cm}^{-2}\text{s}^{-1}$ in 2010 to $3.7 \times 10^{33} \text{ cm}^{-2}\text{s}^{-1}$ in 2011, and to $7.7 \times 10^{33} \text{ cm}^{-2}\text{s}^{-1}$ in 2012 [63].

With increasing instantaneous luminosity, the number of pp interactions per bunch crossing, PU, increases, as is shown in Fig. 3.10. The PU poses a challenge on finding interesting events. In 2011, the PU was still relatively low with an average value of 14 and therefore had a negligible effect on the quarkonium measurements. In 2012, the average number of PU interactions increased to 21, with tails extending up to 40 [63].

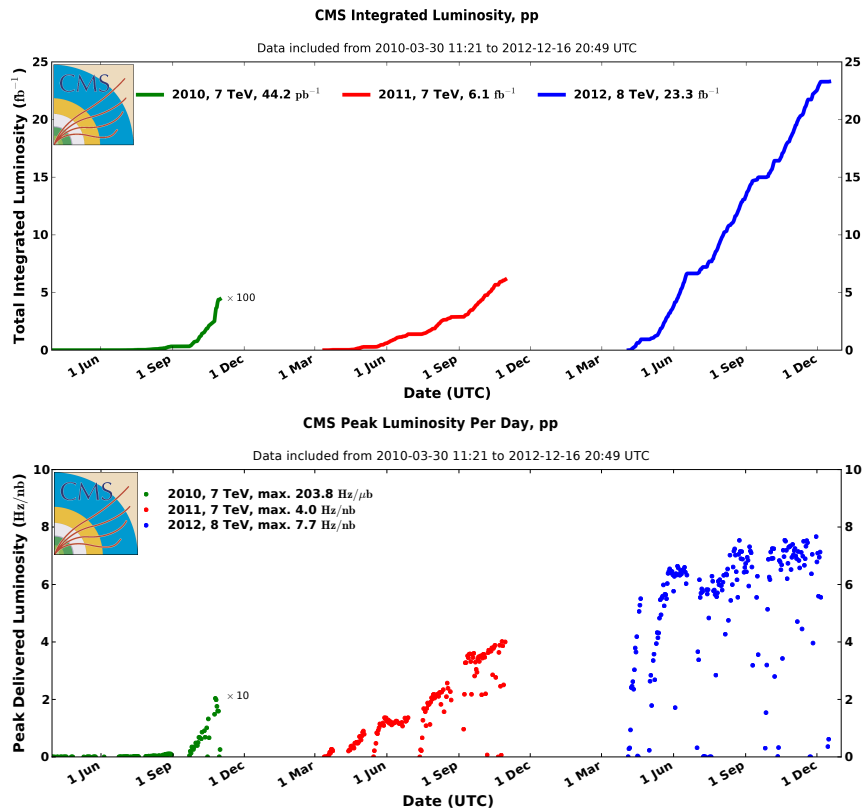


Figure 3.9: Cumulative integrated (top) and peak (bottom) luminosities collected by CMS in the 2010, 2011 and 2012 pp collision runs [63].

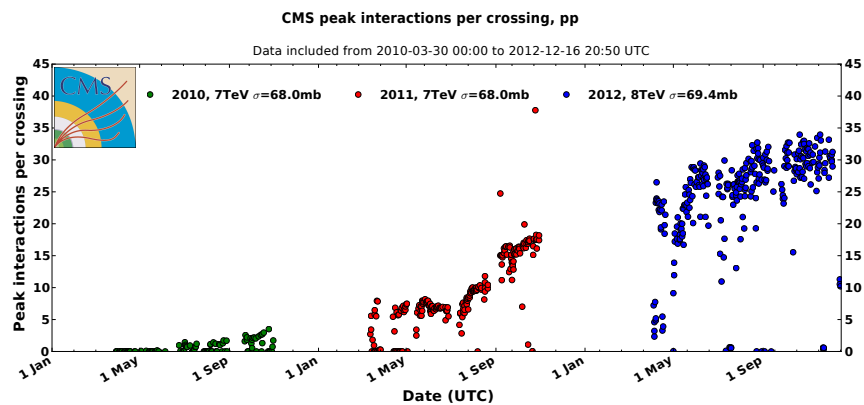
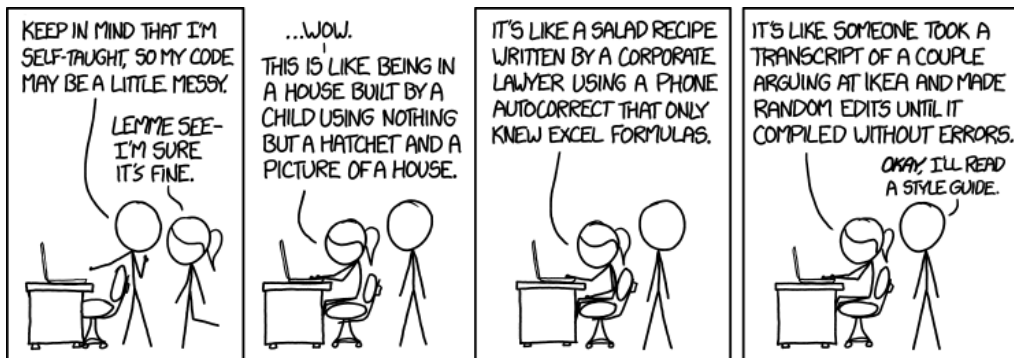


Figure 3.10: Peak number of interactions per bunch crossing in 2010, 2011 and 2012 pp collision runs [63].

CHAPTER 4

PROMPT $\psi(nS)$ POLARIZATIONS



<http://xkcd.com/1513/>

The measurement of the prompt $\psi(nS)$ polarization is based on the study of the dimuon angular decay distributions in the three polarization frames HX, PX and CS. The determination of the three polarization parameters λ_θ , λ_φ and $\lambda_{\theta\varphi}$ is completed by the frame-invariant quantity $\tilde{\lambda}$, which provides a systematic check of the whole analysis chain. The results are obtained for $14 < p_T < 70$ GeV and $|y| < 1.2$ in case of the J/ψ meson and $14 < p_T < 50$ GeV and $|y| < 1.5$ in case of the $\psi(2S)$.

4.1 Event selection

The events selection discussed in this Chapter applies to both the polarization and the cross section analyses.

4.1.1 Online selection

The data sample collected at the CMS experiment in pp collisions in 2011 at $\sqrt{s} = 7$ TeV is used. It corresponds to a total integrated luminosity of 4.9 fb^{-1} . The data was collected with dimuon triggers, requesting a muon pair with opposite electric charge, in the J/ψ ($2.8 < m_{\mu\mu} < 3.35$ GeV) and the $\psi(2S)$ ($3.35 < m_{\mu\mu} < 4.05$ GeV) mass windows. The J/ψ trigger path was restricted to the central rapidity region, $|y| < 1.25$, and had a minimum transverse momentum requirement, $p_T > 9.9$ GeV. The $\psi(2S)$ trigger path had no $|y|$ restrictions and a lower p_T threshold of 6.9 GeV. Both the J/ψ and the $\psi(2S)$ trigger paths required a dimuon vertex fit χ^2 probability greater than 0.5% and a distance of closest approach between the two muons of less than 5 mm. No explicit p_T requirement was imposed on the single muons at trigger level.

Both paths rejected the so called cowboy dimuons, muon pairs that bend towards each other in the magnetic field. By rejecting these events, the rate of the triggers stayed within the allocated trigger bandwidth while maintaining the low p_T thresholds of 9.9 and 6.9 GeV. Cowboy dimuons are not as easy to be dealt with as their counterpart, the seagull dimuons. A fraction of cowboy dimuons is missed by the dimuon trigger because the two muons traverse detector elements so close to each other that they look like a single muon. This is particularly problematic for high p_T dimuons.

Only at the very end of the 2011 run, the p_T threshold of the J/ψ trigger path had to be raised from 9.9 to 12.9 GeV to stay within the allocated trigger bandwidth. The effective integrated luminosity in that configuration was only 0.35 fb^{-1} . For simplicity, these events are not used in the analyses. Contrary to the polarization measurement, the production cross section is directly dependent on the luminosity. Therefore, this small difference in luminosity has to be taken into account when calculating the J/ψ cross section.

4.1.2 Offline selection

The dimuon vertex fit χ^2 probability greater than 0.5% requested by the trigger was raised to 1% in the offline analyses to reduce the combinatorial dimuon background.

The muon tracks are required to have hits in at least eleven tracker layers, with at least two in the silicon pixel detector, and to be matched with at least one segment in the muon system. They must have a good track fit quality (χ^2 per degree of freedom smaller than 1.8) and point to the interaction region. The selected muons must also match in pseudorapidity and azimuthal angle with the muon objects responsible for triggering the event.

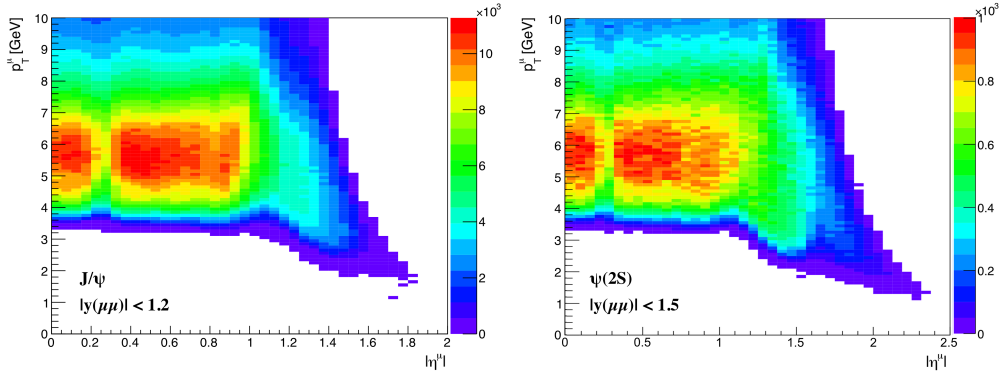


Figure 4.1: Distribution of single muons in the $|\eta|$ - p_T plane for the measured events with dimuon $p_T > 10$ GeV, selected in the 3σ windows around the J/ψ (left, for $|y| < 1.2$) and $\psi(2S)$ (right, for $|y| < 1.5$) pole masses. The colored z-axis indicates the number of events.

Figure 4.1 shows the distributions of the single muons in the $|\eta|$ - p_T -plane, built from dimuons in 3σ windows around the $\psi(nS)$ pole masses, after applying the offline selection. The strong magnetic field imposes a minimum p_T threshold on the single muons of the order of 3.3 GeV at mid-rapidity. In the forward region, the field effect is less pronounced.

The muons are requested to be in a fiducial phase-space window where the muon detection efficiencies are accurately measured:

$$\begin{aligned}
 p_T &> 4.5 \text{ GeV for } |\eta| < 1.2, \\
 p_T &> 3.5 \text{ GeV for } 1.2 < |\eta| < 1.4 \quad \text{and} \\
 p_T &> 3.0 \text{ GeV for } 1.4 < |\eta| < 1.6.
 \end{aligned}
 \tag{4.1}$$

Figure 4.2 shows the y - p_T distributions of the dimuon events within a $\pm 3\sigma$ mass window around the $\psi(nS)$ pole masses in a p_T range from 10 to 100 GeV. The $\psi(2S)$ event yield is much smaller than the J/ψ yield due to its smaller branching fraction in the dimuon decay channel.

The prompt charmonia are separated from those resulting from decays of b-hadrons through the use of the dimuon pseudo-proper decay length, which is the distance between the dimuon and the primary vertex [69],

$$\ell = L_{xy} \cdot M_\psi / p_T,
 \tag{4.2}$$

where M_ψ is the dimuon mass and L_{xy} is the transverse decay length in the laboratory frame, measured after removing the two muon tracks from the calculation of the primary vertex position. For events with multiple collision vertices, the dimuon momentum is extrapolated towards the beam line and L_{xy} is calculated with respect to the vertex closest to this extrapolation. The full decay of the b-hadron is not reconstructed, instead the $\psi(nS)$ kinematics are used, ignoring that they are different from the kinematics of the b-hadron. The boost from

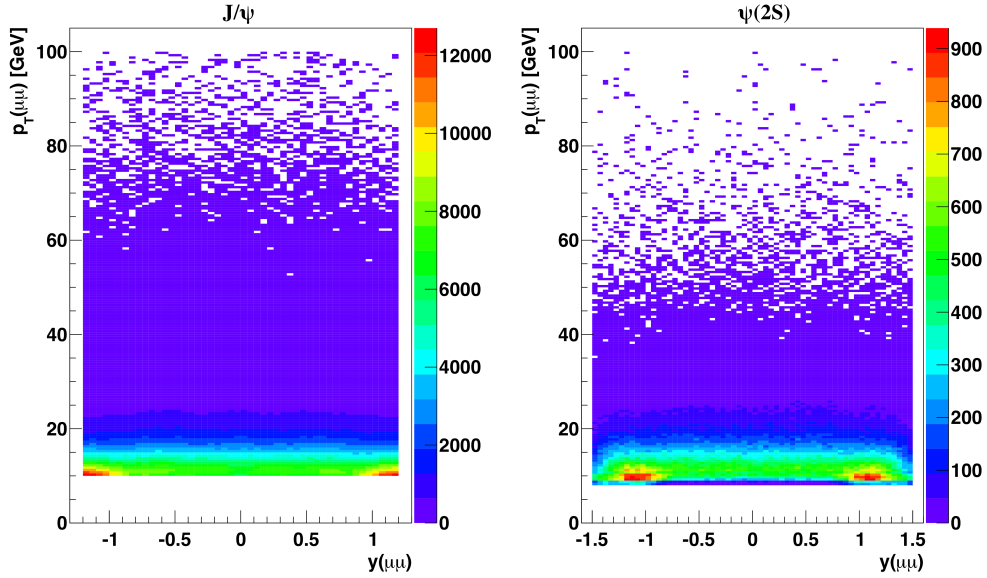


Figure 4.2: Distribution of the dimuon events within a $\pm 3\sigma$ mass window around the $\psi(nS)$ pole masses in the dimuon y - p_T plane for $10 < p_T < 100$ GeV and $|y| < 1.2$ in case of the J/ψ (left) and $|y| < 1.5$ in case of the $\psi(2S)$ (right). The colored z -axis indicates the number of events.

the laboratory frame to the center-of-mass frame is therefore only approximately done, which is reflected by the word “pseudo”.

In addition to the data sample, MC samples based on a $\psi(nS)$ particle gun are used. A particle gun generates particles with masses according to the Particle Data Group (PDG), in this case the J/ψ or $\psi(2S)$ state, and a four-momentum vector. The $\psi(nS)$ resonances are then decayed into muons using EVTGEN [70], interfaced with PYTHIA6, without any preferred polarization (isotropic decay). Final state radiation for the muons is generated through the PHOTOS package [71, 72]. A flat rapidity distribution is used in the range $-2.4 < y < 2.4$. This assumption is supported by the CMS cross section measurements that do not show significant rapidity dependencies [73]. Realistic p_T distributions, published by the CMS Collaboration in Ref. [73] and fitted with a functional form previously used by the HERA-B collaboration [74],

$$\frac{dN}{dp_T} \propto p_T^2 \cdot \left[1 + \left(\frac{1}{\beta - 2} \right) \cdot \frac{p_T^2}{\gamma} \right]^{-\beta}, \quad (4.3)$$

are used, where β and $\gamma \equiv \langle p_T^2 \rangle$ are the free fit parameters.

The time evolution of the triggers used during 2011 was also simulated. The samples were generated separately for the J/ψ or $\psi(2S)$ mesons up to very high p_T .

4.1.3 Phase-space coverage

The phase-space coverage of the angular distribution of the dimuon decay is restricted by the single muon fiducial cuts given in Eqn. 4.1. Figures 4.3 and 4.4 show the distributions of the events in the $\cos\vartheta$ - φ plane of the PX frame, selected in $\pm 3\sigma$ mass and pseudo-proper decay length windows around the pole masses of the J/ψ and $\psi(2S)$ states and $\ell = 0$. The phase-space coverage improves with increasing p_T .

The angular distribution corresponding to different polarization scenarios changes the most at $\cos\vartheta$ values close to $+1$ and -1 . The determination of the polarization in the PX frame is therefore easier to perform for high p_T dimuons, where the phase-space coverage extends up to $\cos\vartheta$ values close to $+1$ and -1 . At low p_T , most of the events are concentrated in the range $|\cos\vartheta| < 0.5$.

4.1.4 Definition of the kinematic cells of the measurement

The measurement of the quarkonium polarizations should not be conducted in too broad rapidity bins because the polarization might change as a function of the production kinematics of the meson, as explained in Ref. [9]. The polarization is therefore determined in two rapidity bins for the J/ψ , $|y| < 0.6$ and $0.6 < |y| < 1.2$, as the J/ψ trigger was restricted to $|y| < 1.25$. The $\psi(2S)$ trigger did not have this restriction. Therefore, a third rapidity bin, $1.2 < |y| < 1.5$, is added, where the higher edge is imposed by the single muon fiducial cut on pseudo-rapidity, $|\eta| < 1.6$.

The event sample is further divided into p_T bins in such a way that each bin contains a sufficient number of events to reliably extract the polarization. The following edges in p_T are chosen:

- $p_T(J/\psi)$: 14, 16, 18, 20, 22, 25, 30, 35, 40, 50, 70 GeV
- $p_T(\psi(2S))$: 14, 18, 22, 30, 50 GeV

The lowest edge of $p_T = 14$ GeV is chosen to stay in a region where the systematic uncertainties are under control and the whole analysis procedure was seen to be robust.

4.2 Single muon and dimuon efficiencies

The precise determination of the muon detection efficiencies is crucial for the study of both the production cross section as well as the polarization. The polarization is only dependent on the shape of the efficiencies, not the absolute values. The production cross section on the other hand is very dependent on the absolute values. An inaccurate or insufficient knowledge of the efficiencies may bias the measurements. Therefore, a lot of time and effort has been invested into the study of the muon efficiencies.

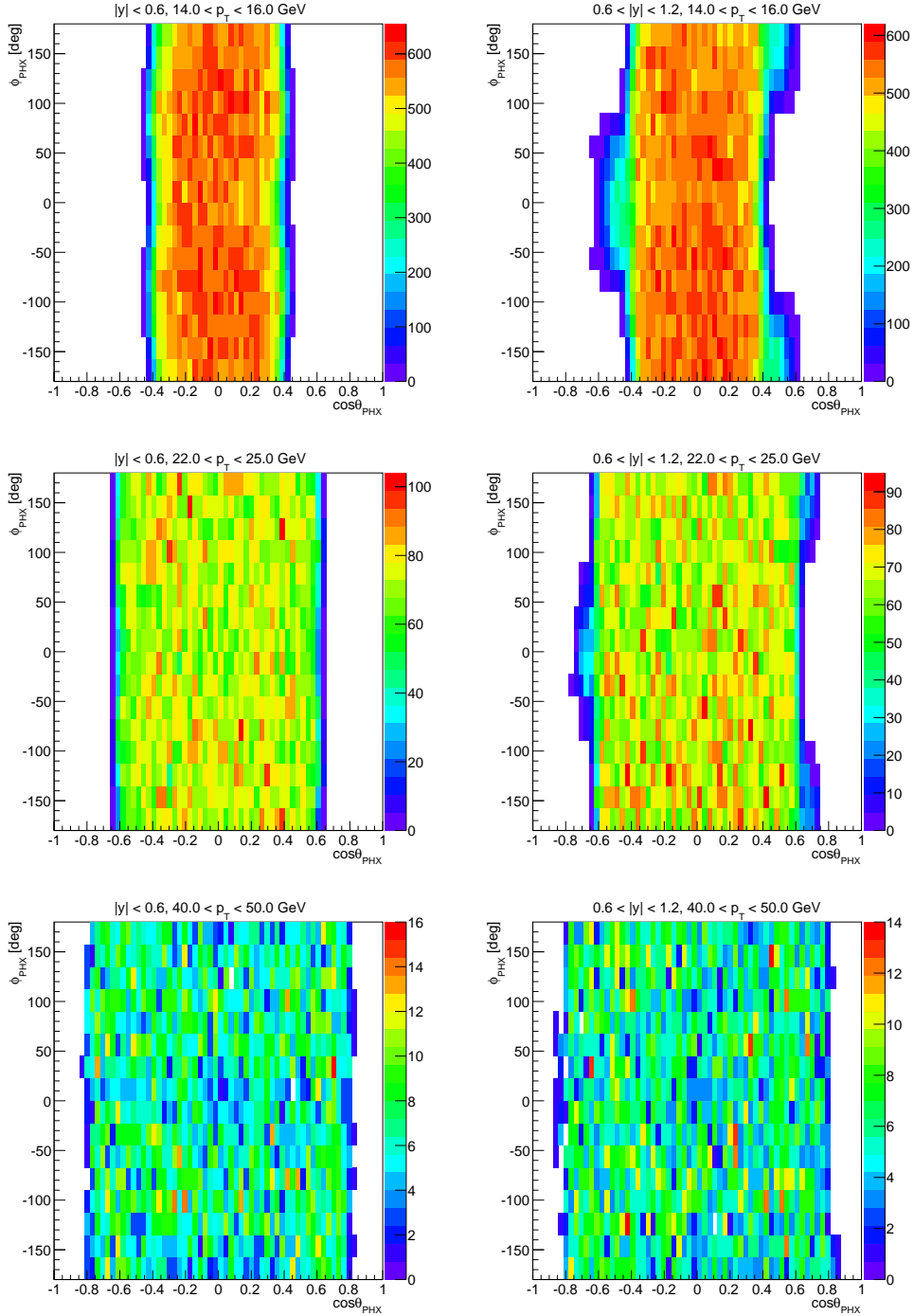


Figure 4.3: Dimuon angular distributions in the PX frame after all selection cuts, selected in the $\pm 3\sigma$ windows around the J/ψ pole mass and $\ell = 0$, in the dimuon rapidity regions $|y| < 0.6$ (left) and $0.6 < |y| < 1.2$ (right), and in three dimuon p_T ranges (top to bottom). The colored z-axis indicates the number of events.

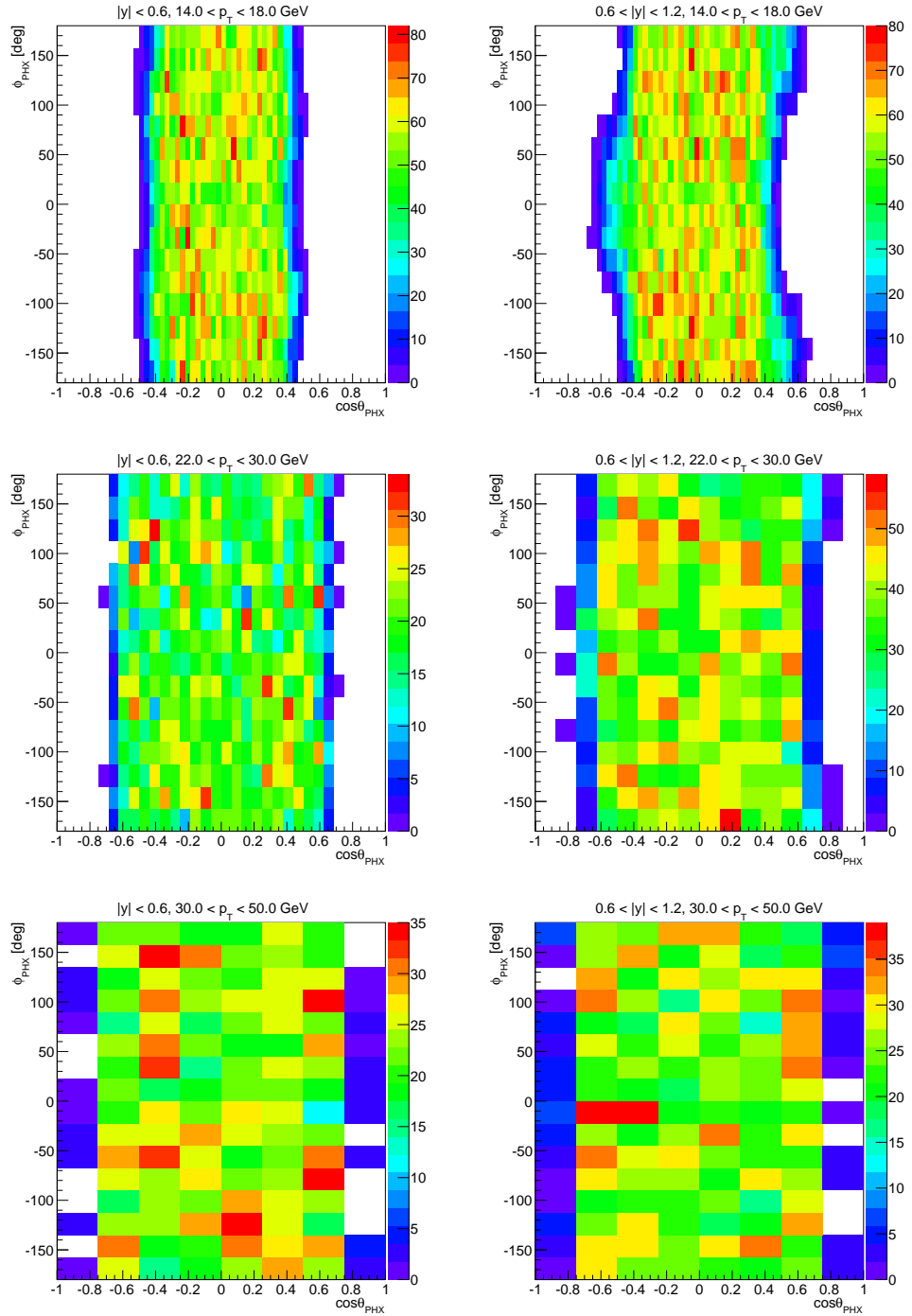


Figure 4.4: Same as previous figure for the $\psi(2S)$.

The total dimuon efficiency, $\varepsilon_{\mu\mu}$, is given by

$$\varepsilon_{\mu\mu} = \varepsilon_{\mu_1} \cdot \varepsilon_{\mu_2} \cdot \varepsilon_{\text{vtx}} \cdot \rho, \quad (4.4)$$

where ε_{μ_1} and ε_{μ_2} are the efficiencies of the single muons, ε_{vtx} represents the efficiency of the dimuon vertex fit χ^2 probability requirement and ρ is a correction factor due to the losses of close-by muons.

4.2.1 Single muon efficiencies

The single muon efficiencies are derived with the TnP method [68] described in Chapter 3.2.6. They can be factorized into five parts

$$\varepsilon_{\mu} = \varepsilon_{\text{track}} \cdot \varepsilon_{\text{id}} \cdot \varepsilon_{\text{qual}} \cdot \varepsilon_{\text{L1-L2}} \cdot \varepsilon_{\text{L3}}, \quad (4.5)$$

where $\varepsilon_{\text{track}}$ is the efficiency of finding a muon track in the silicon detector, $\varepsilon_{\text{id}} \cdot \varepsilon_{\text{qual}}$ the muon reconstruction efficiency requiring certain quality cuts and $\varepsilon_{\text{L1-L2}} \cdot \varepsilon_{\text{L3}}$ the trigger efficiencies.

Special trigger paths have been implemented to study the muon efficiencies in an unbiased way. One trigger requests a high quality global muon plus an additional track in the silicon tracker. This trigger allows the study of all muon related parameters (ε_{ID} , $\varepsilon_{\text{L1-L2}}$). Another trigger requires a high quality global muon and a L2 muon, allowing the study of all tracking related parameters ($\varepsilon_{\text{qual}}$, ε_{L3}). The five individual parts of the single muon efficiencies have been studied extensively on data and MC as a function of p_{T} and $|\eta|$. A lengthy discussion can be found in Ref. [14].

The total single muon efficiencies calculated with the TnP method have been validated using a special MC sample that allowed the direct study of the single muon efficiencies without any bias from the existence of the second muon. The high statistics of this MC truth sample makes it possible to determine the MC truth efficiencies in very fine p_{T} bins with a width of only 0.25 GeV. The comparison between MC based TnP and MC truth efficiencies defines a region where the single muon efficiencies are reliable (see Eqn. 4.1).

To reduce statistical fluctuations and effects of the chosen binning, the p_{T} shapes of the data-driven single muon efficiencies are parametrized using the linearly interpolated very finely binned MC truth efficiencies, $\varepsilon_{\mu}^{\text{MCtruth}}$,

$$\varepsilon_{\mu}(p_{\text{T}}) = \varepsilon_{\mu}^{\text{MCtruth}} \cdot \left(\frac{1}{p_{\text{T}}^{\text{scale}}} \cdot p_{\text{T}} - p_{\text{T}}^{\text{shift}} \right) + \varepsilon^{\text{shift}}, \quad (4.6)$$

where $p_{\text{T}}^{\text{scale}}$, $p_{\text{T}}^{\text{shift}}$ and $\varepsilon^{\text{shift}}$ are free parameters to shift and scale the p_{T} shape and the efficiency value of the MC truth efficiencies.

From the full information of the covariance matrix obtained in the fit, a variation of the free fit parameters can be constructed. New efficiency curves still compatible with the central values of the parametrization within the errors can be built by adding or subtracting the variation. With this procedure, a total of six

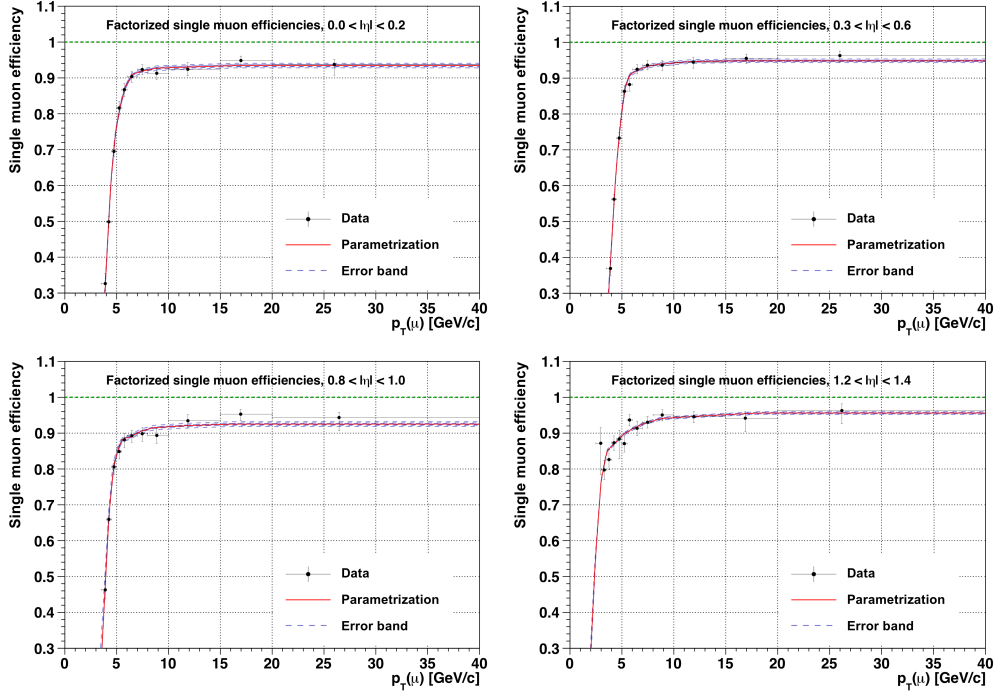


Figure 4.5: Parametrization of the p_T differential data-driven TnP efficiencies and the corresponding error bands compared to the data points in four different $|\eta|$ ranges.

efficiency curves (two for each of the three free fit parameters) is obtained while correctly taking into account the correlations between the parameters.

Figure 4.5 shows four examples of the parametrized function of the data-driven TnP efficiencies and their corresponding error bands.

4.2.2 Efficiency of the dimuon vertex fit χ^2 probability requirement

To study the efficiency of the dimuon vertex fit χ^2 probability requirement, ε_{vtx} , which is the last module of the dimuon trigger path, a special trigger identical to the dimuon trigger, but without requesting a cut on the dimuon vertex fit χ^2 probability was implemented. A special setting called *OneProbe* was then used to determine ε_{vtx} with TnP: The tag and probe pair is set to be the dimuon pair identified by the special trigger. A passing pair is required to fire the dimuon trigger.

For the measurement of the prompt $\psi(nS)$ polarizations, the efficiency is derived in bins of $\cos\vartheta$ and φ . It is flat over the full kinematic range. Since only a modulation in efficiencies, not the absolute value, introduces changes in the extracted polarization, ε_{vtx} is not applied in the nominal analysis. A systematic uncertainty due to ε_{vtx} is assigned as discussed in Chapter 4.6.5.

4.2.3 Muon pair correlations

Since the dimuon trigger cannot distinguish two close-by muons, which is in particular problematic at higher p_T ($\gtrsim 35$ GeV), the dimuon efficiency cannot be calculated as a product of the single muon efficiencies. A correction factor, ρ , accounting for the inefficiency introduced by the dimuon trigger, has to be applied. This correction factor is evaluated with MC.

For the measurement of the polarizations, ρ is obtained as function of $\cos \vartheta^{\text{PX}}$, ϕ^{PX} , p_T and $|y|$. Figure 4.6 shows ρ as function of $\cos \vartheta^{\text{PX}}$ for various (shifted) slices in φ^{PX} and p_T bins for the rapidity region $|y| < 0.6$. The ρ factor seems to be flat and close to unity up to $p_T \approx 35$ GeV. To confirm this qualitative observation, the flatness of ρ in the $\cos \vartheta^{\text{PX}} - \phi^{\text{PX}}$ plane is studied in several ways. One method is to fit the maps with a function analogous to the polarization function (Eqn. 2.3) to see above which dimuon p_T the extracted λ parameters are no longer compatible with zero. The deviations from zero start at $p_T \approx 35$ GeV.

The deviations are introduced by trigger inefficiencies when the two muons are too close to each other. To check which phase-space regions are affected by the dimuon inefficiencies, the spatial variable $\Delta R_{\Delta p_T}^{\text{elliptic}}$ is defined

$$\Delta R_{\Delta p_T}^{\text{elliptic}} = \sqrt{(1.2 \cdot \Delta\varphi)^2 + (\Delta\eta)^2 + 0.00157 \cdot (\Delta p_T)^2}, \quad (4.7)$$

starting from the distance variable $\Delta R = \sqrt{(\Delta\varphi)^2 + (\Delta\eta)^2}$. It is defined such that the dimuon efficiency depends only on this variable $\Delta R_{\Delta p_T}^{\text{elliptic}}$.

The scale value of 1.2 for $\Delta\varphi$ is chosen by looking at the distribution of triggered over reconstructed J/ψ MC events with $p_T > 50$ GeV and $|y| < 1.2$ in the $|\Delta\eta| - \Delta\varphi$ plane, which is shown in Fig. 4.7-left. The trigger-induced efficiency ridge visible in the same figure is not exactly symmetric in $|\Delta\eta|$ and $\Delta\varphi$. This can be appreciated by looking at the dashed green line representing a constant $\Delta R_{\Delta p_T}^{\text{elliptic}} = \sqrt{(1.2 \cdot \Delta\varphi)^2 + (\Delta\eta)^2}$ value of 0.15. For $\Delta R_{\Delta p_T}^{\text{elliptic}} > 0.15$, the dimuon efficiency defined as the triggered over reconstructed J/ψ MC events is very high, the muon pair correlations are practically non-existent.

The term $0.00157 \cdot (\Delta p_T)^2$ is added to $\Delta R_{\Delta p_T}^{\text{elliptic}}$ because of the dependence of the muon pair inefficiencies on the relative proximity of the two single muons in the p_T dimension. Figure 4.7-right shows the dimuon efficiency in the $\Delta R_{\Delta p_T}^{\text{elliptic}} - \Delta p_T$ plane. For a given value of $\Delta R_{\Delta p_T}^{\text{elliptic}}$, the trigger efficiency depends slightly on Δp_T , as illustrated by the curved green line.

The polarization parameters are now calculated with a cut on the $\Delta R_{\Delta p_T}^{\text{elliptic}}$ variable so that the dimuon events are fully efficient over the considered phase-space. The results are compatible with the nominal analysis where no such $\Delta R_{\Delta p_T}^{\text{elliptic}}$ cut is used, but instead the correction factor ρ is applied. However, the results obtained with the $\Delta R_{\Delta p_T}^{\text{elliptic}}$ cut are statistically limited. Therefore, they are only used to evaluate the systematic uncertainty due to ρ at high p_T .

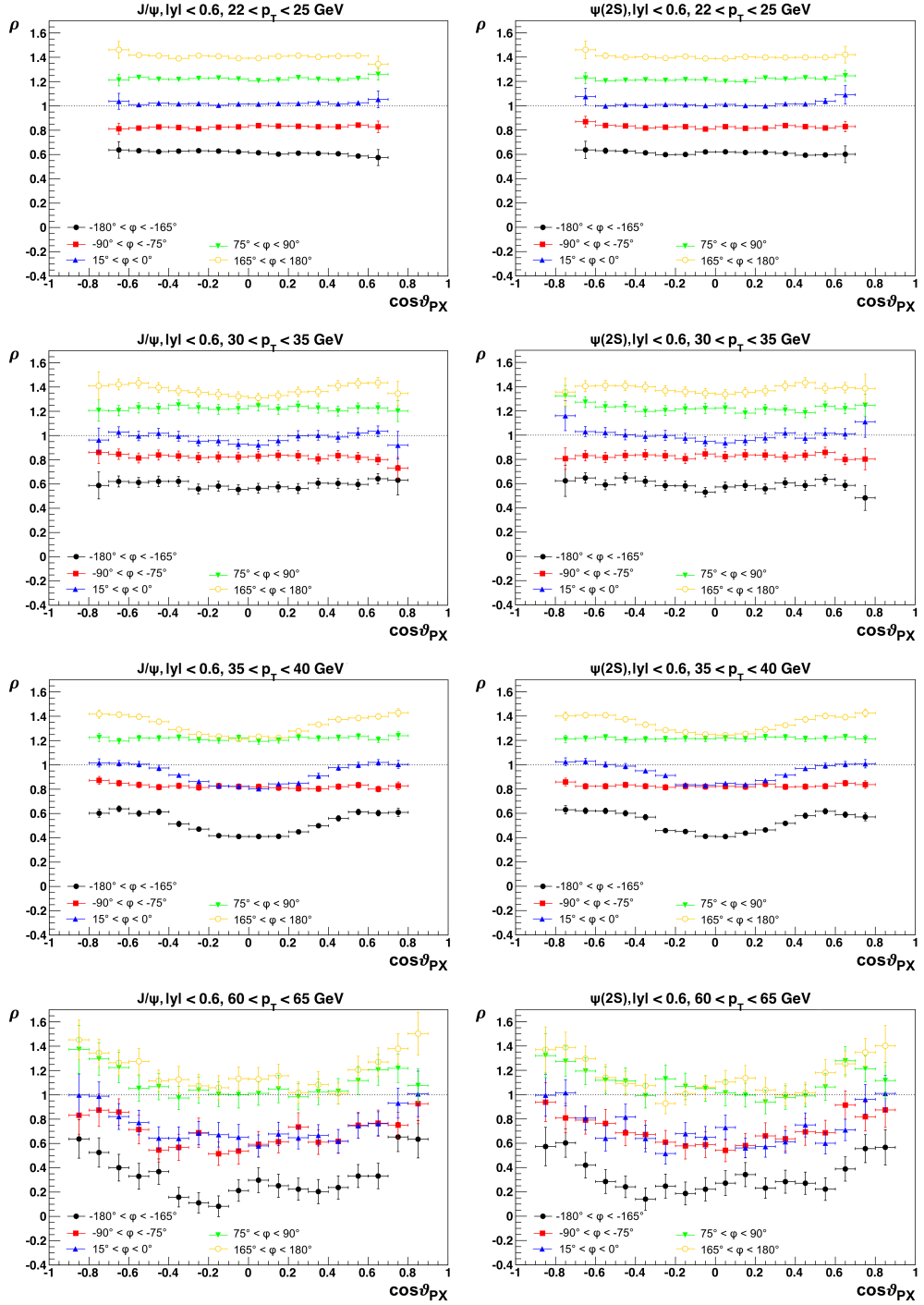


Figure 4.6: Examples of ρ as a function of $\cos\vartheta$ in the PX frame, for various cells of p_T (from top to bottom) in the rapidity region $|y| < 0.6$, for the J/ψ (left) and the $\psi(2S)$ (right). The five sets of points in each plot correspond to different slices in the φ dimension: $[-180^\circ, -165^\circ]$ (black, shifted by -0.4), $[-90^\circ, -75^\circ]$ (red, shifted by -0.2), $[-15^\circ, 0^\circ]$ (blue, not shifted), $[75^\circ, 90^\circ]$ (green, shifted by 0.2), $[165^\circ, 180^\circ]$ (orange, shifted by 0.4).

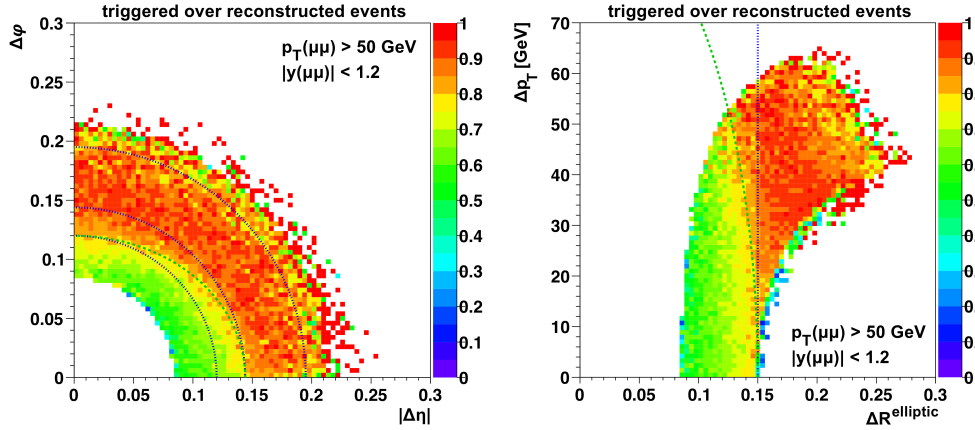


Figure 4.7: Distribution of triggered over reconstructed J/ψ MC events with generated $p_T > 50$ GeV and $|y| < 1.2$ in the $|\Delta\eta|-\Delta\varphi$ (left) and the $\Delta R^{\text{elliptic}}-\Delta p_T$ (right) planes. The colored z-axis indicates the number of events. Left: The green line indicates a constant $\Delta R^{\text{elliptic}} = 0.15$ while the blue lines represent constant ΔR values. Right: The blue line indicates a constant $\Delta R^{\text{elliptic}} = 0.15$. The green line represents the change from a region with high efficiency to one with low efficiency.

4.3 Polarization framework

The ambiguous measurements of quarkonium polarization by the Tevatron experiments have shown that the determination of quarkonium polarization is a complex and challenging problem. The multidimensionality and the severe restrictions in angular space imposed by the single muon fiducial cuts and the limited sensitivity of the CMS detector to low p_T muons enhance the level of difficulty of the measurement. Traditional methods to study quarkonium polarization using maximum likelihood fits were found to be non convergent. Thus, a new framework was developed within the CMS quarkonium group to get a precise and reliable extraction of the angular distribution of vector meson decays.

This new method can be applied to any quarkonium state. It does not rely on acceptance maps or template methods and is fully data-driven. Thus, no assumptions on any theoretical model are used.

The required inputs to the framework are:

- The four-momentum vectors of the two muons of the events selected in a suitable signal region
- The fraction of background events f_{BG} determined from fits to the mass and the pseudo-proper decay length
- The $(p_T, |y|, m_{\mu\mu}, \cos\vartheta, \varphi)$ distribution of the background events: The five dimensional distribution is given as the product of the two-dimensional $(\cos\vartheta, \varphi)$ distribution and the three dimensional $(p_T, |y|, m_{\mu\mu})$ distribution. This implicitly assumes that the $(\cos\vartheta, \varphi)$ distributions do not change

inside each $(p_T, |y|, m_{\mu\mu})$ bin, which is justified given the small bin widths. The $(\cos\vartheta, \varphi)$ distributions of the background events are given in the PX frame since the acceptance and efficiency coverage have particularly simple shapes in this frame. The model to accurately describe the background distribution is discussed in more detail in Chapter 4.5.

- The dimuon efficiencies $\varepsilon(\vec{p}_{\mu^+}, \vec{p}_{\mu^-})$ as a function of the three-momentum vectors \vec{p} of the positive and negative muons: Only the shape of the muon efficiencies, not the magnitude, is relevant to the polarization measurement as the shape of the angular decay distribution is determined.

The framework proceeds in four steps:

1. Subtraction of the background
2. Definition of the likelihood
3. Sampling of the likelihood
4. Extraction of the results

Background-like events are subtracted from the data sample on an event-by-event basis using a likelihood ratio criterion. The background subtraction uses the dimuon kinematics $(p_T, |y|, m_{\mu\mu}, \cos\vartheta, \varphi)$ of the background events, estimated from the mass sidebands and the nonprompt region of the data sample. Further details on the background model are given in Chapter 4.5. Background-like events are removed until the previously determined fraction f_{BG} is reached.

From the remaining signal-like events, denoted with i , the full likelihood of the polarization parameters $\mathcal{L}(\vec{\lambda})$ is defined as

$$\mathcal{L}(\vec{\lambda}) = \prod_i \mathcal{E}(\vec{p}_{\mu^+}^{(i)}, \vec{p}_{\mu^-}^{(i)}), \quad (4.8)$$

where \mathcal{E} is the probability of a given event,

$$\mathcal{E}(\vec{p}_{\mu^+}, \vec{p}_{\mu^-}) = \frac{1}{\mathcal{N}(\vec{\lambda})} \cdot W(\cos\vartheta, \varphi|\vec{\lambda}) \cdot \varepsilon(\vec{p}_{\mu^+}, \vec{p}_{\mu^-}). \quad (4.9)$$

The function $\mathcal{N}(\vec{\lambda})$ represents the normalization while $W(\cos\vartheta, \varphi|\vec{\lambda})$ is the dimuon angular distribution given by Eqn. 2.3. The normalization $\mathcal{N}(\vec{\lambda})$ is calculated by uniformly integrating $W \cdot \varepsilon$ over $\cos\vartheta$ and φ , using events generated according to the efficiency and acceptance corrected $(p_T, |y|, m_{\mu\mu})$ distribution found in data.

Instead of relying on a maximization of the likelihood to determine the polarization parameters, a Bayesian Markov Chain Monte Carlo (MCMC) approach is used to obtain the full Posterior Probability Density (PPD) of the three polarization parameters in the three reference frames. The priors are assumed to be uniform. A Metropolis-Hastings algorithm [75] based on the concept of importance sampling is used: The extracted parameter values are kept or rejected

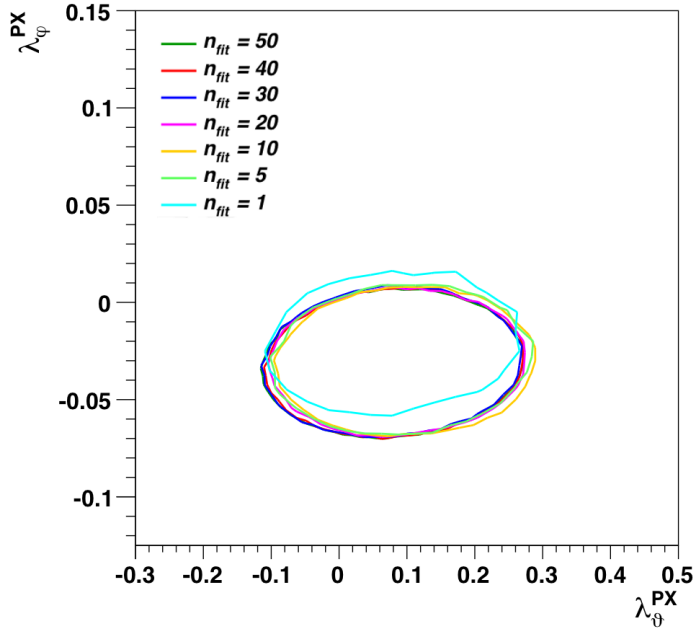


Figure 4.8: Contours of the two-dimensional projections of the PPD on λ_ϑ and λ_φ 68.3% CL in the PX frame, evaluated for different numbers of n_{fit} , for the ranges $|y| < 0.6$ and $20 < p_T < 30$ GeV in case of the $\Upsilon(3S)$.

depending on the likelihood ratio of a given extraction with respect to the ones of the previous extraction.

Due to the random nature of the background subtraction and the likelihood sampling, the full procedure is repeated several times. The results are found to be reasonably stable after $n_{\text{fit}} = 30$ repetitions, as can be seen in Fig. 4.8. The actual number of iterations used in this analysis is $n_{\text{fit}} = 50$. The PPDs of the $n_{\text{fit}} = 50$ iterations are merged, thus automatically including the uncertainties due to the random nature of the framework in the spread of the combined PPD.

The output of the polarization framework is the PPD as a function of the three polarization parameters λ_ϑ , λ_φ and $\lambda_{\vartheta\varphi}$ or any observable depending on these parameters. The value of the highest posterior probability in its one-dimensional projection is used as estimate of the best value of each polarization parameter. The one-dimensional PPD is fit with a Gaussian in a small interval around the maximum to avoid any effects due to statistical fluctuations, as shown in Fig. 4.9. The possibly asymmetric statistical uncertainties are estimated by identifying an interval containing the most probable value over which the integral of the PPD is x% of the total, corresponding to a x% Confidence Level (CL) (x = 68.3, 95.5 and 99.7). The interval is defined symmetrically around the most probable value.

Figure 4.10 shows examples of the two-dimensional contours of the PPD for the CS and PX frames in the different λ planes.

An example of the measured data distributions of the $\cos\vartheta$ and φ angular variables after background subtraction is shown in Fig. 4.11. The curves corresponding to the most extreme cases of modulation as well as the best fit scenario are also shown. This gives an indication of the sensitivity of the current dataset.

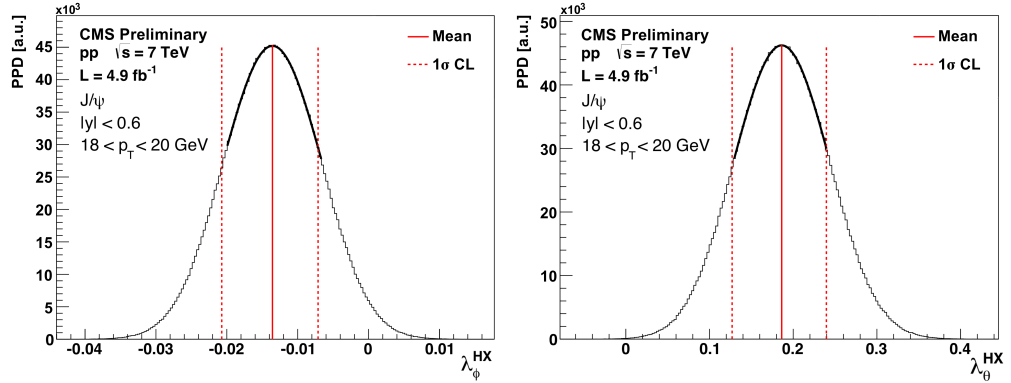


Figure 4.9: Examples for the one-dimensional projection of the PPD on λ_θ (left) and λ_ϕ (right) in the HX frame for the kinematical bin $|y| < 0.6$ and $18 < p_T < 20$ GeV for the J/ψ . The PPD is fit with a Gaussian around a small interval of the peak. The red line indicates the mean of the Gaussian while the dashed red line represents the $\pm 1\sigma$ CL interval around the peak.

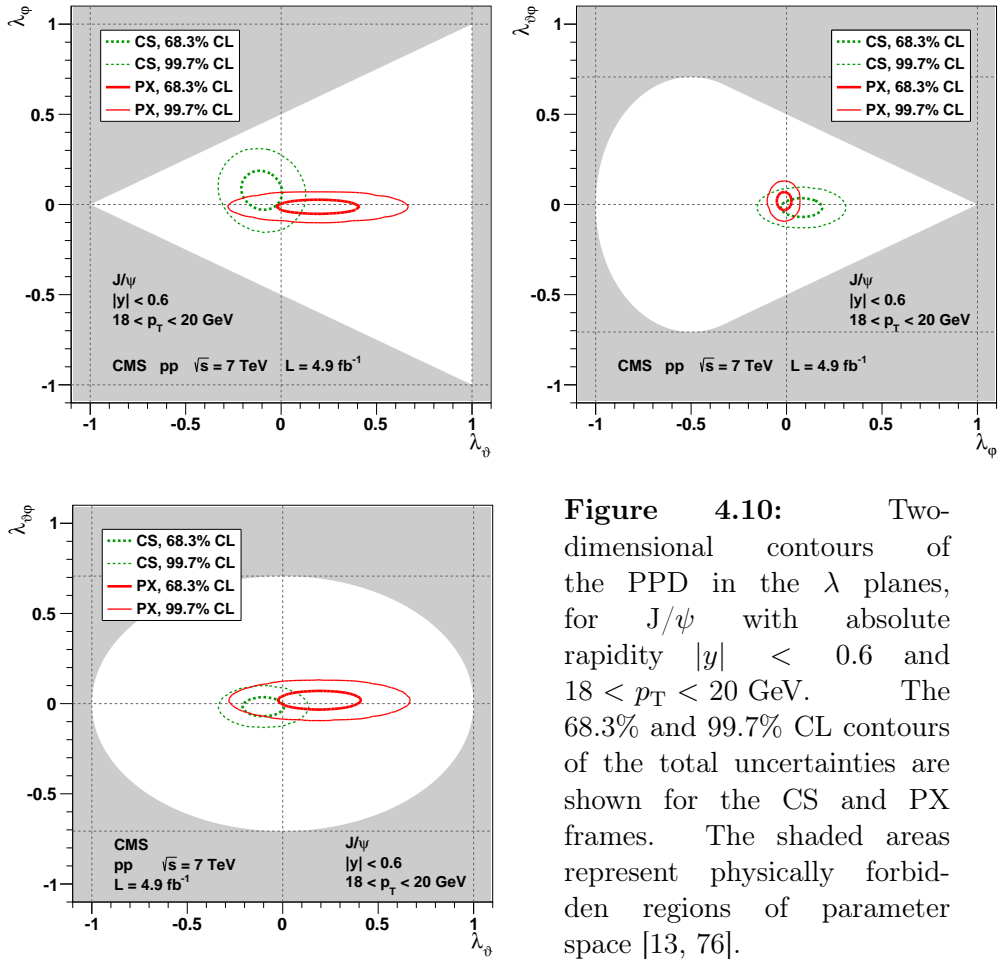


Figure 4.10: Two-dimensional contours of the PPD in the λ planes, for J/ψ with absolute rapidity $|y| < 0.6$ and $18 < p_T < 20$ GeV. The 68.3% and 99.7% CL contours of the total uncertainties are shown for the CS and PX frames. The shaded areas represent physically forbidden regions of parameter space [13, 76].

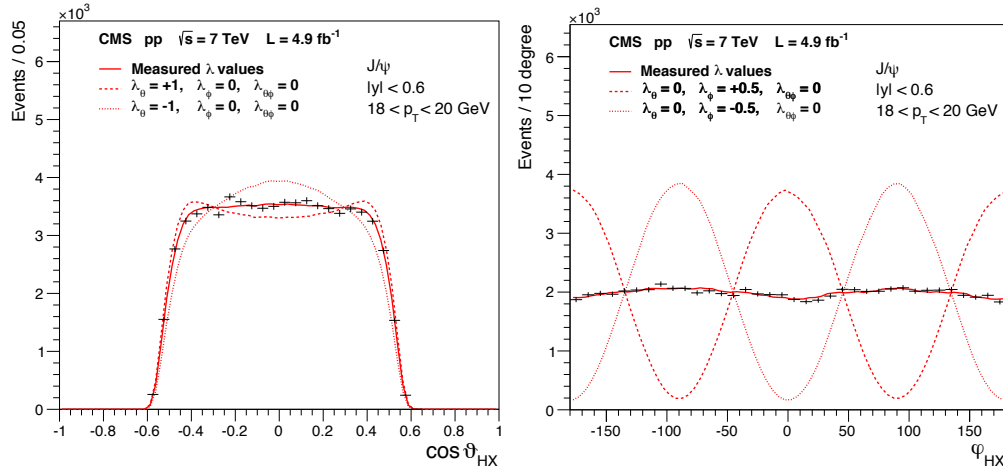


Figure 4.11: Frequency distributions of the $\cos\vartheta$ (left) and φ (right) angular variables, in the HX frame for the J/ψ in the $18 < p_T < 20$ GeV and $|y| < 0.6$ bin. The curves represent the expected distributions for two extreme polarization scenarios (dashed and dotted lines defined in the legends) and for the measured $\vec{\lambda}$ (solid lines) [13].

The framework has been tested extensively with pseudo-data studies, as described in Chapter 4.6. A more detailed discussion of the framework can be found in Ref. [77].

4.4 Fit to mass and pseudo-proper decay length

To extract the fractions of prompt, nonprompt and background events, an unbinned maximum likelihood fit is performed in two steps:

1. Fit to the dimuon mass spectrum to define the mass signal region and to evaluate the fraction of continuum background events under the resonance peak
2. Fit to the pseudo-proper decay length distribution simultaneously in the mass signal and the mass sideband regions to evaluate the fraction of nonprompt events in the prompt signal region

The fit models are built with the ROOFIT package [78] and the likelihood is maximized with MINUIT [79]. First, the SIMPLEX algorithm is run to get a fast, but not very accurate estimate of the maximum. This estimate is then used as a first guess for the computationally more expensive MIGRAD algorithm, which produces an improved estimate. In the final step, the HESSE algorithm is used to get an accurate and reliable error estimation.

4.4.1 Mass fit

The dimuon invariant mass distribution of the signal component is described by a superposition of two Crystal Ball (CB) [80] functions that describes the $\psi(nS)$ signal shape taking into account the detector resolution as well as the radiative tail from final state radiation. Two CB functions, rather than a single one, are chosen to accommodate the changing of the dimuon mass resolution within the rapidity cells.

The CB function $CB(m_{\mu\mu}|\mu_{CB}, \sigma_{CB}, n_{CB}, \alpha_{CB})$ is defined by four parameters: μ_{CB} and σ_{CB} describe the Gaussian core of the distribution; n_{CB} and α_{CB} model the non-Gaussian tail. The same mean μ_{CB} is imposed on both CB functions, but the widths are allowed to be different, σ_{CB_1} and σ_{CB_2} . The tail parameters n_{CB} and α_{CB} are strongly correlated.

To reduce the amount of free parameters, n_{CB} is fixed to the value 2.5, a value inspired by exploratory fits to the dimuon mass distribution leaving n_{CB} free and independent for both CB functions. Small imperfections caused by this specific choice of n_{CB} , if any, are compensated by α_{CB} that is left free. The α_{CB} parameter is forced to be identical for both CB functions.

The continuum mass background is modeled by an exponential function. The total dimuon mass Probability Density Function (PDF) is defined as

$$\mathcal{M}(m_{\mu\mu}) = f_{BG} \cdot \mathcal{M}_{BG}(m_{\mu\mu}) + (1 - f_{BG}) \cdot \mathcal{M}_{Sig}(m_{\mu\mu}), \quad (4.10)$$

where f_{BG} is the fraction of continuum background events in the full mass region and

$$\mathcal{M}_{BG}(m_{\mu\mu}) = e^{-\lambda_{BG} \cdot m_{\mu\mu}} \text{ and} \quad (4.11)$$

$$\begin{aligned} \mathcal{M}_{Sig}(m_{\mu\mu}) = & f_{CB_1} \cdot CB_1(m_{\mu\mu}|\mu_{CB}, \sigma_{CB_1}, \alpha_{CB}) + \\ & +(1 - f_{CB_1}) \cdot CB_2(m_{\mu\mu}|\mu_{CB}, \sigma_{CB_2}, \alpha_{CB}) \end{aligned} \quad (4.12)$$

are the background and signal PDFs, respectively. The parameter λ_{BG} is the only free parameter defining the shape of the background mass distribution. The signal mass shape is given by the two CB functions $CB_1(m_{\mu\mu}|\mu_{CB}, \sigma_{CB_1}, \alpha_{CB})$ and $CB_2(m_{\mu\mu}|\mu_{CB}, \sigma_{CB_2}, \alpha_{CB})$ and their relative normalization, f_{CB_1} and $1 - f_{CB_1}$.

It is worth noting that all PDFs mentioned in this thesis are normalized to unity; this is not explicitly shown in the equations to simplify the expressions.

The width σ_m of the dimuon mass distribution is defined as the weighted average of the widths of the two CB functions (effective width),

$$\sigma_m = \sqrt{f_{CB_1} \cdot (\sigma_{CB_1})^2 + (1 - f_{CB_1}) \cdot (\sigma_{CB_2})^2}. \quad (4.13)$$

Figure 4.12 shows examples for the fit results in the mass dimension for two p_T bins in $|y| < 0.6$, for the J/ψ and $\psi(2S)$, respectively. The fit quality is very

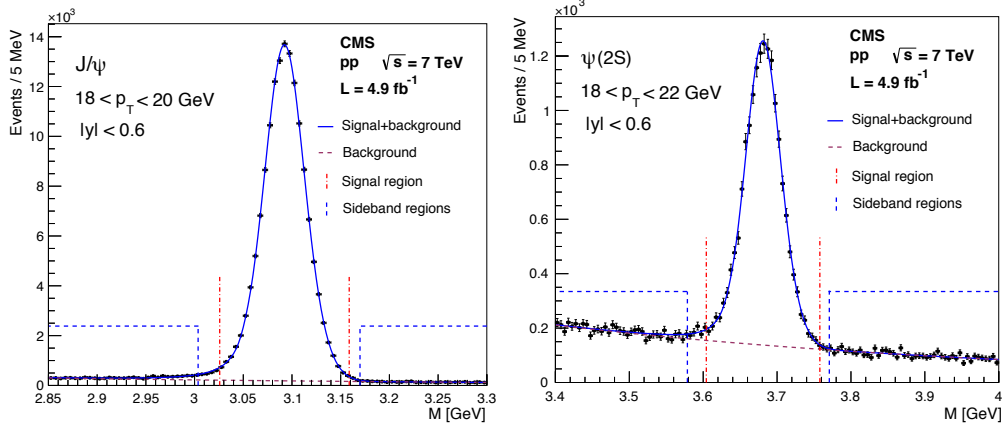


Figure 4.12: Dimuon invariant-mass distribution in the J/ψ (right) and $\psi(2S)$ (left) regions for the p_T and $|y|$ ranges indicated in the figure. The vertical lines delimit the signal region and the mass sidebands. The result of the fit is shown by the solid (signal+background) and dashed (background only) curves [13].

good for both $\psi(nS)$ states over the full kinematic range. Figure 4.13 displays the free parameters μ_{CB} , σ_m and α_{CB} defining the signal mass shape as function of p_T and $|y|$ for the J/ψ and $\psi(2S)$. All parameters show a smooth trend. Also the parameter of the background exponential λ_{BG} has a quite smooth trend as a function of p_T and $|y|$ for the J/ψ and $\psi(2S)$ as can be seen in Fig. 4.14.

4.4.2 Pseudo-proper decay length fit

The fit in the pseudo-proper decay length dimension is performed simultaneously in three mass regions. The full mass windows extend from $m_{\min} = 2.85$ GeV to $m_{\max} = 3.3$ GeV for the J/ψ and from $m_{\min} = 3.4$ GeV to $m_{\max} = 4.0$ GeV for the $\psi(2S)$. The signal mass region and the mass sidebands for both states are defined as

$$\begin{aligned}
 \text{Left SideBand (LSB): } & [m_{\min}, \mu_{CB} - n_{\sigma_m}^{LSB} \cdot \sigma_m], \\
 \text{Signal Region (SR): } & [\mu_{CB} - n_{\sigma_m} \cdot \sigma_m, \mu_{CB} + n_{\sigma_m} \cdot \sigma_m], \\
 \text{Right SideBand (RSB): } & [\mu_{CB} + n_{\sigma_m}^{RSB} \cdot \sigma_m, m_{\max}],
 \end{aligned} \tag{4.14}$$

with $n_{\sigma_m}^{LSB} = 4.0$, $n_{\sigma_m} = 3$ and $n_{\sigma_m}^{RSB} = 3.5$.

The value of $n_{\sigma_m}^{LSB}$ is larger than $n_{\sigma_m}^{RSB}$ to decrease the contamination of the background with signal events in the LSB coming from the final state radiation tail. On the other hand, increasing $n_{\sigma_m}^{LSB}$ to even larger values would reduce the number of events in the LSB and thus statistically limit the background model. The signal contamination in the right sidebands and also in the left sideband of the $\psi(2S)$ are negligible, as can be seen in Fig. 4.15. Some residual contamination in the LSB of the J/ψ is still present, which has to be taken into account when building the background model (see Chapter 4.5).

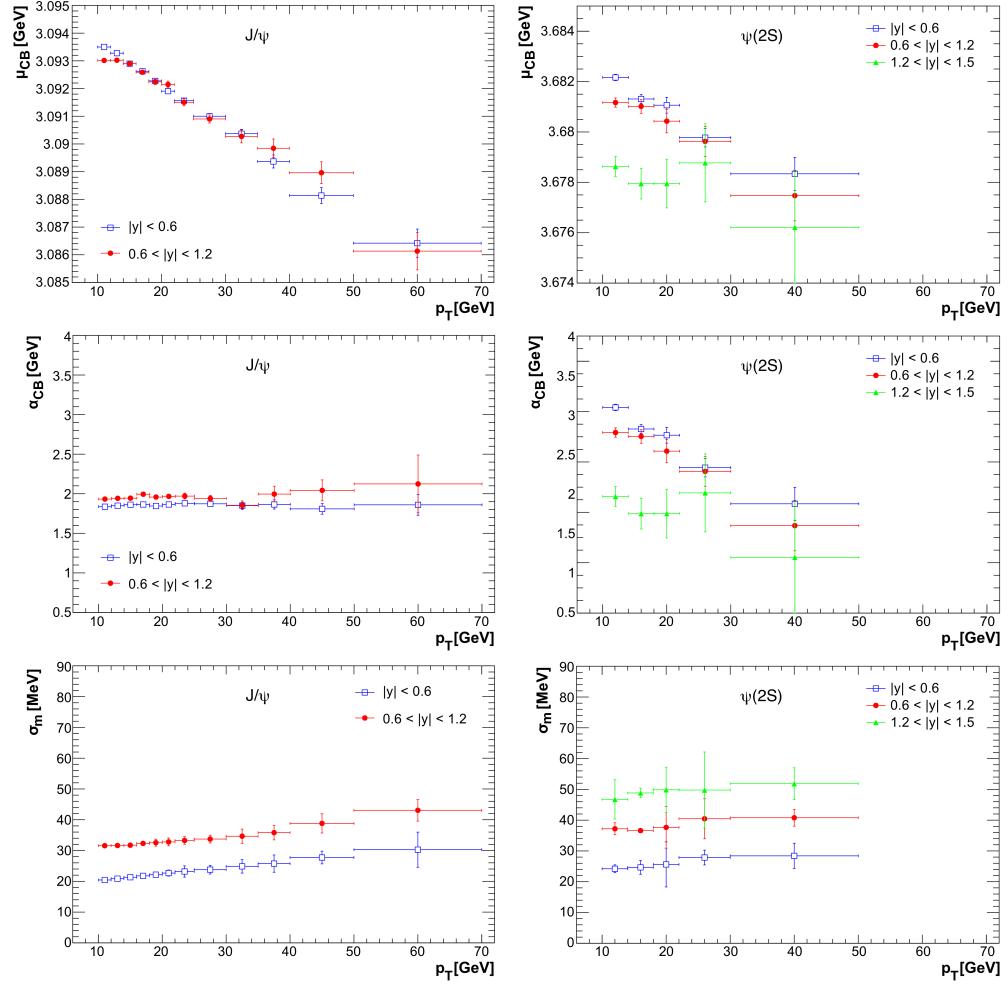


Figure 4.13: The free parameters μ_{CB} (top), α_{CB} (middle) and σ_m (bottom), defining the signal mass shape, as a function of p_T and $|y|$ for the J/ψ (left) and $\psi(2S)$ (right).

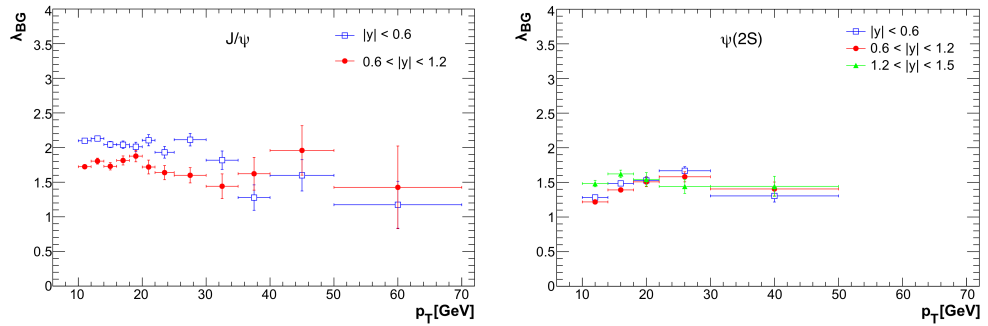


Figure 4.14: The free parameter of the background exponential λ_{BG} as a function of p_T and $|y|$ for the J/ψ (left) and $\psi(2S)$ (right).

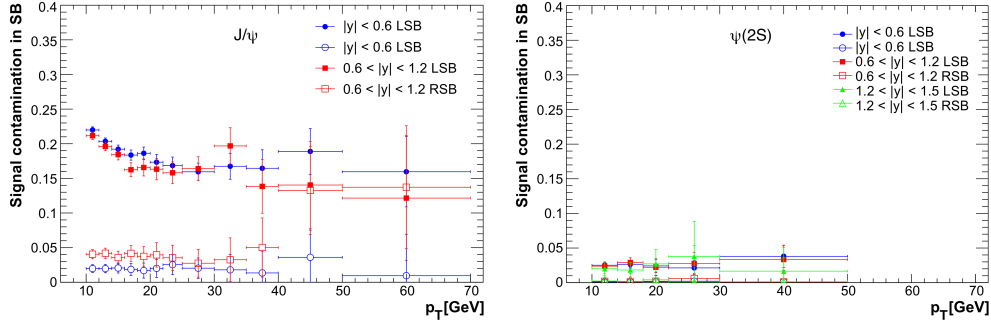


Figure 4.15: Relative yield of signal events contaminating the LSB and RSB regions for the J/ψ (left) and $\psi(2S)$ (right) as function of p_T and $|y|$.

The likelihood component describing the pseudo-proper decay length distribution, ℓ , exploits the per-event error information provided by the vertex reconstruction algorithm. The ℓ resolution function is modeled as a full expansion over N Gaussian functions G , where N is the number of events in the considered kinematic space [73]:

$$\mathcal{L}'_{Res}(\ell) = \sum_N \left[\frac{1}{\sigma_i \cdot \sigma_\ell^{\text{scale}}} G(\ell | \mu_\ell, \sigma_\ell^{\text{scale}} \cdot \sigma_i) \right]. \quad (4.15)$$

Each Gaussian function represents the uncertainty σ_i in the determination of the primary and dimuon vertices for the specific event i of the ensemble. The parameter μ_ℓ (if different from 0) describes a shift in ℓ in case of a bias. In the data, μ_ℓ is compatible with 0 in all bins, when left as a free parameter, i.e. there is no evidence for such a bias. Therefore, μ_ℓ is fixed to 0 in the final fits, to minimize the number of free parameters. The $\sigma_\ell^{\text{scale}}$ parameter (if different from 1) describes a scaling of the individual Gaussian components, in case of a systematic error in the calculation of the per-event-errors, σ_i .

This resolution model does not satisfactorily describe the tails of the resolution function. Therefore, a second Gaussian term is added, allowing two different scale factors $\sigma_{\ell_1}^{\text{scale}}$ and $\sigma_{\ell_2}^{\text{scale}}$,

$$\mathcal{L}_{Res}(\ell) = \sum_N \left[\frac{1 - f_{G_2}}{\sigma_i \cdot \sigma_{\ell_1}^{\text{scale}}} G_1(\ell | 0, \sigma_{\ell_1}^{\text{scale}} \cdot \sigma_i) + \frac{f_{G_2}}{\sigma_i \cdot \sigma_{\ell_2}^{\text{scale}}} G_2(\ell | 0, \sigma_{\ell_2}^{\text{scale}} \cdot \sigma_i) \right] \quad (4.16)$$

where f_{G_2} is the relative normalization of the second Gaussian contribution. This model remains quite simple and provides an accurate description of the data.

The prompt contribution is described with the resolution function. The non-prompt contribution is a convolution of the resolution function with a single exponential

$$\mathcal{L}_{NP}(\ell) = \mathcal{L}_{Res}(\ell' - \ell) \otimes e^{-\frac{\ell'}{\tau_{NP}}}, \quad (4.17)$$

where τ_{NP} is a variable that can be interpreted as the average (pseudo-proper) decay constant of the mixture of b-hadron decays present in the data. In principle, a superposition of several exponential functions, one for each b-hadron decaying into charmonia, should be applied. However, already a single exponential function provides a good description of the nonprompt contribution, thus significantly simplifying the analysis procedure.

The pseudo-proper decay length distribution of the dimuon-continuum background is modeled by the sum of three exponential functions, a double-sided (D), a single-sided right (R) and a single-sided left (L), convolved with the resolution function,

$$\begin{aligned} \mathcal{L}_{BG}(\ell) = \mathcal{L}_{Res}(\ell' - \ell) \otimes & \left[\frac{f_{BG_D}}{2\tau_{BG_D}} \cdot e^{-\frac{|\ell'|}{\tau_{BG_D}}} + \right. \\ & \left. + \frac{f_{BG_R}}{\tau_{BG_R}} \cdot e^{-\frac{\ell'}{\tau_{BG_R}}} \cdot \Theta(\ell') + \frac{1 - f_{BG_R} - f_{BG_D}}{\tau_{BG_L}} \cdot e^{\frac{\ell'}{\tau_{BG_L}}} \cdot \Theta(-\ell') \right], \end{aligned} \quad (4.18)$$

where τ_{BG_D} , τ_{BG_R} and τ_{BG_L} are the slope parameters of the three exponential functions, f_{BG_D} and f_{BG_R} correspond to the relative normalizations of the exponentials, and $\Theta(\ell')$ and $\Theta(-\ell')$ are step functions. The double-sided exponential describes a prompt background component while the right-sided exponential models a nonprompt contribution of the background. The left-sided exponential is added to describe the remaining tail on the negative side of ℓ .

The composite model of the background, prompt and nonprompt signal events is

$$\mathcal{L}(\ell) = (1 - f_{NP} - f_{BG}) \cdot \mathcal{L}_{PR}(\ell) + f_{NP} \cdot \mathcal{L}_{NP}(\ell) + f_{BG} \cdot \mathcal{L}_{BG}(\ell), \quad (4.19)$$

where f_{NP} and f_{BG} are the fractions of nonprompt events and dimuon continuum background events, respectively. The f_{BG} parameter is set to the value obtained in the fit to the dimuon mass distribution using a Gaussian constraint to correctly take into account its statistical uncertainty.

The Punzi term [81] in the composite pseudo-proper decay length model is not applied since the signal and background distributions basically have identical error distributions, as can be seen in the example shown in Fig. 4.16.

The same pseudo-proper decay length model is applied to both the mass signal region and the mass sidebands. But the background and nonprompt fractions are different in the three regions. While the parameters of the background pseudo-proper decay length PDF are mostly constrained by the sidebands, the parameters of the resolution function and of the nonprompt pseudo-proper decay length PDF are mostly constrained in the signal region. The ratio of prompt over nonprompt signal events is fixed to be the same in all mass regions.

The pseudo-proper decay length distributions in the sidebands are very well described by the PDF $\mathcal{L}_{BG}(\ell)$ when they are fit individually in each region. In the simultaneous fit however, the fit quality is not good if identical shape and

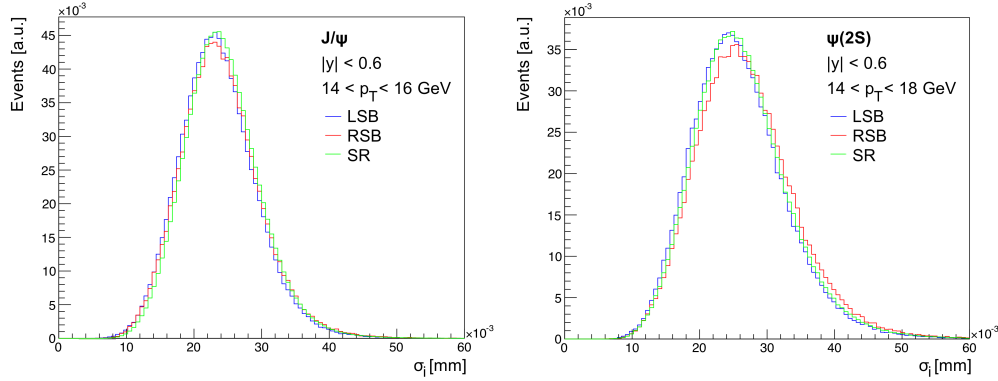


Figure 4.16: Error distributions of the pseudo-proper decay length in the mass sidebands (reflecting the background distribution) and in the signal region for the J/ψ (left) and $\psi(2S)$ (right) in the p_T bins indicated in the figure and $|y| < 0.6$. The background in the signal region is not subtracted.

normalization parameters are imposed. The independent fits to the LSB and RSB show that the normalization parameters f_{BG_L} , f_{BG_R} and f_{BG_D} as well as the shape parameter of the right-sided exponential, τ_{BG_R} , are systematically different for the two sidebands. Therefore, the simultaneous fit to all three mass regions is performed allowing these parameters to be different in the LSB and RSB regions. A linear interpolation of the values in the two mass sidebands is used for the signal region. The linear interpolation is justified by studies of the angular distributions of the background as a function of mass.

To reduce the number of free fit parameters, thus making the fit more stable, the scale parameters of the resolution function $\sigma_{\ell_1}^{\text{scale}}$ and $\sigma_{\ell_2}^{\text{scale}}$ are fixed to reasonable values, inspired by fit results where they are left free:

- $\sigma_{\ell_1}^{\text{scale}} = 0.9$ for J/ψ and $\psi(2S)$, and all rapidity cells
- $\sigma_{\ell_2}^{\text{scale}} = 1.1, 1.5$ and 3.0 for $|y(J/\psi)| < 0.6, 0.6 < |y(J/\psi)| < 1.2$, and in all y bins of the $\psi(2S)$, respectively

Due to the low fraction of background events in the J/ψ mass window, the high p_T bins ($p_T > 25$ GeV) of the J/ψ analysis do not contain enough background events to constrain all the free parameters in the simultaneous fit. As the parameter f_{BG_R} has a very smooth trend with p_T , this parameter is fixed to a constant value inspired by the results of fits where this parameter is left free.

Figure 4.17 shows examples of the results of the simultaneous pseudo-proper decay length fit in the three mass regions for the J/ψ and the $\psi(2S)$. The fit quality is good as can be seen from the pull distributions.

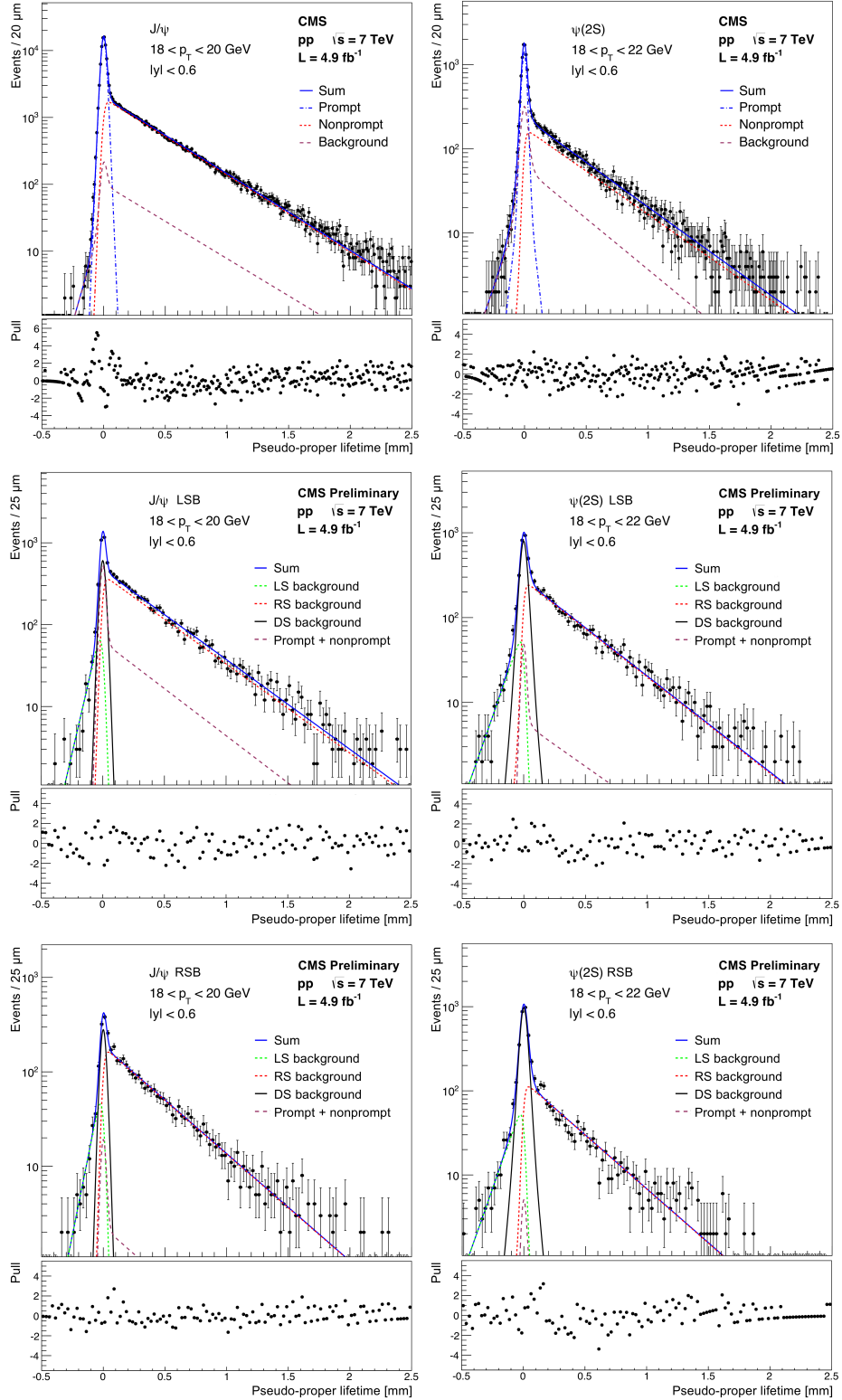


Figure 4.17: Pseudo-proper decay length distribution in the mass signal region [13] (top), the left (middle) and the right (bottom) sidebands of the J/ψ (left) and $\psi(2S)$ (right) for the p_T and $|y|$ ranges indicated in the figures. The result of the fit is shown by the solid curve, representing the sum of three contributions: prompt $\psi(nS)$ (dash-dotted), nonprompt $\psi(nS)$ (dotted), and background (dashed).

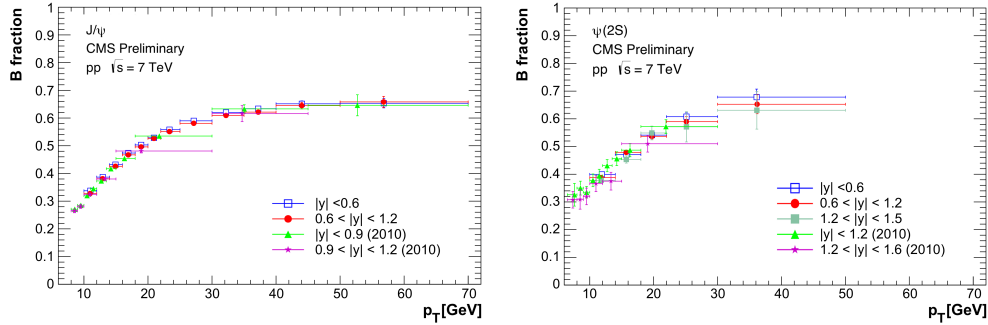


Figure 4.18: B-fractions of the J/ψ (top) and $\psi(2S)$ (bottom) as a function of p_T in bins of $|y|$ compared to the B-fractions obtained with data collected in 2010, published in Ref. [73].

4.4.3 B-fractions

As a cross-check for the pseudo-proper decay length model and the fitting procedure, the so-called B-fractions, the fraction of nonprompt to prompt plus nonprompt events, have been evaluated. They are defined as

$$f_B = \frac{n_{\text{NP}}}{n_{\text{NP}} + n_{\text{PR}}} = \frac{f_{\text{NP}}}{1 - f_{\text{BG}}}, \quad (4.20)$$

where n_{NP} and n_{PR} are the number of nonprompt and prompt events, respectively.

Figure 4.18 compares the extracted J/ψ and $\psi(2S)$ B-fractions with the results obtained in a previous CMS measurement, which is based on the 2010 data [73]. There is a good consistency between the two measurements.

4.5 Background model

Due to its simple phase-space coverage, the PX frame is chosen for the calculation of the $\cos\vartheta$ and φ distributions that are used to model the background. In order to properly subtract all background, a realistic background model is very important. For the case of the prompt $\psi(nS)$, also the nonprompt component is considered as a background. A PRrompt Signal Region (PRSR) is defined where the polarization of the prompt component is measured. The mass signal and sideband regions were already defined in Chapter 4.4.2. Additionally, prompt and nonprompt regions are introduced based on the resolution of the pseudo-proper decay length observable, σ_ℓ . The resolution is evaluated through the root mean square (r.m.s.) of the most probable transverse decay length, $L_{xy} = \ell \cdot p_T/M_\psi$, shown in Fig. 4.19.

Contrary to the variable ℓ , the L_{xy} parameter has a very simple linear dependence on p_T , well described by the function $\sigma_{L_{xy}} = a + b \cdot p_T$, with $a = 0.073$ and $b = 0.0027$. These values are fitted from the J/ψ in $0.6 < |y| < 1.2$, but also give

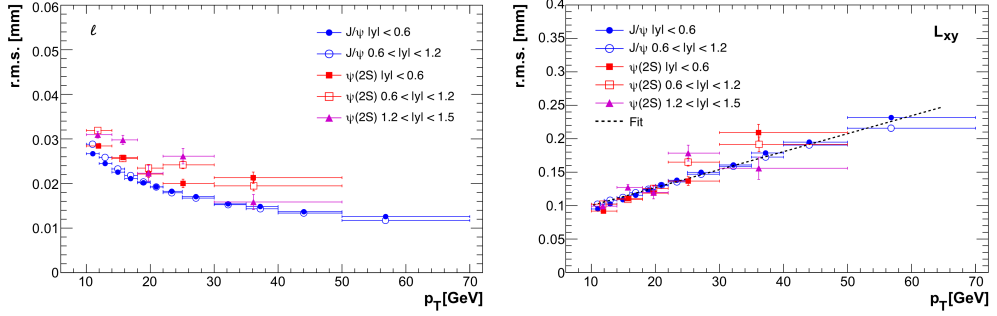


Figure 4.19: The r.m.s. of the parameters ℓ and L_{xy} as function of p_T and $|y|$ for both charmonium states.

an equally good description for the other bins. The linear function $\sigma_{L_{xy}}$ scaled with M_ψ/p_T is used to define the prompt and nonprompt regions:

$$\begin{aligned} \text{Prompt region (PRR): } & [-n_{\sigma_\ell} \cdot \sigma_\ell, +n_{\sigma_\ell} \cdot \sigma_\ell] \\ \text{Non-prompt region (NPR): } & [+n_{\sigma_\ell} \cdot \sigma_\ell, \infty]. \end{aligned} \quad (4.21)$$

where $\sigma_\ell = \sigma_{L_{xy}} \cdot M_\psi/p_T$ and $n_{\sigma_\ell} = 3.0$ for both, J/ψ and $\psi(2S)$.

In total, six regions in the two-dimensional $m_{\mu\mu} - \ell$ plane are defined, which are visualized in Fig. 4.20:

- PRompt Signal Region (PRSR)
- PRompt Left SideBand (PRLSB)
- PRompt Right SideBand (PRRSB)
- NonPrompt Signal Region (NPSR)
- NonPrompt Left SideBand (NPLSB)
- NonPrompt Right SideBand (NPRSB)

The numerical value of n_{σ_ℓ} is chosen to contain as many prompt signal events as possible in the PRSR while at the same time keeping the contaminating non-prompt and continuum background contributions small. Furthermore, this definition ensures that the contamination of prompt signal like events in the NPSR is sufficiently small to build a clean model of nonprompt events.

The specific choice of the prompt region was studied on MC and was found to have a small effect on the polarization of the prompt $\psi(nS)$ states which is covered by the systematic uncertainties.

Figure 4.21 shows an example of the fractions of the individual prompt, non-prompt and background contributions in the PRSR for $|y| < 0.6$ and both charmonium states. The prompt signal events clearly dominate the sample. The fraction of nonprompt events is kept below 20%. The fraction of continuum

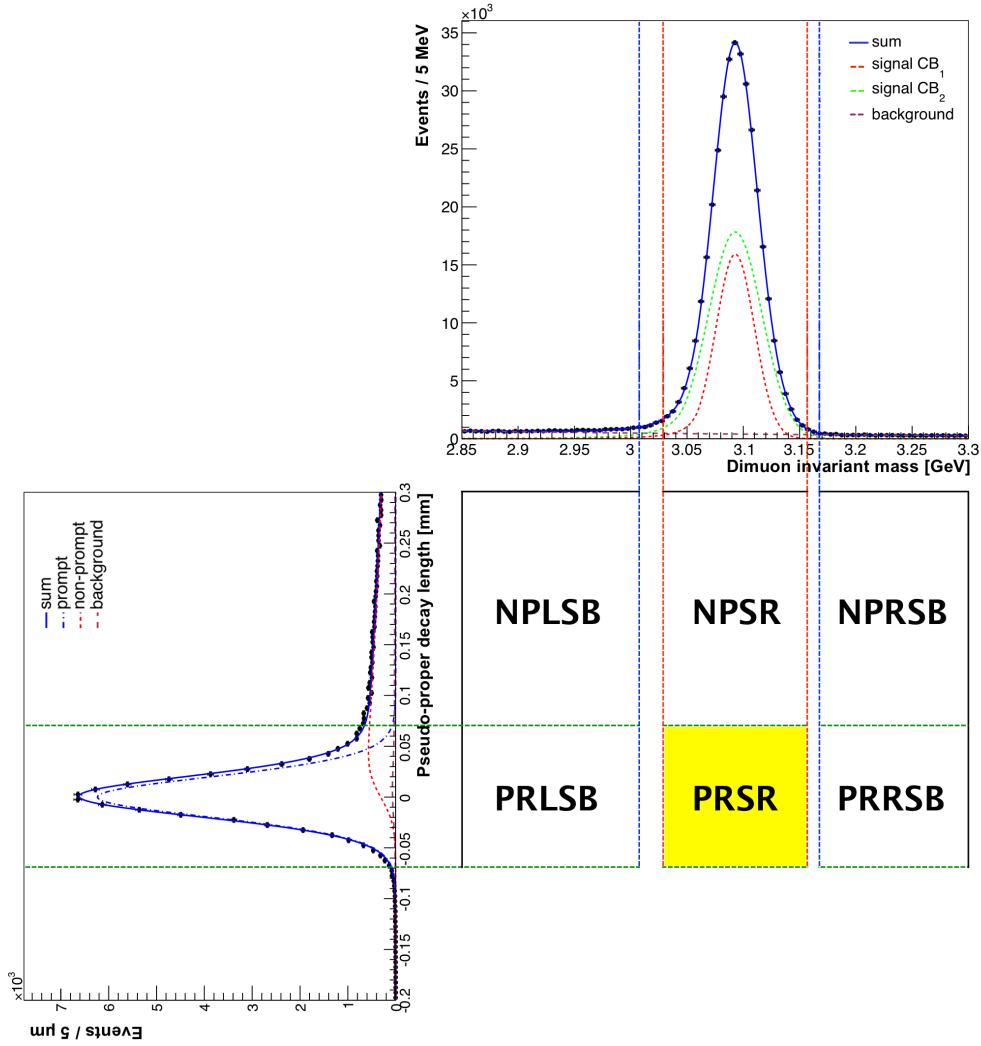
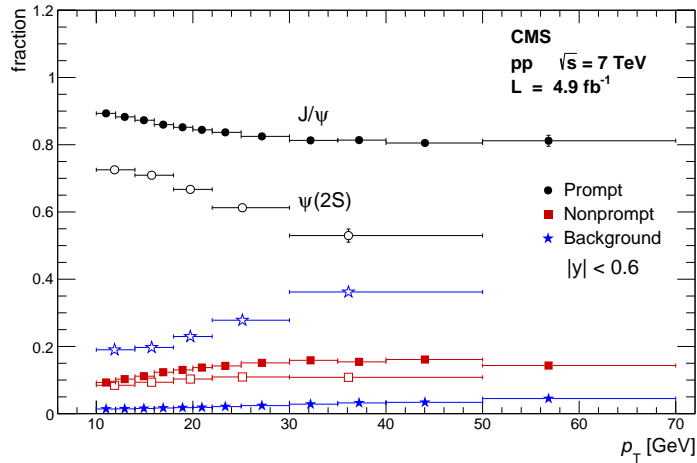


Figure 4.20: Sketch of the six individual $m_{\mu\mu} - \ell$ regions, illustrated by the mass and the pseudo-proper decay length distributions.

Figure 4.21:

Fractions of prompt, nonprompt and continuum background events in the PRSR of the J/ψ (closed symbols) and the $\psi(2S)$ (open symbols), as functions of dimuon p_T for absolute rapidity $|y| < 0.6$ [13].



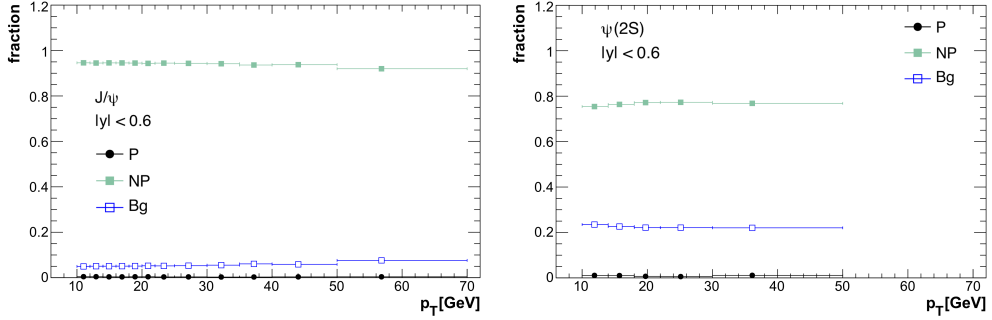


Figure 4.22: Fractions of the prompt, nonprompt and background contributions in the NPSR as a function of p_T for the J/ψ (left) and the $\psi(2S)$ (right) for absolute rapidity $|y| < 0.6$.

background events is very small (1–6%) in case of the J/ψ , while it varies between 18% and 50% depending on p_T and $|y|$ in case of the $\psi(2S)$.

Figure 4.22 shows examples of the fractions of the individual prompt, nonprompt and background contributions in the NPSR for $|y| < 0.6$. The contamination of the prompt signal events is negligible, giving a sample of only nonprompt and continuum background events. To build a pure nonprompt sample, the continuum background contribution has to be subtracted. A model for the continuum background in the NPSR is built by adding contributions from the NPLSB and NPRSB angular distributions, according to the relative importance of each sideband using f_{LSB} . The parameter f_{LSB} defines the relative importance of the LSB in the SR by linearly interpolating from the sidebands into the SR,

$$f_{LSB} = \frac{M_{RSB} - M_{SR}}{M_{RSB} - M_{LSB}}, \quad (4.22)$$

where M_{RSB} , M_{SR} and M_{LSB} are the dimuon mass median of the background events in the RSB, SR and LSB, respectively. The assumption that the background changes linearly with mass is checked by studying the angular distributions as a function of mass. Figure 4.23 shows the values of f_{LSB} obtained from

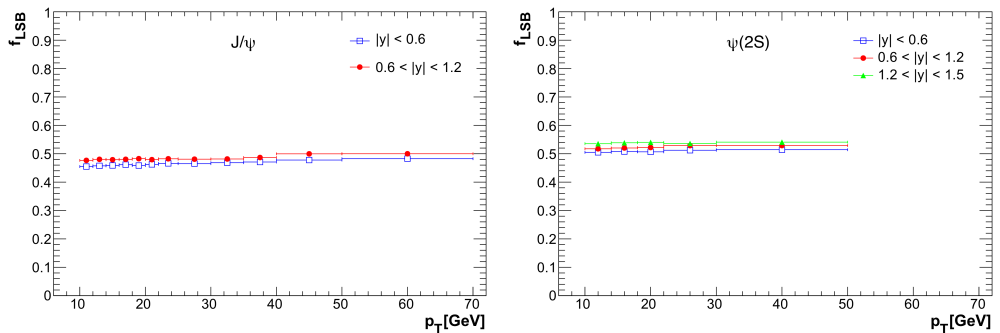


Figure 4.23: Parameter f_{LSB} showing the relative importance of the left sideband as a function of p_T and $|y|$ for the J/ψ (left) and the $\psi(2S)$ (right).

the fit results of the dimuon mass dimension. The values are close to 50% for all kinematic bins and states.

The nonprompt background model is added to the continuum background model according to their relative fractions in the PRSR to form the total model. The continuum background is built from the PRLSB and PRRSB regions, weighted with the f_{LSB} parameter. Examples of the background model are displayed in Fig. 4.24. The binning of the background model varies with the statistical precision in each p_T and $|y|$ bin of the two $\psi(nS)$ states.

4.6 Systematic uncertainties

The systematic uncertainties are directly included in the PPD by convolution. A probability distribution as function of $\vec{\lambda}$ is defined for each systematic uncertainty. The distribution describes the probability of the variations of the polarization parameters due to the uncertainty. It is defined individually for each charmonium state, kinematical bin and reference frame. It is assumed to be Gaussian in all cases except for the uncertainty related to the background model, where a uniform probability distribution is used. The inclusion of the systematic variations smears the PPD and thus directly reflects the total uncertainties in the broadened CL intervals.

The systematic uncertainties are either determined on data or pseudo-data (toy-MC) tests. The toy-MC tests proceed in three steps:

1. **Generation:** Events are generated with realistic p_T , flat $|y|$ and data-inspired $m_{\mu\mu}$ distributions. The p_T distribution follows the p_T differential cross sections measured by CMS [73] and described by Eqn. 4.3. The $m_{\mu\mu}$ distributions are generated according to Gaussians with the mean set to the quarkonium PDG masses [19] and a similar dimuon mass resolution as the one found in data. The angular distributions are generated according to the chosen (injected) distributions, usually unpolarized if not indicated otherwise. In most cases, 200 000 signal events are generated and the fraction of background events is set to zero. In the other cases, the number of signal events and the background fraction are explicitly stated in the discussion of each toy-MC test.
2. **Reconstruction:** The detector response is simulated by randomly drawing a number between zero and one from a uniform distribution and comparing it to the dimuon efficiency. If the number is smaller than the value of the dimuon efficiency, the event is kept. Only events passing the single muon fiducial cuts are considered. The background model is built with accepted and reconstructed pseudo-events in the mass sidebands and the nonprompt region.
3. **Extraction of the polarization:** The inputs generated in the first two steps are propagated to the polarization framework that determines the PPD. The efficiency chosen in this step can be different from the one in

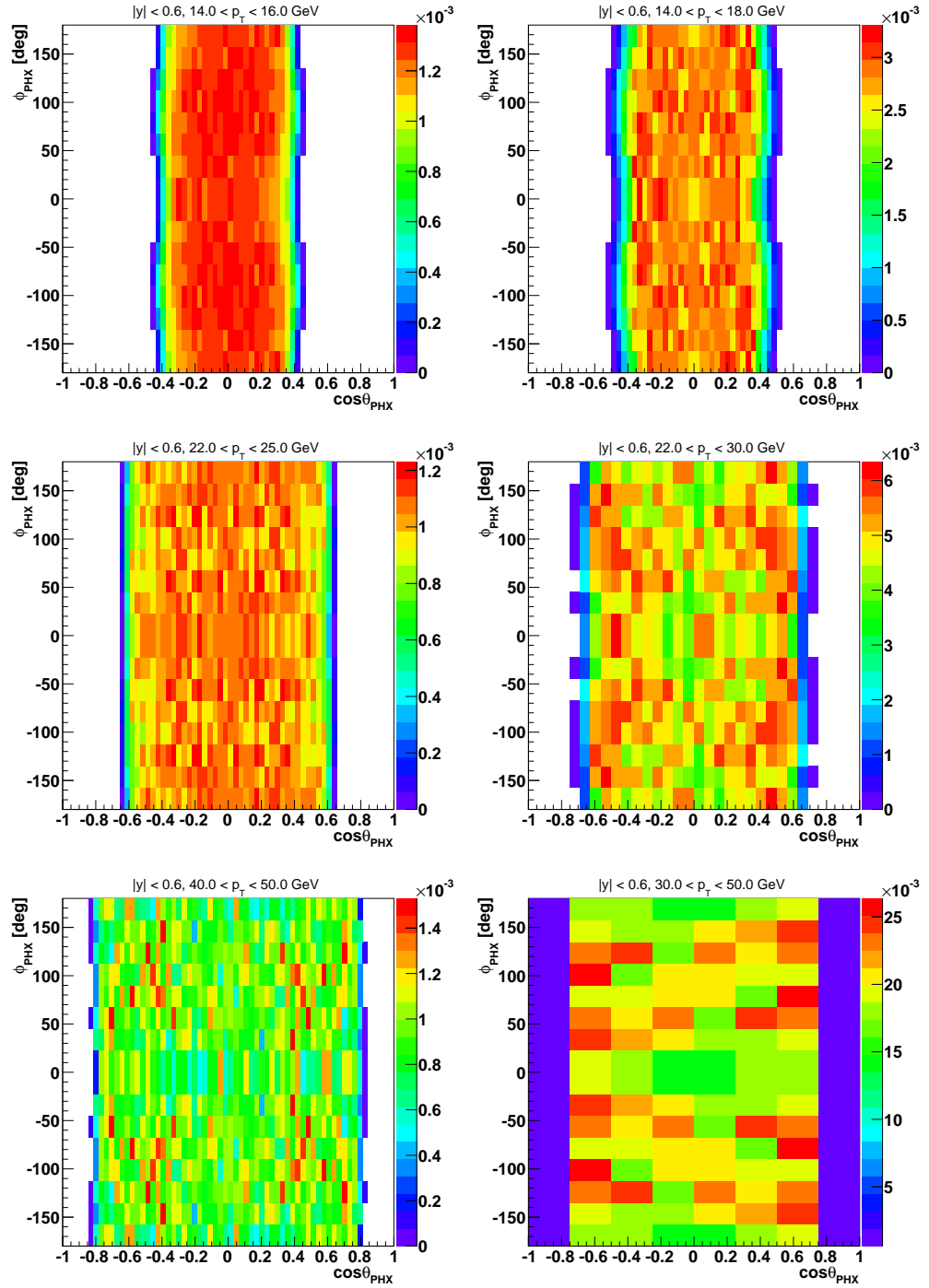


Figure 4.24: Angular distributions in the PX frame of the background events in the PRSR for the kinematical ranges indicated in the figure for the J/ψ (left) and the $\psi(2S)$ (right). The colored z-axis indicates the number of events.

the reconstruction step so that the effect of the variations of efficiencies on the polarization parameters can be determined.

All toy-MC tests performed to evaluate the systematic uncertainties rely on at least $n_{\text{toy}} = 50$ pseudo-experiments, resulting into n_{toy} results for the polarization parameters. The toy-MC bias is calculated as the median of the difference of the results with respect to the injected polarization parameters.

4.6.1 Uncertainty on the framework

The analysis framework might introduce biases due to limited statistics, the extraction of signal polarization and the subtraction of background events. Therefore, toy-MC studies are conducted to determine the variations of the three polarization parameters and the frame-invariant quantity in all frames and kinematic bins of the analysis. The studies are performed separately for each $\psi(nS)$ state. These tests are also cross-checks to see that the framework behaves in a reliable way.

To test how the framework reacts to the limited statistics in data, toy-MC studies are performed with unpolarized signal and background with the number of signal events and the fraction of background events taken from data. The small resulting bias is assigned as a systematic uncertainty.

To test the reliability of the framework to extract the correct signal polarization, four different polarizations are injected in the toy-MC studies:

1. $\lambda_{\vartheta}^{PX} = +1, \lambda_{\varphi}^{PX} = \lambda_{\vartheta\varphi}^{PX} = 0$
2. $\lambda_{\vartheta}^{PX} = +0.5, \lambda_{\varphi}^{PX} = \lambda_{\vartheta\varphi}^{PX} = 0$
3. $\lambda_{\vartheta}^{PX} = -0.5, \lambda_{\varphi}^{PX} = \lambda_{\vartheta\varphi}^{PX} = 0$
4. $\lambda_{\vartheta}^{PX} = -1, \lambda_{\varphi}^{PX} = \lambda_{\vartheta\varphi}^{PX} = 0$

The toy MC bias is again very small. The mean of the absolute values of the four evaluated biases are added in quadrature to evaluate the systematic uncertainty due to the extraction of the signal polarization.

To test the ability of the framework to reliably subtract the background events, a realistic polarization of the background and the fraction of background events taken from data are injected:

- J/ψ : $\lambda_{\vartheta}^{CS} = -0.25, \lambda_{\varphi}^{CS} = 0.15, \lambda_{\vartheta\varphi}^{CS} = 0$
- $\psi(2S)$: $\lambda_{\vartheta}^{CS} = -0.25, \lambda_{\varphi}^{CS} = 0.25, \lambda_{\vartheta\varphi}^{CS} = 0$

The small resulting toy-MC bias is assigned as a systematic uncertainty.

The three evaluated systematic uncertainties are added in quadrature and assigned as a framework-related uncertainty, $\sigma_{\text{syst}}^{\text{Framework}}$.

4.6.2 Uncertainty on the background model

The influence of changing the background model is studied on data. The parameter f_{LSB} is set to 75% and 25% instead of the default value around 50%, thus changing the importance of the angular distributions of the left sideband. The difference between the polarization parameters obtained with $f_{LSB} = 75\%$ or 25% is used to assign as systematic uncertainty, $\sigma_{\text{syst}}^{\text{fLSB}}$. It is defined as the 100% CL interval limiting a uniform probability distribution as a function of $\vec{\lambda}$ in between these extreme values.

4.6.3 Uncertainty due to the TnP model

To estimate the bias of the TnP model used to calculate the single muon efficiencies, generated events are reconstructed with MC truth efficiencies. The polarization is then extracted using MC TnP efficiencies. The bias is non-negligible at low p_T , in particular for the J/ψ . It might be caused by binning effects in the turn-on curve of the efficiencies. The bias is assigned as a systematic uncertainty, $\sigma_{\text{syst}}^{\text{TnPModel}}$.

4.6.4 Uncertainty due to the parametrization of the single muon efficiencies

The parametrization of the single muon efficiencies is provided together with three reasonable variations of the efficiencies in the negative and positive directions, which include possible imperfect assumptions of the construction of the parametrization as well as the statistical uncertainty on the TnP efficiency determination. A toy-MC study is conducted for each of the six variations. The pseudo-data samples are generated with the central parametrization. The polarization is then extracted with the corresponding variation. The means of each bias evaluated in the negative and positive directions are added in quadrature and assigned as a systematic uncertainty, $\sigma_{\text{syst}}^{\text{EffParam}}$.

4.6.5 Uncertainty due to the efficiency of the dimuon vertex fit χ^2 probability requirement

To estimate the bias coming from ε_{vtx} , the toy-MC events are reconstructed applying ε_{vtx} measured with MC. The polarization is then extracted without applying ε_{vtx} . The small resulting bias is assigned as systematic uncertainty, $\sigma_{\text{syst}}^{\text{VtxEff}}$.

4.6.6 Uncertainty related to the muon pair correlations

At $p_T < 35$ GeV, there are no dimuon correlations at low p_T , i.e. the correction factor ρ is negligible. Since there are very few events with $p_T > 35$ GeV in case of the $\psi(2S)$, ρ does not significantly affect the polarization of the $\psi(2S)$.

Therefore, the systematic uncertainty for the p_T region below 35 GeV for the J/ψ and the full kinematic region in case of the $\psi(2S)$ is evaluated separately from the high p_T region of the J/ψ . For $p_T < 35$ GeV and for the $\psi(2S)$, toy-MC events are generated and reconstructed applying ρ . The polarization is then extracted without applying ρ . The resulting bias has no trend in p_T or rapidity and is compatible for both states. Therefore, the r.m.s. of the distributions of the toy-MC biases for both, J/ψ and $\psi(2S)$, is used as global systematic uncertainty at low p_T .

The evaluation of the systematic uncertainty at high p_T for the J/ψ is based on studies using the distance variable $\Delta R_{\Delta p_T}^{\text{elliptic}}$ introduced in Chapter 4.2.3. The difference between the results of the nominal analysis (without applying a cut on $\Delta R_{\Delta p_T}^{\text{elliptic}}$, but correcting for the non-flatness of the ρ) and the ones obtained after applying a cut on $\Delta R_{\Delta p_T}^{\text{elliptic}}$ and the corresponding ρ correction, does not show any dependence on rapidity or p_T . Therefore, a constant systematic uncertainty for each polarization parameter and reference frame is assigned, calculated from the mean value of the absolute difference in the six high p_T and $|y|$ bins of the J/ψ .

4.6.7 Uncertainty due to the definition of the prompt signal region

To check if the definition of the prompt signal region of 3σ around $\ell = 0$ induces a bias, the polarization is calculated with MC events using the $\pm 3\sigma$ window and an infinite PRSR. The difference using these two options is found to be small. It is assigned as a systematic uncertainty, $\sigma_{\text{syst}}^{\text{nSigmaLifetime}}$.

4.6.8 Summary of systematic uncertainties

Figures 4.25, 4.26 and 4.27 show the squared statistical uncertainties on the negative side and the squared systematic uncertainties on the positive side, for the J/ψ and the $\psi(2S)$ in the different rapidity bins. The individual systematic uncertainties are assumed to be uncorrelated. The total uncertainties in the measurements of the individual polarization parameters are dominated by systematic uncertainties at low p_T and by statistical uncertainties at high p_T , in case of the J/ψ state. For the $\psi(2S)$ meson, the measurement is always statistics limited. At low p_T , the leading systematic uncertainty is the one related to the TnP efficiencies, i.e. the TnP model and the parametrization. At high p_T , the systematic uncertainty on ρ dominates.

4.7 Cross-checks

A wide range of cross-checks are performed, also in the context of obtaining the systematic uncertainties. A final check of the whole analysis chain consists of evaluating the differences between the frame invariant quantity $\tilde{\lambda}$ in the three

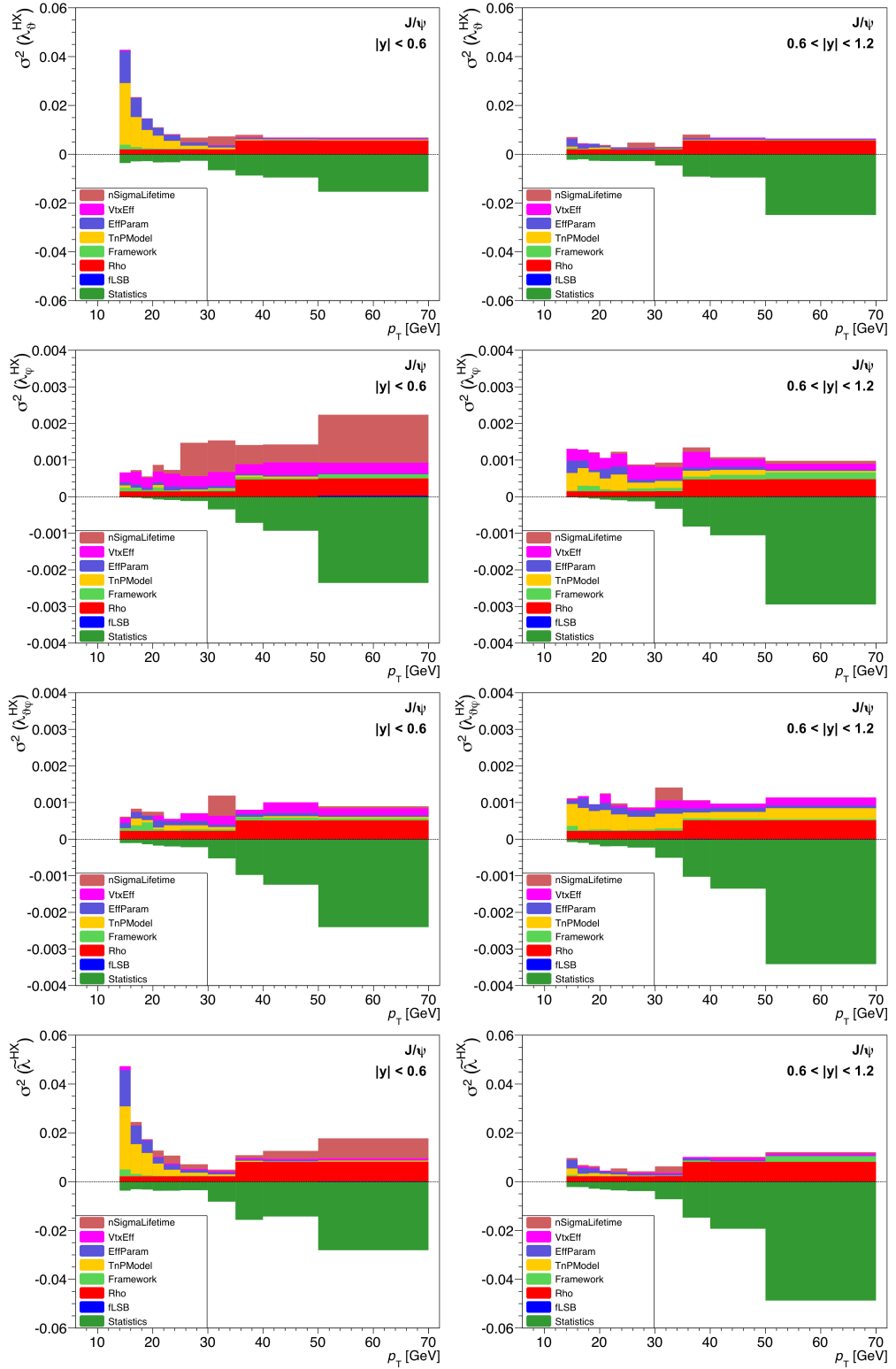


Figure 4.25: Squared systematic uncertainties displayed on the positive side and squared statistical uncertainties on the negative side for the parameters λ_ϑ , λ_φ , $\lambda_{\vartheta\varphi}$ and $\tilde{\lambda}$ (top to bottom) for the rapidity ranges $|y| < 0.6$ (left) and $0.6 < |y| < 1.2$ (right) in case of the J/ψ .

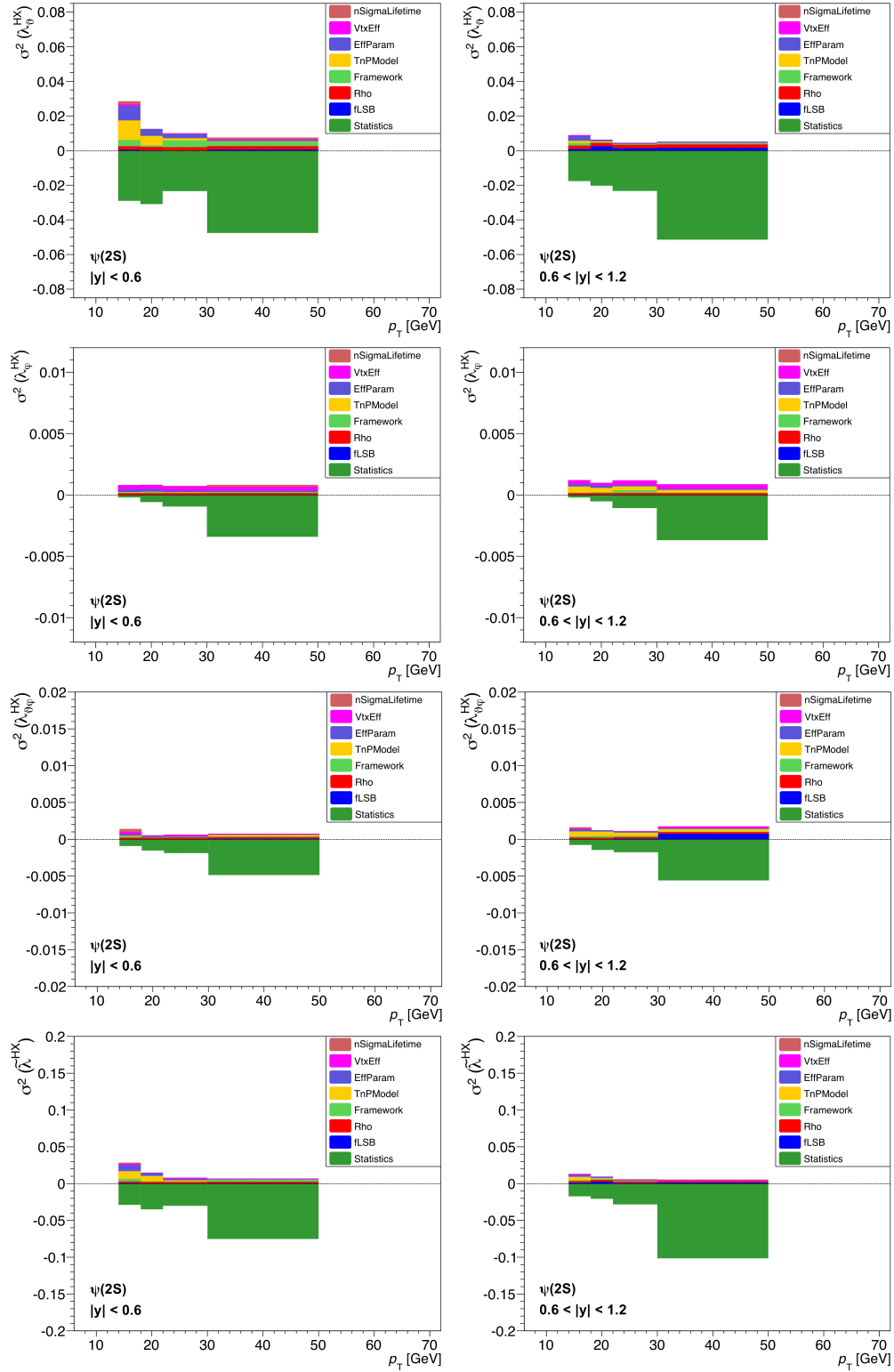


Figure 4.26: Squared systematic uncertainties displayed on the positive side and squared statistical uncertainties on the negative side for the parameters λ_{θ} , λ_{φ} , $\lambda_{\theta\varphi}$ and $\tilde{\lambda}$ (top to bottom) for the rapidity ranges $|y| < 0.6$ (left) and $0.6 < |y| < 1.2$ (right) in case of the $\psi(2S)$.

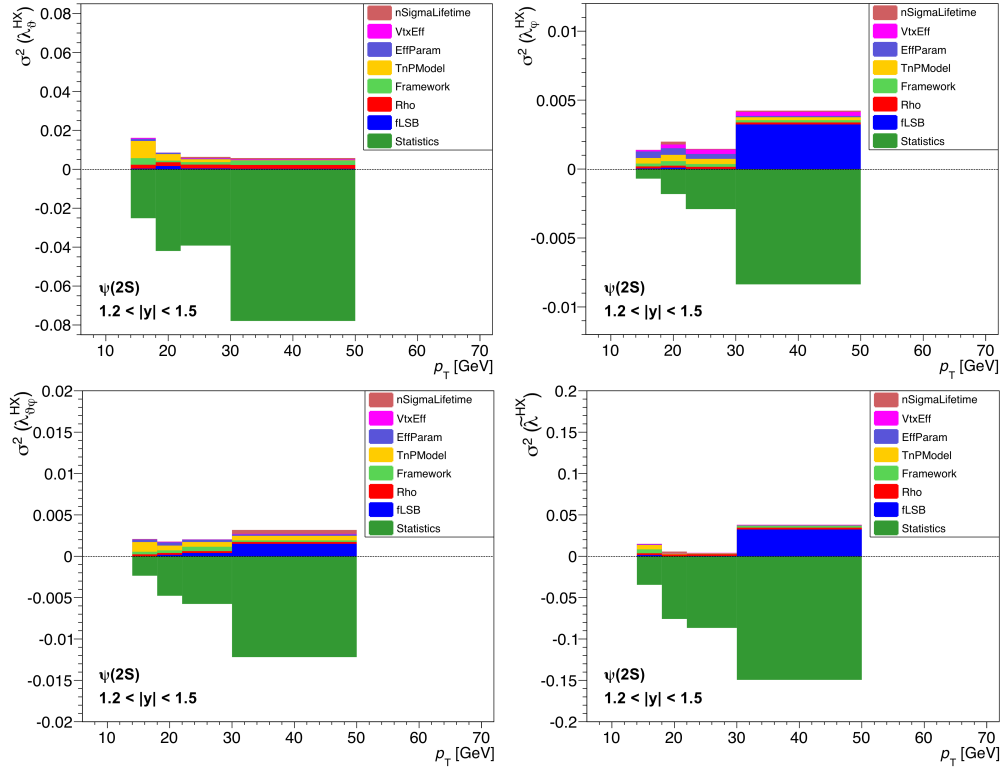


Figure 4.27: Squared systematic uncertainties displayed on the positive side and squared statistical uncertainties on the negative side for the parameters λ_ϑ (top left), λ_φ (top right), $\lambda_{\vartheta\varphi}$ (bottom left) and $\tilde{\lambda}$ (bottom right) for the rapidity range $1.2 < |y| < 1.5$ in case of the $\psi(2S)$.

reference frames. In the absence of any unaccounted systematic effect, the differences should be compatible with being zero. Figure 4.28 shows examples of the differences in $\tilde{\lambda}$ compared to the total systematic uncertainty for the J/ψ and $\psi(2S)$. The observed values are close to zero and contained within the total systematic uncertainties. Therefore, no evidence of any significant systematic effects that are not already accounted for is found.

4.8 Results

The three polarization parameters λ_ϑ , λ_φ and $\lambda_{\vartheta\varphi}$ as well as the frame invariant quantity $\tilde{\lambda}$ of the prompt J/ψ and $\psi(2S)$ are measured in three reference frames. The results are published in Ref. [13]. Figure 4.29 displays the frame invariant quantity $\tilde{\lambda}$ in the three reference frames, showing once more that the values and thus the analysis itself are consistent. Figure 4.30 shows the λ_ϑ , λ_φ and $\lambda_{\vartheta\varphi}$ parameters in the HX frame. All values are close to zero. No evidence of any strong polarization is seen.

The graphical representations of the polarization in the other reference frames and the numerical values can be found in Ref. [13].

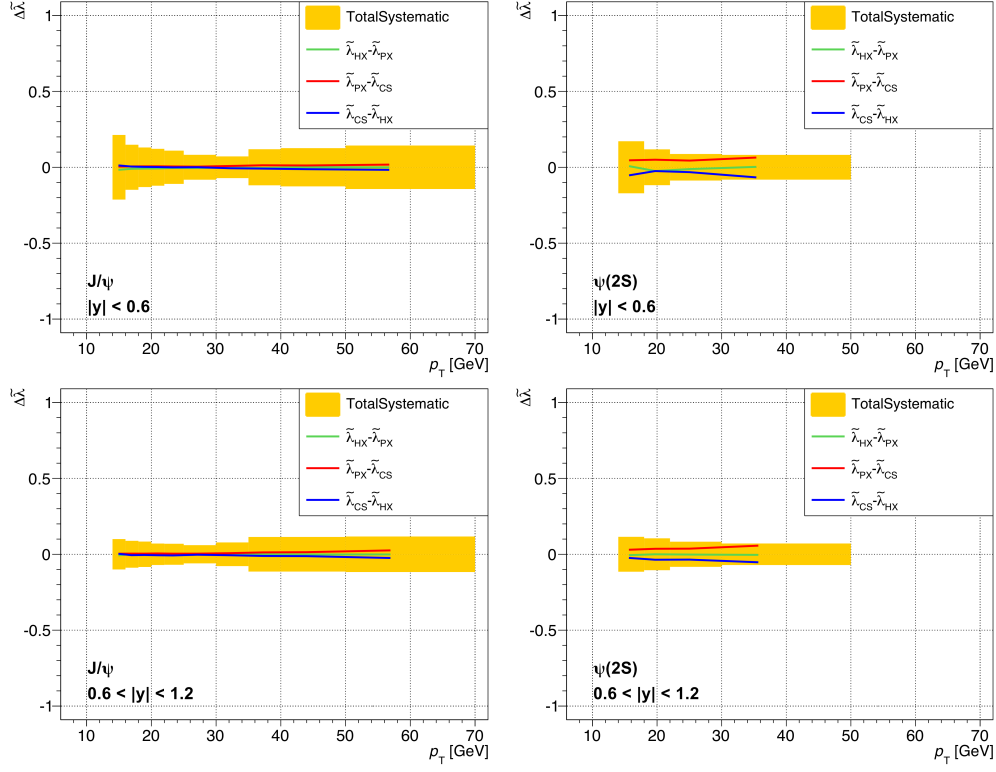


Figure 4.28: Differences between the $\tilde{\lambda}$ parameters in the different reference frames, compared to the total systematic uncertainty for the J/ψ (left) and the $\psi(2S)$ (right) in the rapidity ranges, $|y| < 0.6$ (top) and $0.6 < |y| < 1.2$ (bottom).

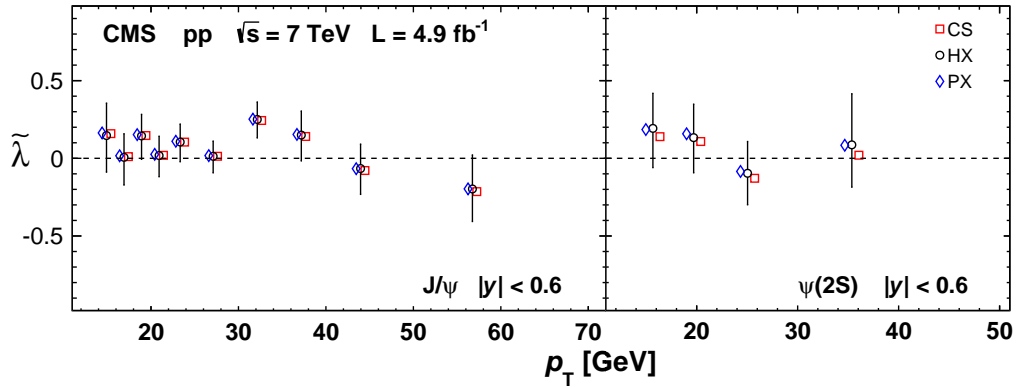


Figure 4.29: Measurements of the frame-invariant $\tilde{\lambda}$ for the $\psi(nS)$ in the HX, PX, and CS frames, for absolute rapidity $|y| < 0.6$. The error bars represent the total uncertainties at 68.3% CL in the HX frame [13].

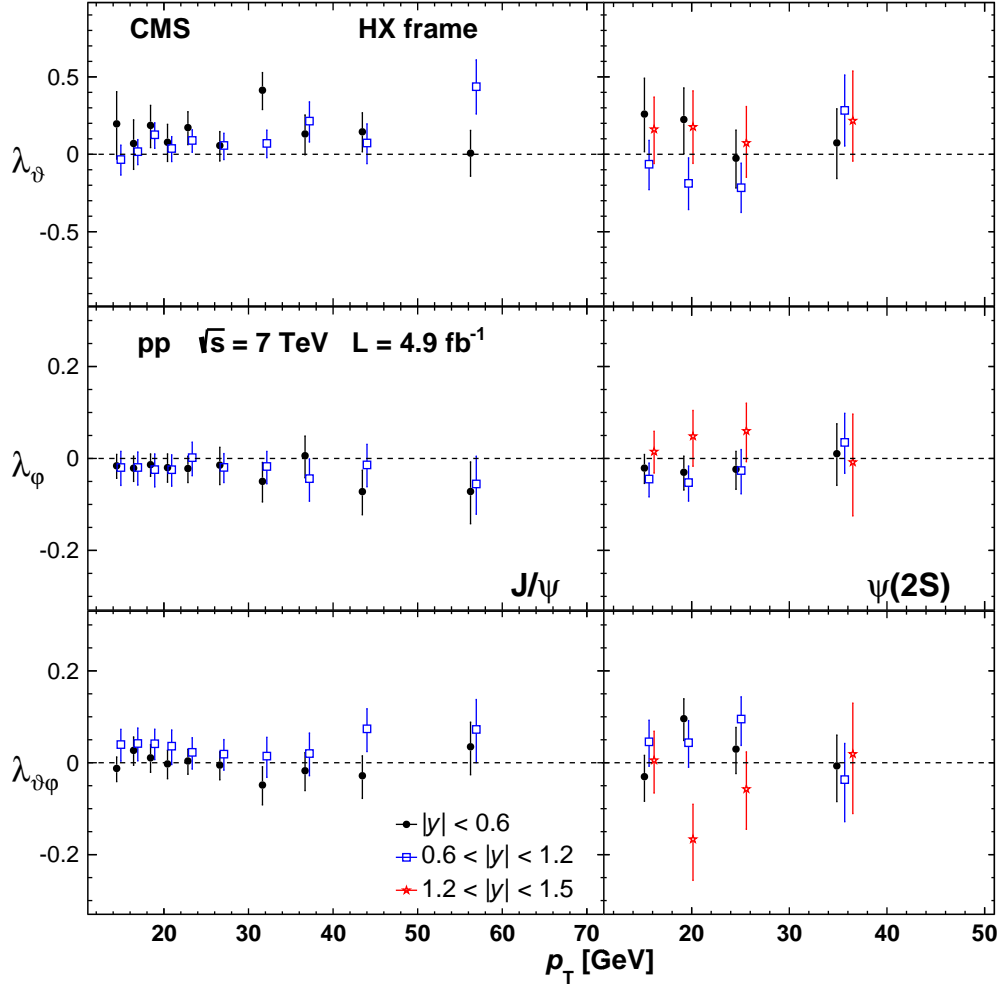


Figure 4.30: Measurements of the λ_θ , λ_ϕ and $\lambda_{\theta\phi}$ parameters (top to bottom) for the J/ψ (left) and $\psi(2S)$ (right), in the HX frame, as a function of the $\psi(nS)$ p_T , for all rapidity ranges. The error bars represent the total uncertainties at 68.3% CL [13].

CHAPTER 5

PROMPT $\psi(nS)$ CROSS SECTIONS

With four parameters I can fit an elephant, and with five I can make him wiggle his trunk.

– John von Neumann via Enrico Fermi via Freeman Dyson in Ref. [82]

This section discusses the measurement of the double-differential cross sections of the promptly produced J/ψ and $\psi(2S)$ mesons, as a function of p_T and $|y|$. The results reach from $p_T = 10$ GeV to 95 and 75 GeV for the J/ψ and the $\psi(2S)$, respectively, in four rapidity bins. They extend even further in p_T up to 120 and 100 GeV, respectively, when integrated over the interval $|y| < 1.2$. The integrated analysis is performed for four different polarization scenarios. The scaling factors to obtain the cross sections corresponding to the different scenarios are provided. The ratio of the $\psi(2S)$ to J/ψ cross sections is also determined for $|y| < 1.2$ and $10 < p_T < 100$ GeV. These measurements present the highest p_T values to date, for which the cross sections and ratio have been determined.

The prompt double-differential production cross section $\frac{d^2\sigma}{dp_T d|y|}$ times branching fraction \mathcal{B} can be written as

$$\frac{d^2\sigma(pp \rightarrow \psi(nS))}{dp_T d|y|} \times \mathcal{B} = \frac{n_{\text{PR}}(p_T, |y|)}{\mathcal{L} \cdot \mathcal{A}(p_T, |y|) \cdot \varepsilon_{\mu\mu}(p_T, |y|) \cdot \Delta p_T \cdot \Delta |y|} \quad (5.1)$$

where n_{PR} is the number of prompt signal events, \mathcal{L} the luminosity, \mathcal{A} the acceptance and $\varepsilon_{\mu\mu}$ the dimuon efficiency while Δp_T and $\Delta |y|$ represent the widths of the bins in transverse momentum and absolute rapidity. The determination of each of these variables is discussed in the following sections.

The measurement of the cross sections is based on the same inputs as the polarization analysis: The used data and MC samples as well as the event selection are discussed in Chapter 4.1 while the employed strategy to determine the single muon and dimuon efficiencies is explained in Chapter 4.2.

5.1 Definition of the kinematic cells of the measurement

The measurement of the prompt $\psi(nS)$ cross sections is performed in four equidistant rapidity intervals with a width of 0.3 in the range $|y| < 1.2$ because the J/ψ trigger was restricted to $|y| < 1.25$ in 2011. The $\psi(2S)$ trigger did not have any restrictions in $|y|$, but for simplicity the same binning is used. Moreover, the single muon efficiencies are only validated up to $|\eta| < 1.6$, also limiting the $|y|$ reach. Since the rapidity dependence of the charmonium cross sections is already known to be rather flat in rapidity, it is more interesting to extend the measurements up to the highest p_T possible at mid-rapidity instead of extending the rapidity reach.

The data sample is further divided into bins of dimuon p_T , starting at a p_T of 10 GeV due to the p_T threshold of the J/ψ trigger. The widths of the p_T bins are chosen in such a way that a sufficient number of events is contained inside each bin to be able to perform a reliable fit in the mass and pseudo-proper decay length distributions. At the same time, the bins are kept small enough to provide a detailed determination of the p_T dependence of the cross sections. At low p_T , the bin widths are 1 GeV slowly increasing towards higher values with p_T . In case of the J/ψ , 30 p_T bins are used: 20 bins, 1 GeV wide, between 10 and 30 GeV; 4 bins, 2 GeV wide, between 30 and 38 GeV; 3 bins, 4 GeV wide, between 38 and 50 GeV; and three more bins: 50–60, 60–75 and 75–95 GeV. For the $\psi(2S)$, the following 18 p_T bins are employed: 10 bins, 1 GeV wide, between 10 and 20 GeV; 4 bins, 2.5 GeV wide, between 20 and 30 GeV; and four more bins: 30–35, 35–40, 40–55 and 55–75 GeV.

5.2 Single muon and dimuon efficiencies

The single muon efficiencies are identical to the ones used in the measurement of the prompt $\psi(nS)$ polarizations. They are discussed in Chapter 4.2.1. The dimuon efficiencies follow the same strategy as outlined in Chapters 4.2.2 and 4.2.3, but are obtained in bins of p_T and $|y|$ instead of the $\cos\vartheta$ and φ intervals that are used in the context of the polarization.

5.2.1 Efficiency of the dimuon vertex fit χ^2 probability requirement

Figure 5.1 shows ε_{vtx} as a function of p_T evaluated with data and MC. The data-driven efficiency is quite flat with p_T , slightly decreasing from mid- to more forward rapidity. Given the large error bars on data, the data-driven and MC based efficiencies still seem compatible with each other. The difference of about 2% between data and MC efficiencies is assigned as a systematic uncertainty to all p_T and y bins and is big enough to cover the statistical uncertainties of this efficiency.

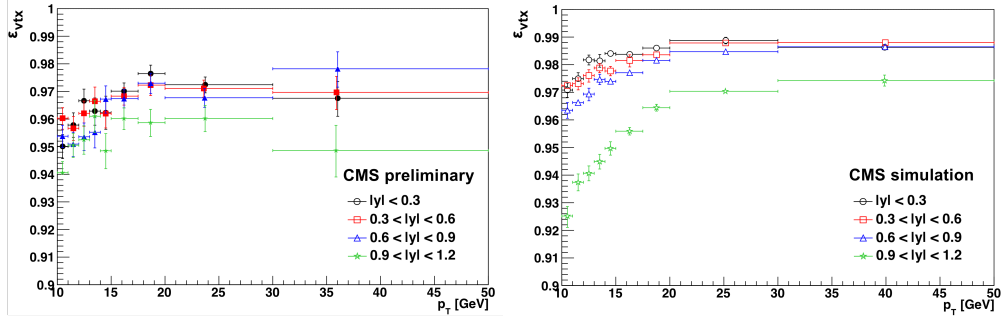


Figure 5.1: Efficiency ε_{vtx} as a function of p_{T} evaluated with data (left) and MC (right) for four rapidity regions.

Figure 5.1 displays the efficiencies in the four rapidity bins chosen for the final results. However, given the higher statistics, the MC based efficiencies are calculated in twelve equidistant $|y|$ bins, which are used in the determination of the ρ factor.

5.2.2 Muon pair correlations

The correction factor ρ accounts for muon pair correlations. In case of the cross section analysis, it is determined in bins of p_{T} and $|y|$. Figure 5.2 shows ρ as a function of p_{T} (in bins of the analysis) for four different rapidity regions. This figure is only meant for illustration purposes: The factor used to correct the yield on an event-by-event basis is calculated in much finer p_{T} and $|y|$ bins. The correction factor is almost flat and very close to unity up to $p_{\text{T}} \approx 35$ GeV, as was already seen in the context of the polarization analysis. For $p_{\text{T}} > 35$ GeV, it starts dropping fast, reaching values between 0.6 and 0.7 at $p_{\text{T}} \approx 85$ GeV.

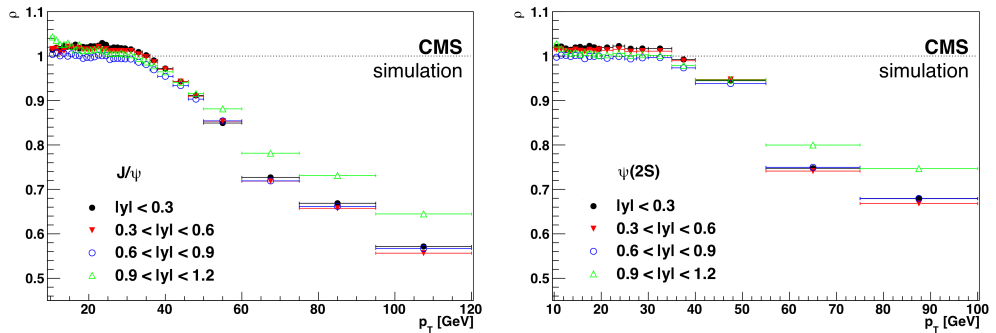


Figure 5.2: Correction factor ρ as a function of p_{T} for four rapidity regions in case of the J/ψ (left) and the $\psi(2S)$ (right).

5.3 Acceptance

In order to obtain the production cross sections without any restriction on the geometrical coverage of the CMS detector or the kinematics of the muons, the dimuon acceptance has to be taken into account. Its calculation has to be performed with MC samples. The acceptance is the fraction of detectable $\psi(nS)$ events decaying into two muons emitted in the single-muon fiducial phase space

$$A(p_T, y) = \frac{n_{\text{det}}^{\psi(nS)}(p_T, y)}{n_{\text{gen}}^{\psi(nS)}(p_T, y)}, \quad (5.2)$$

where $n_{\text{det}}^{\psi(nS)}$ is the number of $\psi(nS)$ events detected and reconstructed in the silicon tracker in a certain p_T and y bin and $n_{\text{gen}}^{\psi(nS)}$ is the corresponding total number of generated $\psi(nS)$ events. The acceptance calculation only uses generator level quantities.

The number of detectable $\psi(nS)$ events decaying into two muons in a certain phase-space window depends on the decay kinematics and the polarization of the $\psi(nS)$ mesons. The acceptance is calculated for four different polarization scenarios: unpolarized, the two extreme scenarios $\lambda_{\theta}^{\text{HX}} = \pm 1$ and a realistic polarization, which reflects the measurements published by CMS [13]. The measured polarization shows no significant trend of the three polarization parameters with p_T and $|y|$. Therefore, the weighted average of all data points in the HX frame is taken as input for the acceptance calculation. The $\lambda_{\phi}^{\text{HX}}$ and $\lambda_{\theta\phi}^{\text{HX}}$ parameters have average values compatible with zero (within less than one standard deviation). They have negligible effects on the final results and are set to zero. The $\lambda_{\theta}^{\text{HX}}$ parameter is found to be 0.1 for the J/ψ and 0.03 for the $\psi(2S)$.

Figure 5.3 shows the acceptance of the J/ψ and $\psi(2S)$ mesons for the four different polarization scenarios. The acceptance assuming the realistic polarization scenario is very close to the one assuming isotropic (unpolarized) decays.

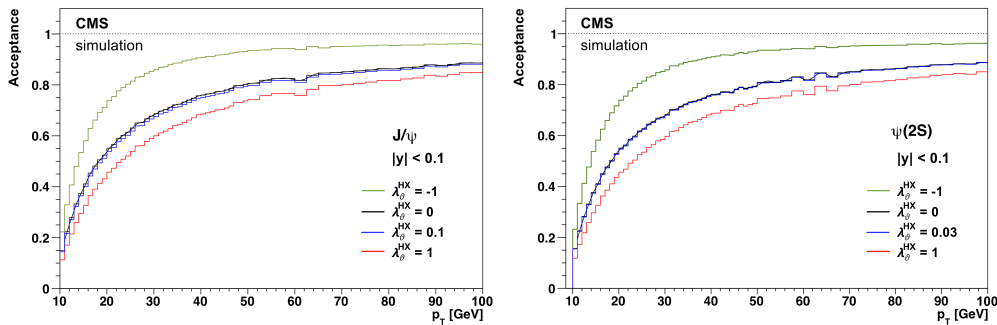


Figure 5.3: J/ψ (left) and $\psi(2S)$ acceptance as function of p_T for $|y| < 0.1$, calculated for four different polarization scenarios: unpolarized (black), $\lambda_{\theta}^{\text{HX}} = 1$ (red), $\lambda_{\theta}^{\text{HX}} = -1$ (red) and $\lambda_{\theta}^{\text{HX}} = 0.1$ and 0.03 , respectively (blue). Small deviations from a smooth curve are accounted for by using spline interpolation.

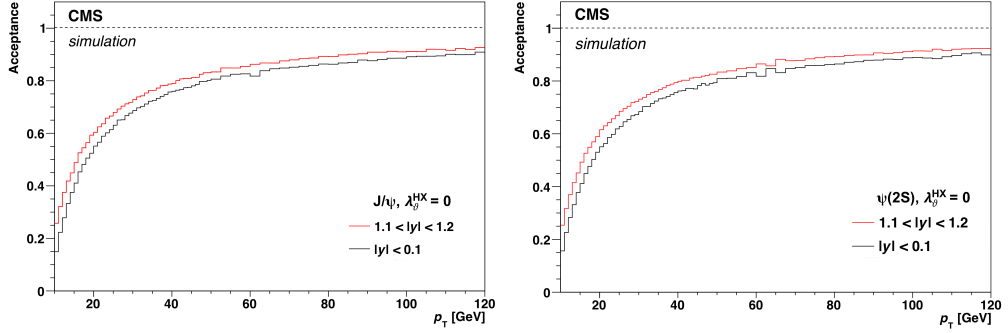


Figure 5.4: J/ψ (left) and $\psi(2S)$ (right) acceptances calculated for unpolarized dimuons as function of p_T for $|y| < 0.1$ and $1.1 < |y| < 1.2$ [83].

Figure 5.4 shows the acceptance of J/ψ (left) and $\psi(2S)$ (right) mesons calculated for isotropic decays for the two extreme rapidity bins. The dimuon acceptance increases with rapidity given that the p_T cut on the single muons is lower in the most forward rapidity bins.

The acceptances are provided in finely grained $(p_T, |y|)$ maps. They are calculated for seagull dimuons only. Therefore, a correction factor of two has to be applied to account for the cowboy dimuons that were rejected already at the trigger level.

5.4 Fit to mass and pseudo-proper decay length

The prompt, nonprompt and continuum background yields are extracted using a two-dimensional extended unbinned maximum likelihood fit in the mass and pseudo-proper decay length dimensions. The fitting routine was set up in ROOFIT.

In first approximation, the fitting functions follow the one of the $\psi(nS)$ polarization analysis in Chapter 4.4. A few modifications have been made to adapt the procedure to the specification of the present work. First of all, the numbers of signal and background events, instead of the fractions, are used as free fit parameters. Secondly, the fits are performed in narrower rapidity bins, in which the dimuon mass resolution does not change significantly. This makes it possible to use only one CB function to describe the mass peak instead of the two used for the polarization analysis.

The composite dimuon mass PDF is then defined as

$$\mathcal{M}(m_{\mu\mu}) = n_{\text{BG}} \cdot \mathcal{M}_{\text{BG}}(m_{\mu\mu}) + n_{\text{Sig}} \cdot \mathcal{M}_{\text{Sig}}(m_{\mu\mu}), \quad (5.3)$$

where n_{BG} is the number of continuum background events and n_{Sig} is the number of prompt plus nonprompt signal events and

$$\mathcal{M}_{\text{Sig}}(m_{\mu\mu}) = CB(m_{\mu\mu} | \mu_{\text{CB}}, \sigma_{\text{CB}}, n_{\text{CB}}, \alpha_{\text{CB}}) \quad \text{and} \quad (5.4)$$

$$\mathcal{M}_{\text{BG}}(m_{\mu\mu}) = e^{-\lambda_{\text{BG}} \cdot m_{\mu\mu}} \quad (5.5)$$

are the background and signal PDFs, respectively.

The pseudo-proper decay length resolution model is identical to the one used in the polarization analysis discussed in Chapter 4.4.2. The composite model of background, prompt and non-prompt signal events is given by

$$\mathcal{L}(\ell) = n_{\text{PR}} \cdot \mathcal{L}_{\text{PR}}(\ell) + n_{\text{NP}} \cdot \mathcal{L}_{\text{NP}}(\ell) + n_{\text{BG}} \cdot \mathcal{L}_{\text{BG}}(\ell), \quad (5.6)$$

where n_{PR} and n_{NP} are the numbers of prompt and nonprompt signal events, respectively, while n_{BG} represents the number of continuum background events.

In the $\psi(2S)$ case, using mass-independent $f_{BG_L} = 1 - f_{BG_D} - f_{BG_R}$, f_{BG_D} , f_{BG_R} and τ_{BG_R} parameters (describing the continuum background in the pseudo-proper decay length distribution) leads to descriptions of the pseudo-proper decay length distributions measured in the dimuon mass sidebands that are not very good. This observation was already made during the analysis of the $\psi(nS)$ polarizations, where it had no relevance. Therefore, these three parameters are allowed to change linearly with dimuon mass

$$\begin{aligned} f_{BG_D} &= f_{BG_D}^k \cdot m_{\mu\mu} + f_{BG_D}^d, \\ f_{BG_R} &= f_{BG_R}^k \cdot m_{\mu\mu} + f_{BG_R}^d, \\ \tau_{BG_R} &= \tau_{BG_R}^k \cdot m_{\mu\mu} + \tau_{BG_R}^d, \end{aligned} \quad (5.7)$$

where $f_{BG_D}^k$, $f_{BG_R}^k$ and $\tau_{BG_R}^k$ are the slope parameters, and $f_{BG_D}^d$, $f_{BG_R}^d$ and $\tau_{BG_R}^d$ are the offsets.

A better description of the data in the mass sideband regions is reached using this linear parametrization in case of the $\psi(2S)$. Not taking this mass dependence into account would possibly have induced a bias on the extraction of the signal yields. In the case of the J/ψ , no such mass dependence is observed. The corresponding slope parameters are thus set to zero.

5.4.1 Free and fixed parameters

In order to obtain reasonable fits, even at high p_T where the statistics is quite low, some parameters need to be fixed. The values of the fixed parameters were obtained by leaving the parameters free and seeing them clustering around a certain value or following an obvious trend. In some cases, also broader p_T bins were used to obtain reasonable values to fix the parameters. All parameters are summarized in Tab. 5.1.

Table 5.1: Parameters of the dimuon mass and pseudo-proper decay length fit including the description of the parameters and the value to which the parameters are fixed, for the J/ψ and $\psi(2S)$. In case the rank “value” is left free, the parameter is left floating in the fit. If “funct.” is indicated in this field, the parameter is fixed to a certain function.

Param.	Description	Value	
		J/ψ	$\psi(2S)$
n_{PR}	Number of prompt events		
n_{NP}	Number of nonprompt events		
n_{BG}	Number of continuum background events		
μ_{CB}	Expected mean of CB function	funct. ($p_T > 50$ GeV)	funct. ($p_T > 35$ GeV)
σ_{CB}	Variance of CB function, dimuon mass resolution		
n_{CB}	Tail parameter of CB function	1.9, 2.1, 2.7, 3.5	2.5
α_{CB}	Tail parameter of CB function	1.8	1.8
λ_{BG}	Background parameter of mass exponential		
μ_ℓ	Shift in pseudo-proper decay length in case of a bias	0	0
$\sigma_{\ell_1}^{\text{scale}}$	Scale parameter of the individual components of the first Gaussian G_1	0.9	0.9
$\sigma_{\ell_2}^{\text{scale}}$	Scale parameter of the individual components of the second Gaussian G_2	1.2	3
f_{G_2}	Relative normalization of second Gaussian G_2		
τ_{NP}	Slope parameter of the nonprompt contribution		0.42
τ_{BGL}	Slope parameter of the left-sided background exponential	funct.	funct. ($p_T > 35$ GeV)
τ_{BGD}	Slope parameter of the double-sided background exponential	funct. ($p_T > 9$ GeV)	funct. ($p_T > 35$ GeV)
τ_{BGR}^d	Offset parameter of the slope of the right-sided background exponential	0	
τ_{BGR}^k	Slope parameter of the slope of the right-sided background exponential		
f_{BGR}^d	Offset parameter of the relative normalization of the right-sided background exponential		
f_{BGR}^k	Slope parameter of the relative normalization of the right-sided background exponential	0	
f_{BGD}^d	Offset parameter of the relative normalization of the double-sided background exponential		
f_{BGD}^k	Slope parameter of the relative normalization of the double-sided background exponential	0	

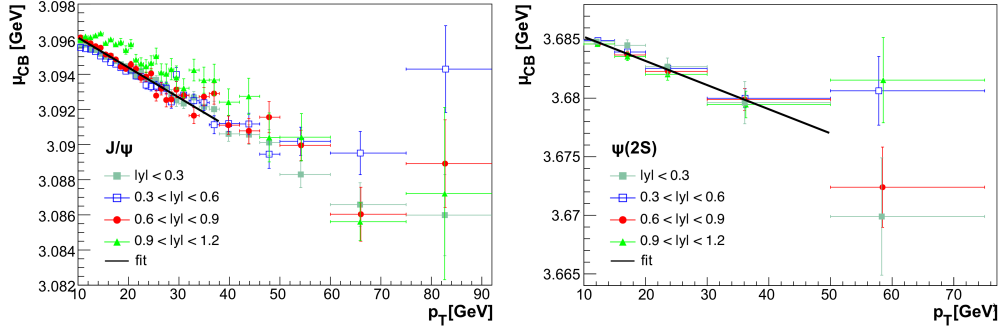


Figure 5.5: Expected mean of the CB function, μ_{CB} , as function of p_T for the J/ψ (left) and the $\psi(2S)$ (right). The data points are fit with a linear function $f(p_T) = k \cdot \mu_{CB}(p_T) + d$ at low p_T .

To get a linear or almost constant description of the p_T dependence of the parameter μ_{CB} , Muon momentum Scale calibration Fit (MuSclFit) corrections [66] are applied to the dimuon mass. A linear function is used to describe the p_T dependence of μ_{CB} as is shown in Fig 5.5. In case of the $\psi(2S)$, broader p_T bins than in the final analysis are used. The linear function is then used to fix the μ_{CB} parameter in the final mass and pseudo-proper decay length fits to better constrain them in the highest p_T bins, where the statistics is the poorest.

The two tail parameters of the CB function, α_{CB} and n_{CB} , are strongly correlated so that a good description of the tail can be achieved with different sets of (α_{CB}, n_{CB}) parameters. Figure 5.6 shows that fixing either $\alpha_{CB} = 1.8$ or $n_{CB} = 2.5$ while varying the other parameter within reason gives very similar shapes.

In some cases, the maximum likelihood optimization in MINUIT [79] fails to reach a global minimum, resulting in unreasonable parameters, when both α_{CB} and n_{CB} are left unconstrained. Therefore, α_{CB} and n_{CB} are set to reasonable values that describe the tail of the CB functions. These values are different in case of the J/ψ and the $\psi(2S)$, as can be seen in Tab. 5.1.

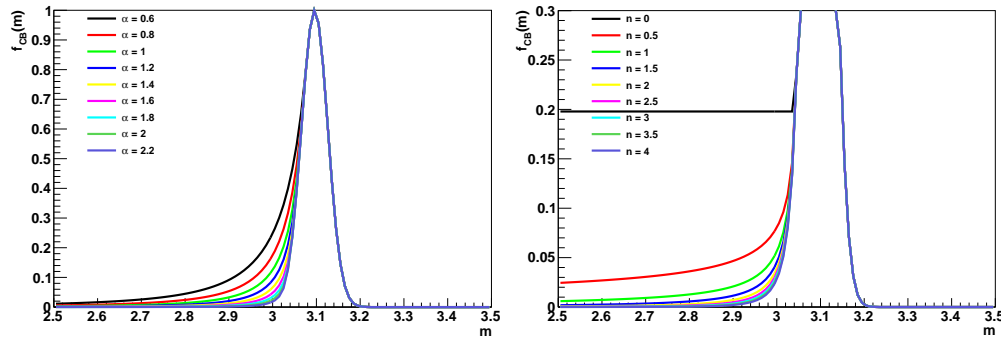


Figure 5.6: Shape of the CB function as a function of mass with different sets of (α_{CB}, n_{CB}) parameters when fixing $n_{CB} = 2.5$ (left) and $\alpha_{CB} = 1.8$ (right).

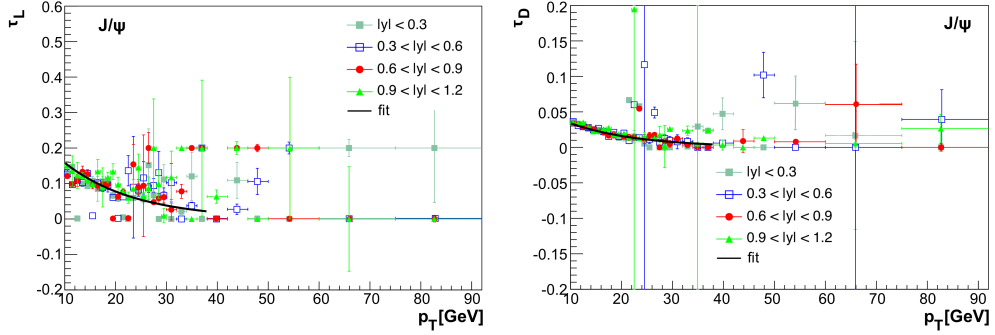


Figure 5.7: Slopes of the left-sided (left) and double-sided (right) exponentials describing the pseudo-proper decay length distribution of the background dimuons for the J/ψ : The data points of τ_{BG_D} parameter on the right side are obtained after τ_{BG_L} has already been fixed to the exponential function shown on the left side and also fitted with an exponential function.

The scale parameters $\sigma_{\ell_1}^{\text{scale}}$ and $\sigma_{\ell_2}^{\text{scale}}$ are seen to cluster around certain values when left free and are therefore fixed to these values.

In addition, the following two pseudo-proper decay length parameters are fixed to exponential functions: τ_{BG_L} and τ_{BG_D} . The two slope parameters τ_{BG_L} and τ_{BG_D} are highly correlated, in particular in case of the J/ψ . Therefore, the τ_{BG_L} parameter is fixed to an exponential function that roughly describes the values obtained in the mass and pseudo-proper decay length fit when leaving both slope parameters free. The values and the exponential fit are shown in Fig. 5.7-left. The parameter of the double-sided exponential τ_{BG_D} that is obtained after fixing τ_{BG_L} is also fit with an exponential function, as shown in Fig. 5.7-right. In the final fits, the τ_{BG_L} parameter is fixed for all p_T bins while the τ_{BG_D} is set to the exponential function for $p_T > 9$ GeV.

In case of the $\psi(2S)$, the p_T dependence of the two parameters is first obtained in broader p_T bins without fixing them. Again, the τ_{BG_L} as well as the τ_{BG_D} seem to follow an exponential trend as shown in Fig. 5.8. To constrain the mass and pseudo-proper decay length fits at high p_T , the two parameters are set to the exponential functions shown in Fig. 5.8, for $p_T > 35$ GeV.

The parameter τ_{NP} is set to 0.42 in case of the $\psi(2S)$ after observing it cluster around this value. In case of the J/ψ , τ_{NP} is left free.

The fits give good descriptions of the mass and pseudo-proper decay length dimensions as can be seen in Figs. 5.9 and 5.10, where examples of the fitted distributions projected on the mass and pseudo-proper decay length dimensions are shown. The fit quality and pulls of the distributions are very reasonable even up to the highest p_T bins. This shows that the number of free parameters is not too large or too small and that the functions used to describe the signal and background terms are suitable. The uncertainties related to the chosen fit model and the corresponding parameters are discussed in Chapter 5.5.

Figure 5.8: Slopes of the left-sided (τ_L) and double-sided (τ_D) exponentials describing the pseudo-proper decay length distribution of the background dimuons for the $\psi(2S)$. The data points are fitted with an exponential function.

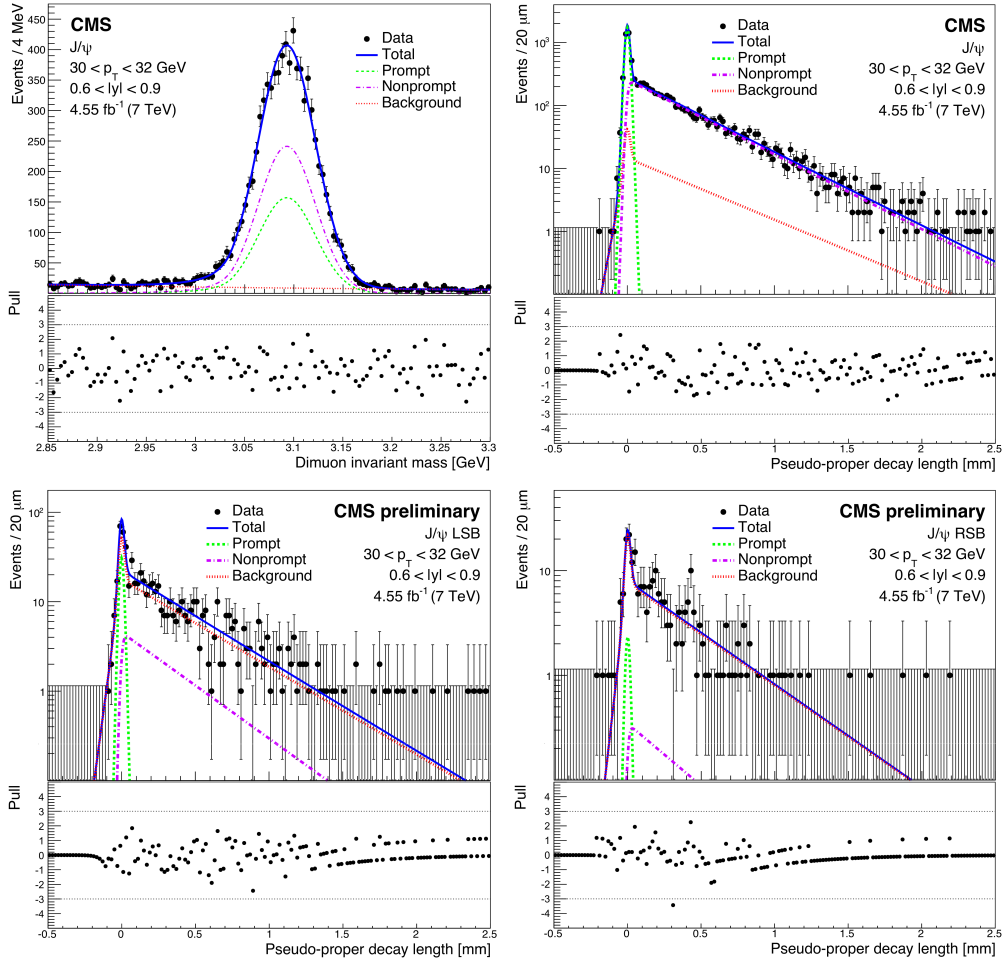
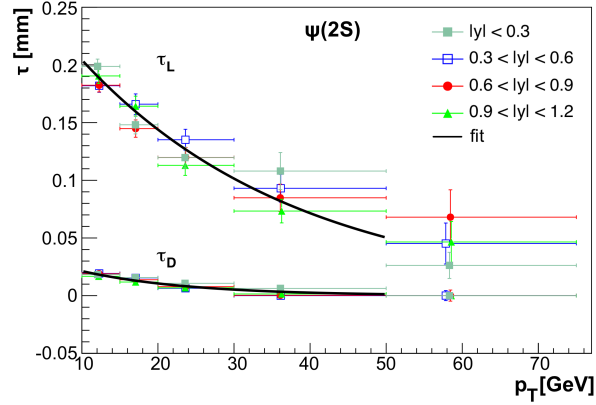


Figure 5.9: Dimuon invariant-mass (top left) and pseudo-proper decay length distribution in the signal region (top right, $\pm 3\sigma$ around the pole mass) [84] and the left (bottom left) and right (bottom right) sidebands for the J/ψ in the bin $30 < p_T < 32$ GeV and $0.6 < |y| < 0.9$. The result of the fit is shown by the solid line, representing the sum of the three contributions: prompt, nonprompt and background.

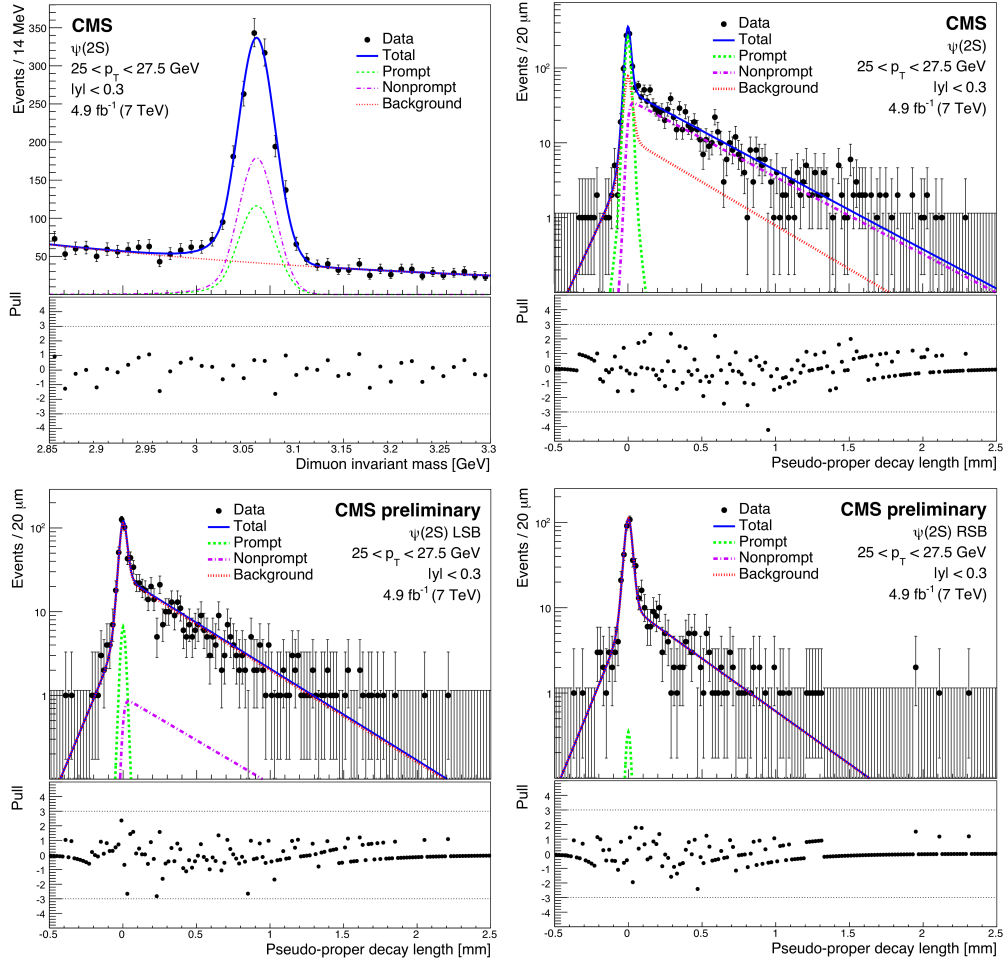


Figure 5.10: Same as previous figure for the $\psi(2S)$ and the bin $22 < p_T < 23$ GeV and $|y| < 0.3$ [84].

5.4.2 B-fractions

The B-fractions are evaluated as a cross-check of the pseudo-proper decay length models and the fitting procedure. Figure 5.11 compares the resulting J/ψ and $\psi(2S)$ B-fractions with the results obtained in the previous CMS measurement [73]. The two measurements are in very good agreement.

The quality of the results of this analysis crucially benefits from the excellent dimuon mass and pseudo-proper decay length resolutions offered by the CMS detector, in particular thanks to the silicon tracker. The dependence of the dimuon mass resolution on the dimuon p_T and rapidity is shown in Fig. 5.12 for the J/ψ and $\psi(2S)$. The corresponding plots for the pseudo-proper decay length resolution, only meant for illustration purposes, are shown in Fig. 5.13.

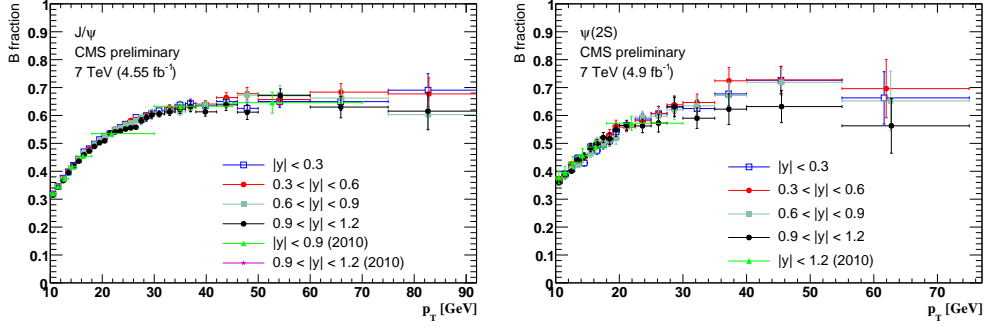


Figure 5.11: B-fractions of the J/ψ (left) and $\psi(2S)$ (right) as a function of p_T in bins of $|y|$ compared to the B-fractions obtained with data collected in 2010 in Ref. [73].

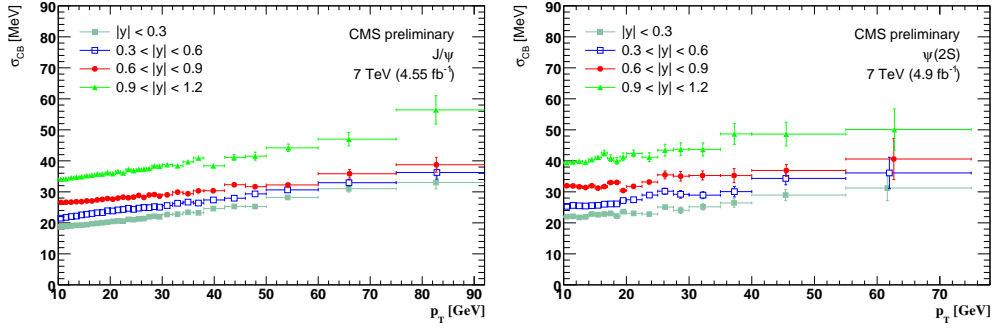


Figure 5.12: Dimuon mass resolution as a function of p_T in bins of $|y|$ for the J/ψ (left) and $\psi(2S)$ (right).

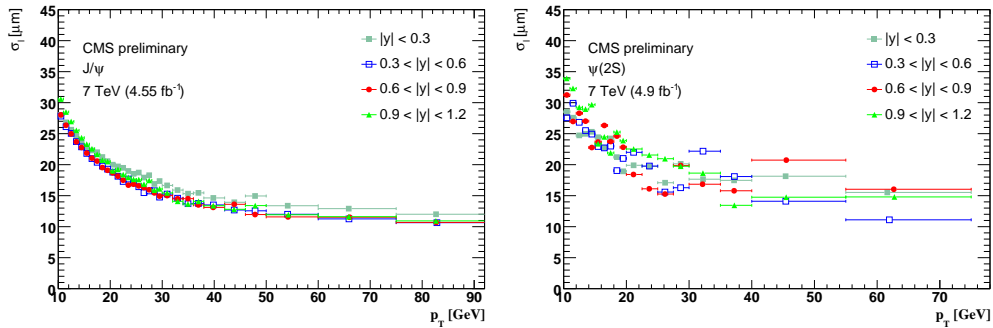


Figure 5.13: Dimuon pseudo-proper decay length resolution as a function of p_T in bins of $|y|$ for the J/ψ (left) and $\psi(2S)$ (right).

5.4.3 Fit to mass and pseudo-proper decay length for $|y| < 1.2$

To extend the p_T reach of the measurement, the cross section is also determined for the integrated rapidity bin, $|y| < 1.2$. The only difference in the fitting procedure is that instead of one CB function, a combination of four CB functions is used as signal mass shape,

$$\begin{aligned} \mathcal{M}_{Sig}(m_{\mu\mu}) = & f_{CB1} \cdot CB_1(m_{\mu\mu} | \mu_{CB1}, \sigma_{CB1}, \alpha_{CB}, n_{CB1}) + \\ & f_{CB2} \cdot CB_2(m_{\mu\mu} | \mu_{CB2}, \sigma_{CB2}, \alpha_{CB}, n_{CB2}) + \\ & f_{CB3} \cdot CB_3(m_{\mu\mu} | \mu_{CB3}, \sigma_{CB3}, \alpha_{CB}, n_{CB3}) + \\ & (1 - f_{CB1} - f_{CB2} - f_{CB3}) \cdot CB_4(m_{\mu\mu} | \mu_{CB4}, \sigma_{CB4}, \alpha_{CB}, n_{CB4}). \end{aligned} \quad (5.8)$$

Each of the four CB functions corresponds to one of the $|y|$ bins and has its parameters fixed to the values that are obtained in the respective fit. The fractions f_{CB1} , f_{CB2} and f_{CB3} are fixed to the fractions of the cross section with which each rapidity bin contributes to the total cross section. The fractions are very close to 0.25 since the cross sections do not change significantly with rapidity. In the highest p_T bin, the values of f_{CBi} and σ_{CBi} (with $i = 1 - 4$) are fixed by extrapolating from the values of the lower p_T bins. The parameter μ_{CBi} is left free in the fit.

Figures 5.14 and 5.15 show examples of the fit projections on the mass and pseudo-proper decay length distributions in case of the J/ψ and $\psi(2S)$, respectively.

5.5 Systematic uncertainties

The systematic uncertainties on the cross section stem from the extraction of the prompt signal yield, the single muon and dimuon efficiencies and the integrated luminosity. The global uncertainty on the luminosity of 2.2% is kept separated from the other uncertainties.

5.5.1 Uncertainties on the extraction of the prompt signal yield

The fitting model and the choice of the parameters might bias the extracted prompt signal yields. Therefore, the background model as well as parameters that have been fixed in the fit are varied to evaluate the corresponding systematic uncertainty. It is, however, difficult to make reasonable changes that would lead to significantly different signal yields while retaining a good fit quality. Systematic uncertainties related to the choice of the background model as well as to the selection of the values of the parameters μ_{CB} , n_{CB} , α_{CB} , τ_{NP} , μ_ℓ , $\sigma_{\ell_1}^{\text{scale}}$ and $\sigma_{\ell_2}^{\text{scale}}$ are considered. The influence of the nonprompt exponential on the prompt signal yield due to residual mis-alignment of the tracker is found to be negligible and is therefore not considered.

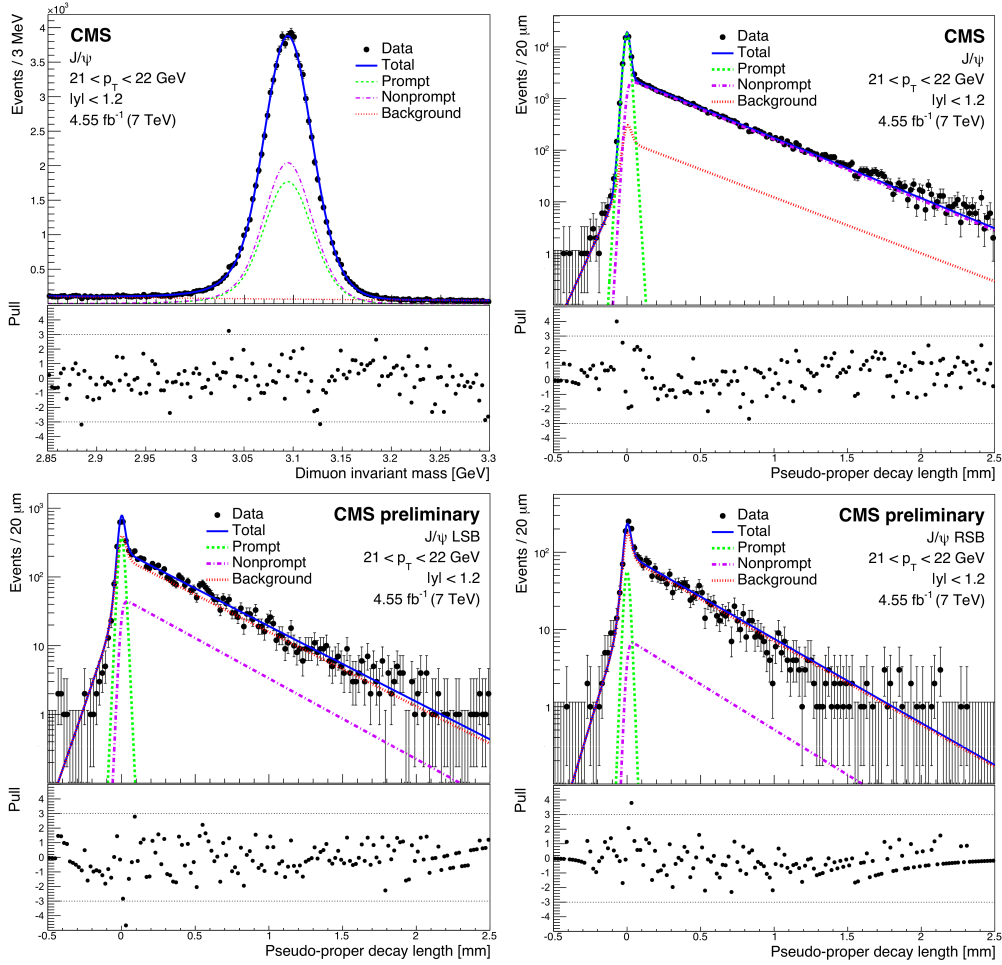


Figure 5.14: Dimuon invariant-mass (top left) and pseudo-proper decay length distribution in the signal region (top right, $\pm 3\sigma$ around the pole mass) and the left (bottom left) and right (bottom right) sidebands for the J/ψ in the bin $21 < p_T < 22$ GeV and $|y| < 1.2$. The result of the fit is shown by the solid line, representing the sum of the three contributions: prompt, nonprompt and background [84].

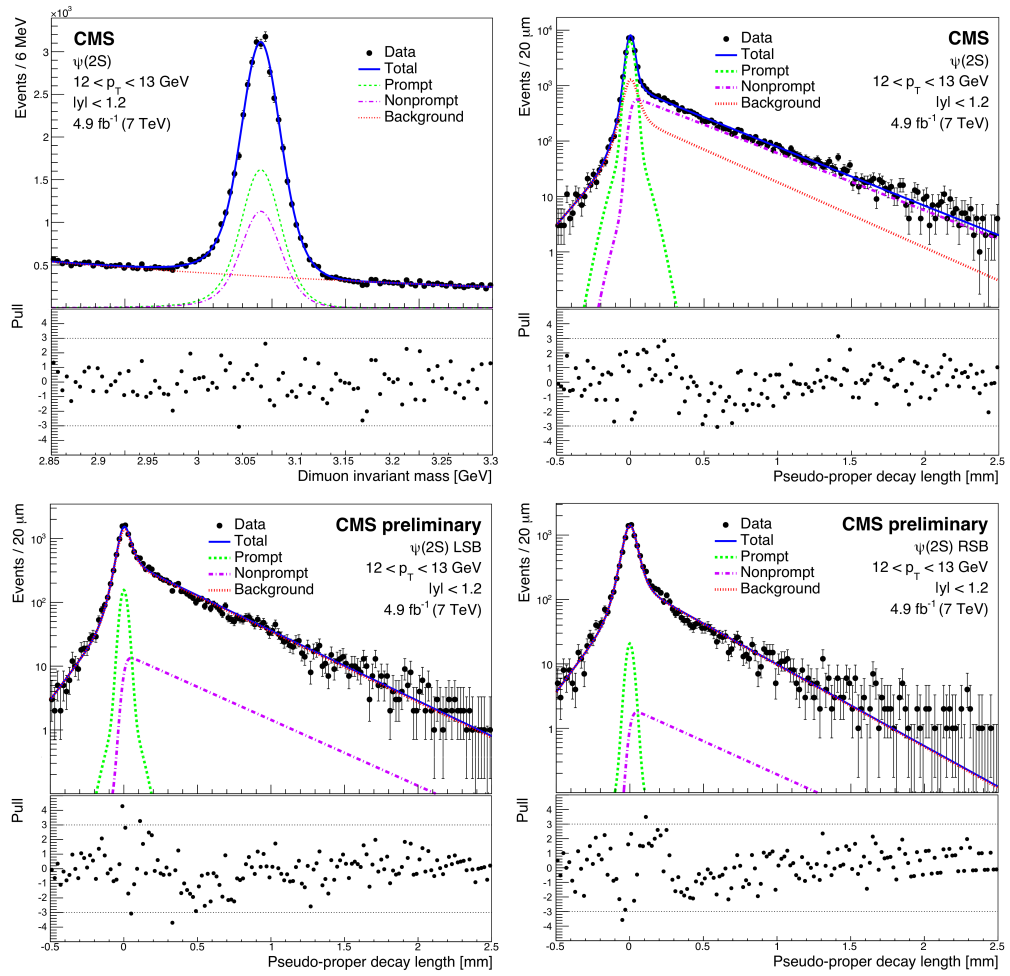


Figure 5.15: Same as previous figure for the $\psi(2S)$ in the bin $12 < p_T < 13$ GeV and $|y| < 1.2$ [84].

1. **Different background models:** The dimuon mass dimension constrains the number of background events. The mass continuum background is described by an exponential in the default analysis, denoted by the subscript d, but might as well be fitted reasonably with a linear function or a parabola. For each of these two alternatives, denoted by the subscript a, the absolute value of the relative difference in prompt signal yields, $|n_a - n_d|/n_d$, is obtained. As the two alternatives are equally reasonable, the average is calculated. It shows no rapidity dependence, therefore the average of all the four rapidity bins is assigned as systematic uncertainty on the background model. The uncertainty ranges between 1% and 5%, depending on p_T .
2. **Mean of CB function μ_{CB} :** In the high p_T bins, the parameter μ_{CB} is fixed to values linearly extrapolated from the lower p_T bins, where the parameter is left free. To evaluate the influence of fixing the parameter on the prompt signal yield, the parameter is left free. The resulting relative difference is negligible in the p_T region 50–75 GeV for the J/ψ and 35–55 GeV for the $\psi(2S)$. In the highest p_T bin of each state, the relative difference is around 0.7% for the J/ψ and 1.6% for the $\psi(2S)$.
3. **Tail parameters of the CB function n_{CB} and α_{CB} :** The tail parameters are fixed to $\alpha_{CB} = 1.9$ and $n_{CB} = 1.9, 2.1, 2.7, 3.5$ for the four rapidity bins from mid- to forward rapidity, in case of the J/ψ . As alternative scenarios, the α_{CB} parameter is left free, while the n_{CB} was increased and decreased by 0.5. The systematic uncertainties are then established from the relative differences in the same way as for the background model. They are identical for all rapidity bins and vary from less than 1% for $p_T(J/\psi) < 60$ GeV up to 2% in the highest p_T bin.

In case of the $\psi(2S)$, the parameters are by default fixed to $\alpha_{CB} = 1.8$ and $n_{CB} = 2.5$. For the alternative scenarios, α_{CB} is again left free, while n_{CB} is set to either 2 or 3. The resulting systematic uncertainty ranges from 1% to 4%, depending on p_T .
4. **Pseudo-proper decay length parameters μ_ℓ , $\sigma_{\ell_1}^{\text{scale}}$ and $\sigma_{\ell_2}^{\text{scale}}$:** Leaving the parameter μ_ℓ and $\sigma_{\ell_1}^{\text{scale}}$ free instead of setting them to a fixed value has negligible influence on the prompt signal yield. The second scale parameter $\sigma_{\ell_2}^{\text{scale}}$ is fixed to 0.7 (2.5) and 1.7 (3.5) instead of the default value 1.2 (3.0), for the J/ψ ($\psi(2S)$). Again the difference in the prompt yields is negligible. To cover any residual effects related to these three pseudo-proper decay length parameters, a p_T independent uncertainty of 1% is assigned.
5. **Slope parameter τ_{NP} :** In case of the $\psi(2S)$, the slope parameter of the exponential of the nonprompt contribution τ_{NP} is fixed to 0.42 for all p_T bins. Leaving τ_{NP} free in the fit has negligible influence on the prompt signal yield except for the highest p_T bins. Again, the average of the absolute value of the relative difference in signal yields over the four rapidity bins is taken to establish a systematic uncertainty. This uncertainty is below 1% for $p_T < 35$ GeV and increases to 2% in the highest p_T bin.

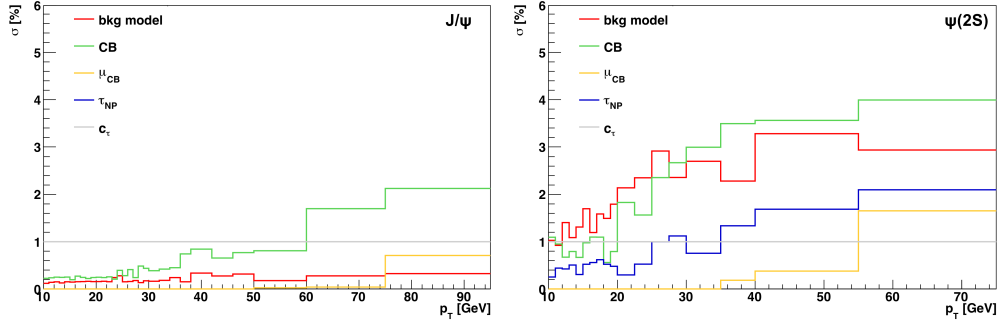


Figure 5.16: Systematic uncertainties on the extraction of the prompt signal yield for the J/ψ (left) and $\psi(2S)$ (right). The legend entry “bkg model” denotes the systematic uncertainty related to the different background models while CB represents the one related to the tail parameters of the CB function and c_τ is the one related to the parameters μ_ℓ , $\sigma_{\ell_1}^{\text{scale}}$ and $\sigma_{\ell_2}^{\text{scale}}$.

There is no corresponding systematic uncertainty for the J/ψ , where τ_{NP} is always left free.

None of the fit-related uncertainties described above show a significant dependence on rapidity. Therefore only values averaged over the four rapidity bins are considered. Their p_T dependence is depicted in Fig. 5.16 for the J/ψ and the $\psi(2S)$ mesons. The uncertainties are added in quadrature to get a total uncertainty related to the fit model and fitting procedure.

5.5.2 Uncertainties due to the TnP approach

The weighted yields are obtained using data-driven single muon TnP efficiencies corrected by the absolute difference between the average weight given by the MC truth and MC TnP efficiencies to account for the small bias induced by the TnP method. The average efficiency weight in each p_T and $|y|$ bin is calculated using the reconstructed and triggered MC events weighted once with the MC truth and once with the MC TnP efficiencies. The other correction factors remain the same. Figure 5.17 shows the difference between the average weight calculated with the MC truth and the MC TnP efficiencies as a function of dimuon p_T and $|y|$. The absolute value of the difference is additionally applied as a systematic uncertainty on the cross sections. The uncertainties are around 1-2% except for low p_T (< 12 GeV) where they are around 3%.

5.5.3 Uncertainties on the parametrization of the single muon efficiencies

The product of the data-driven single muon TnP efficiencies is parametrized as function of single muon p_T and $|\eta|$, as is explained in Chapter 4.2. In addition

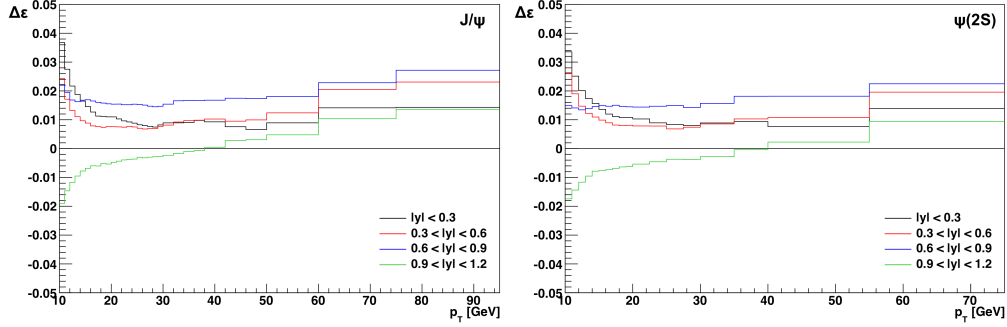


Figure 5.17: Difference between the average efficiency weight calculated with the MC truth and the MC TnP efficiencies, as a function of p_T in bins of $|y|$ for the J/ψ (left) and $\psi(2S)$ (right). The absolute values are applied as a systematic uncertainty addressing possible biases coming from the TnP approach.

to the parametrization of the data-driven TnP efficiencies, the uncertainties on the three parameters of the parametrization are evaluated and used to generate other efficiency curves, still compatible with the available measurements. These curves also include the statistical error on the data-driven TnP efficiencies.

The systematic uncertainty due to the parametrization and the statistical error of the single muon efficiencies are evaluated by recomputing the average of the inverse dimuon efficiency (not including ρ) six times. Each time, another efficiency curve where one of the three parameters is varied either in the positive or the negative direction is used. The mean of the inverse of the average dimuon efficiency, when individually changing each parameter in the positive and negative direction, is depicted in Fig. 5.18 for the rapidity range $|y| < 0.3$. In addition to the mean of each parameter, the total change, established by adding in quadrature the mean of the individual changes in the three parameters in the

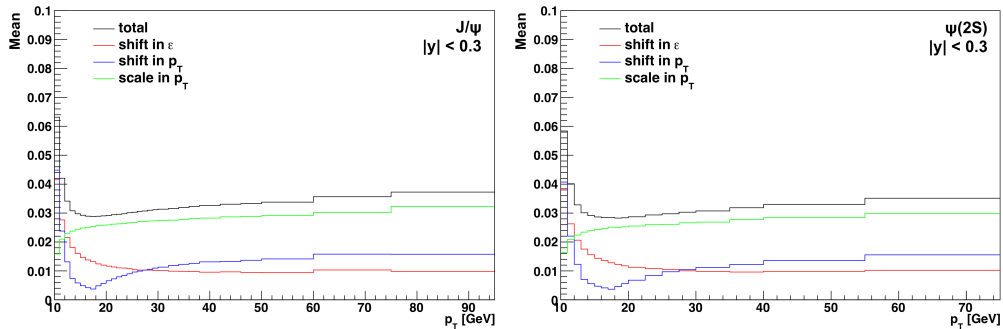


Figure 5.18: Mean of the inverse of the average dimuon efficiency, when individually changing each parametrization parameter in the positive and negative directions, as a function of p_T for the range $|y| < 0.3$ for the J/ψ (left) and $\psi(2S)$ (right). The total mean obtained by adding the means of the individual changes in the parameters in quadrature is also shown.

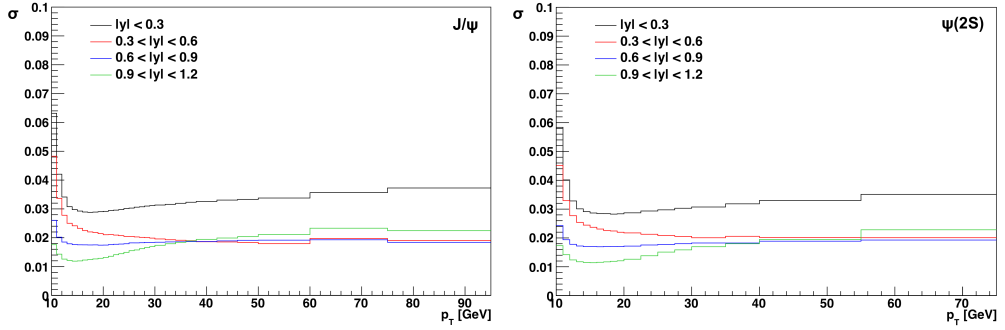


Figure 5.19: Relative systematic uncertainty on the parametrization and statistical error of the single muon efficiencies, as a function of p_T in bins of $|y|$ for the J/ψ (left) and $\psi(2S)$ (right).

positive and negative directions, is shown. This total change, displayed for all four rapidity bins in Fig. 5.19, is applied as a systematic uncertainty.

5.5.4 Uncertainties related to the muon pair correlations

As already done in the context of the polarization analysis, the systematic uncertainty related to the muon pair correlations, i.e. the correction factor ρ , is evaluated differently for the p_T region below and above 35 GeV. For $p_T < 35$ GeV, ρ is close to unity. The residual absolute difference between the value of ρ evaluated with MC and unity is up to 2%, except in the $0.9 < |y| < 1.2$ bin, where it increases to 4.3% for the J/ψ for $p_T < 12$ GeV, and to 2.7% for the $\psi(2S)$ for $p_T < 11$ GeV as is shown in Fig. 5.20. Conservatively, a 2% systematic uncertainty is assigned symmetrically for the rapidity bins $|y| < 0.9$. For the most forward rapidity bin, a p_T dependent uncertainty is assigned, increasing from 2% at $p_T = 35$ GeV to 4.3% and 2.7% at $p_T = 10$ GeV for the J/ψ and the $\psi(2S)$, respectively.

For $p_T > 35$ GeV, ρ is no longer close to unity, but decreases roughly linearly with p_T . The systematic uncertainty in this p_T region is evaluated with dimuon

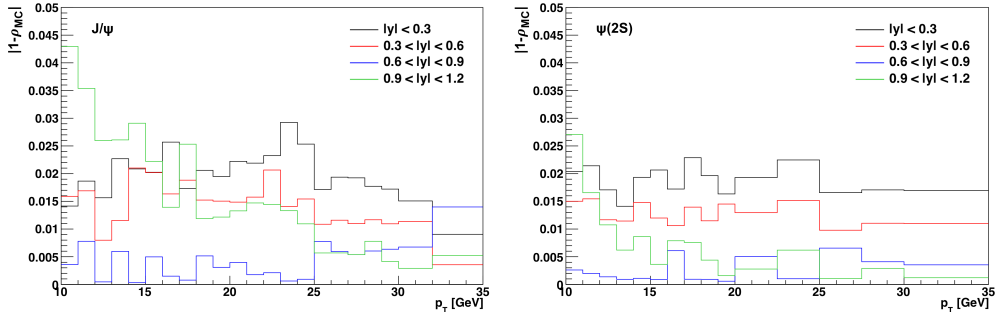


Figure 5.20: Absolute value of the difference between the value of ρ evaluated with MC and unity, as a function of p_T in bins of $|y|$ for the J/ψ (left) and $\psi(2S)$ (right).

events collected with triggers requiring a single muon with p_T above 24 GeV. Requiring only one muon at the trigger level means that there is no trigger induced inefficiency due to the presence of a second muon. However, this also limits the number of events with a muon pair. Therefore, the studies of events collected by single-muon triggers have large statistical errors and are limited to high p_T .

The determination of ρ from data is based on seagull muon pairs from the single-muon primary datasets reconstructed in the J/ψ mass window. The reconstruction is limited to the run ranges that correspond to the dimuon trigger used in the default analysis. The single muon selection cuts given in Eqn. 4.1 are applied. An extended maximum likelihood fit is performed to extract the signal yields. The signal is described with a CB function while the background is modeled with an exponential. The ρ factor is calculated as the ratio of two numbers: the number of J/ψ signal events that fire the J/ψ trigger corrected for the trigger efficiency of the lower p_T single muon (the one that did not fire the single-muon trigger) and ε_{vtx} , divided by the number of all reconstructed and selected J/ψ events. This procedure implicitly assumes that the muon with the higher p_T fired the single-muon trigger and that its efficiency cancels in the ratio. The procedure is also repeated with events in the $\psi(2S)$ mass window, but the resulting number of events is too small to provide a meaningful ρ .

Figure 5.21-left shows ρ calculated with J/ψ events collected by the single-muon triggers. The ρ values are flat in the p_T range from 25 to 40 GeV for all four rapidity bins. Within their large errors, they are close to unity, except in the most forward rapidity bin, where $\rho \approx 0.92$. Again given the large uncertainties and the various assumptions made during the derivation of the ρ factor, there is no reason to believe that the rapidity dependence is different from the one obtained in the MC evaluation. In the bin $0.9 < |y| < 1.2$, ρ seems to decrease less with p_T than in the other $|y|$ bins, similar to what was observed on MC.

Figure 5.21-right shows the relative difference $(\rho_{\text{data}} - \rho_{\text{MC}})/\rho_{\text{MC}}$. No significant differences between ρ evaluated with MC and the data-driven one are observed, given the large uncertainties on ρ_{data} . The relative differences are contained

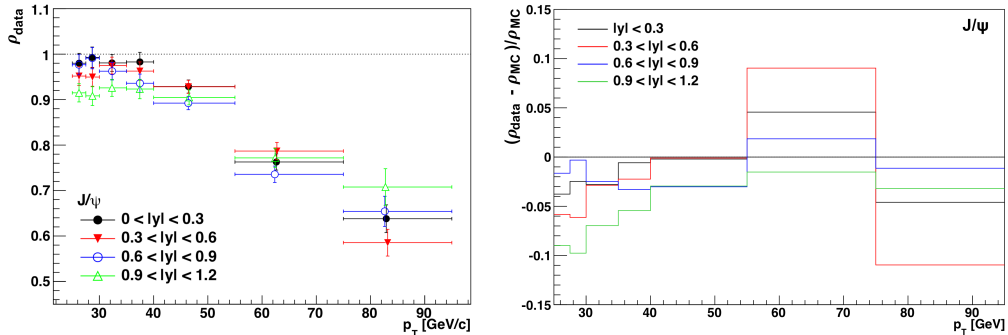


Figure 5.21: Left: Correction factor ρ evaluated with data from single-muon triggers as a function of p_T for the J/ψ . Right: Relative difference between ρ evaluated with data and MC as a function of p_T .

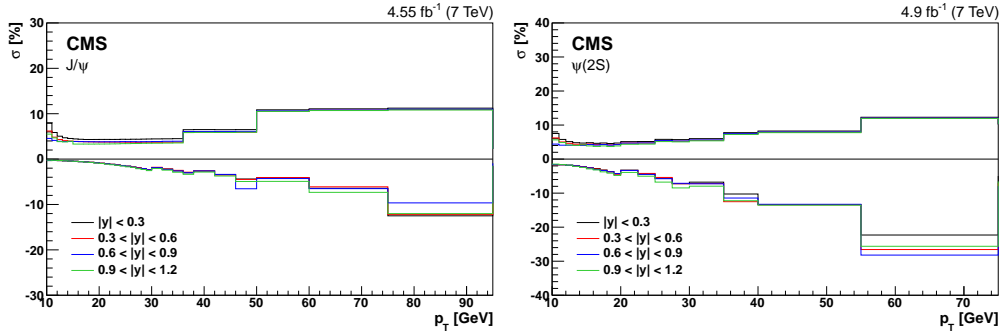


Figure 5.22: Total systematic uncertainty displayed on the positive side and statistical uncertainty on the negative side, as a function of p_T in bins of $|y|$ for the J/ψ (left) and $\psi(2S)$ (right) [76].

between -10 and +5%, except for the $0.3 < |y| < 0.6$ bin, where ρ_{data} changes in a very sudden way from the p_T bin 55–75 GeV to the bin 75–95 GeV. Given the large uncertainties on the data-driven ρ , considering a rapidity dependent systematic uncertainty is not justified. Instead, a constant uncertainty of 5% in the p_T range 35–50 GeV for the J/ψ and 35–55 GeV for the $\psi(2S)$ and of 10% for higher p_T is assigned.

5.5.5 Summary of the systematic uncertainties

In addition to the uncertainties discussed above, a systematic uncertainty of 2% is assigned independently of p_T and rapidity due to the efficiency of the dimuon vertex fit χ^2 probability requirement, ε_{vtx} . The individual systematic uncertainties are added in quadrature to get the total uncertainty. Figure 5.22 shows the statistical uncertainty on the negative and the total systematic uncertainty on the positive side. The global uncertainty of 2.2% related to the luminosity is not included. At low p_T , the systematic uncertainties dominate while at high p_T , the leading uncertainty is due to statistics.

The relative importance of each systematic uncertainty is shown in Fig. 5.23. For the p_T region above 35 GeV, the uncertainty related to the ρ factor is clearly dominating. At very low p_T , the uncertainties related to the muon efficiencies are the largest contribution in the rapidity range $|y| < 0.6$, while in the two other rapidity bins none of the systematic uncertainties is dominating.

5.5.6 Systematic uncertainties for $|y| < 1.2$

The maximum value of the four rapidity-dependent systematic uncertainties is taken as systematic uncertainty for the bin $|y| < 1.2$. This procedure is considered reasonable given that the systematic uncertainties between the four bins are very highly correlated. For the last p_T bin, only available for the range $|y| < 1.2$, the systematic uncertainty is evaluated by linearly extrapolating the values of the previous three p_T bins. Only the three previous p_T bins are used because

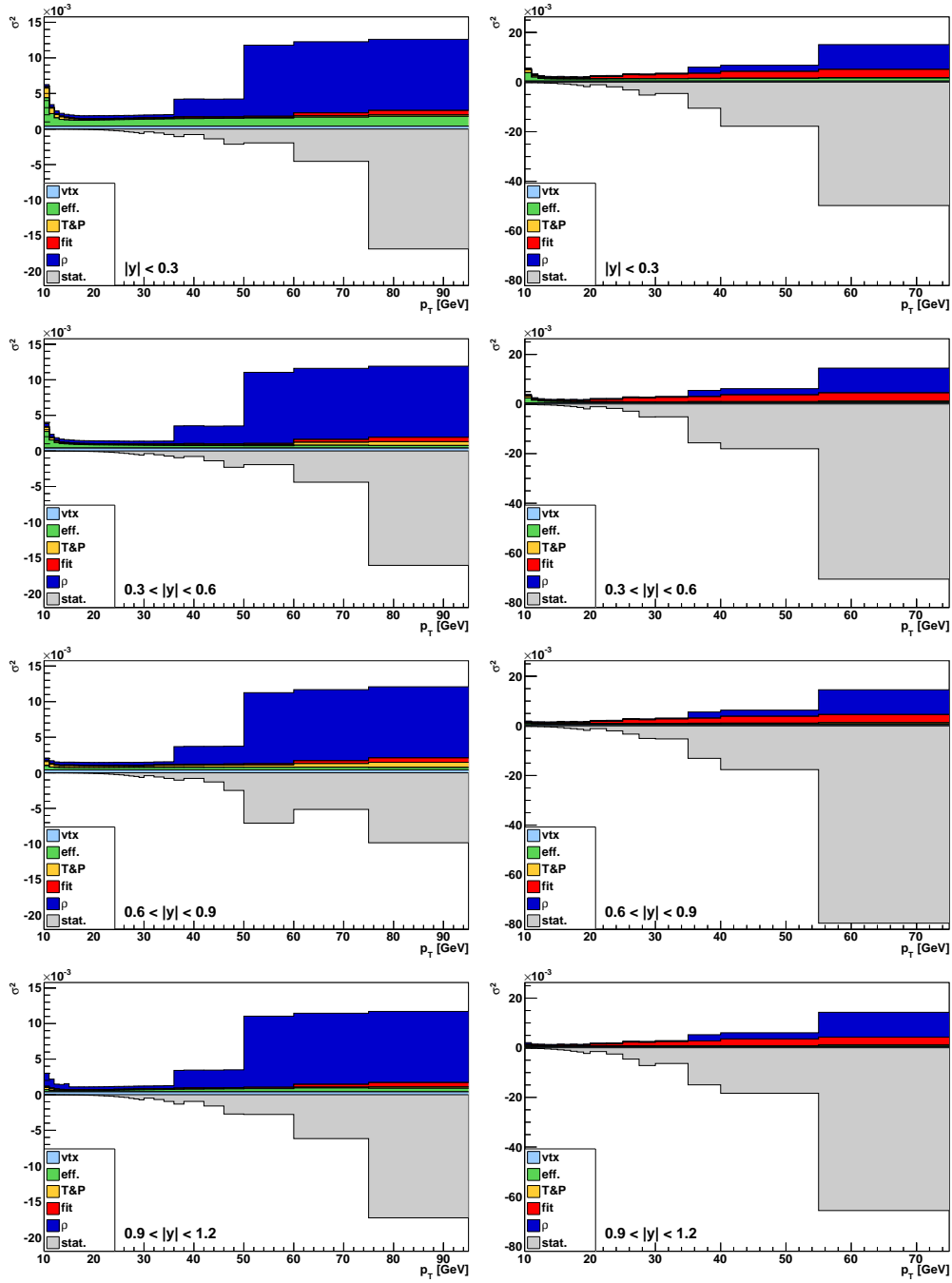


Figure 5.23: Squared systematic uncertainties displayed on the positive side and squared statistical uncertainties on the negative side, as a function of p_T in bins of $|y|$ for the J/ψ (left) and $\psi(2S)$ (right) for the four rapidity bins (top to bottom).

of the steep increase of the uncertainty on the ρ factor. The relative systematic uncertainty on the cross section times branching fraction is 11.4% and 12.6% in the highest p_T bins of the J/ψ and the $\psi(2S)$, respectively.

5.6 Results

The two-dimensional mass and pseudo-proper decay length fits described in Chapter 5.4 provide the event yield for the prompt and nonprompt charmonia as well as the continuum background for each dimuon ($p_T, |y|$) bin. To convert the prompt yields into cross sections, a correction for the efficiencies, the integrated luminosity, the acceptance and the p_T and $|y|$ bin widths needs to be applied. The integrated luminosity is slightly different for the J/ψ and the $\psi(2S)$ as already explained in Chapter 4.1: The events collected with the HLT_Dimuon13_Jpsi_Barrel_v* trigger paths are not used in the measurement of the J/ψ cross section. This leads to the small difference of 0.35 fb^{-1} in integrated luminosity: The total integrated luminosities of the analyzed samples are 4.9 fb^{-1} for the $\psi(2S)$ and 4.55 fb^{-1} for the J/ψ analysis (7.1% less).

The single muon and dimuon efficiencies as well as the acceptance are corrected for on an event-by-event basis using the weight attribution implemented in ROOFIT. Since ROOFIT does not handle errors correctly when a weighted fit is performed, the mass and pseudo-proper decay length fits are executed twice: once on the unweighted data samples to get the correct relative statistical errors on the signal yield and once on the weighted data to acquire the correct number of signal events.

The double-differential production cross sections $\mathcal{B} \times \frac{d^2\sigma}{dp_T d|y|}$ are obtained after additionally correcting the prompt signal yields (already weighted with the efficiency and acceptance correction) for the integrated luminosities, p_T and $|y|$ bin widths and the bias due to the TnP method. The final cross sections times branching fractions are shown in Fig. 5.24 for the J/ψ and $\psi(2S)$ in the four rapidity bins as well as for the integrated rapidity interval, $|y| < 1.2$. The production cross sections are essentially independent of rapidity, with only a small decrease in the most forward rapidity bin. The changes in rapidity are visualized in Fig. 5.25, where the ratios of the cross sections in each rapidity interval with respect to the ones in the bin $|y| < 0.3$ are shown. The cross sections decrease by 5% in the $0.6 < |y| < 0.9$ bin and by 15% in the most forward rapidity bin, $0.9 < |y| < 1.2$.

The numerical values of the cross section times branching ratios in the four rapidity bins as well as the ones in the $|y| < 1.2$ bin assuming isotropic decays can be found in Ref. [84]. The cross sections for $|y| < 1.2$ are also measured for three other polarization scenarios as discussed in Chapter 5.3: the two extreme scenarios $\lambda_{\psi}^{\text{HX}} = \pm 1$ and the measured values $\lambda_{\psi}^{\text{HX}} = 0.1$ and 0.03 in case of the J/ψ and the $\psi(2S)$, respectively. The scaling factors to compute the cross sections corresponding to these other polarization scenarios are also given in Ref. [84].

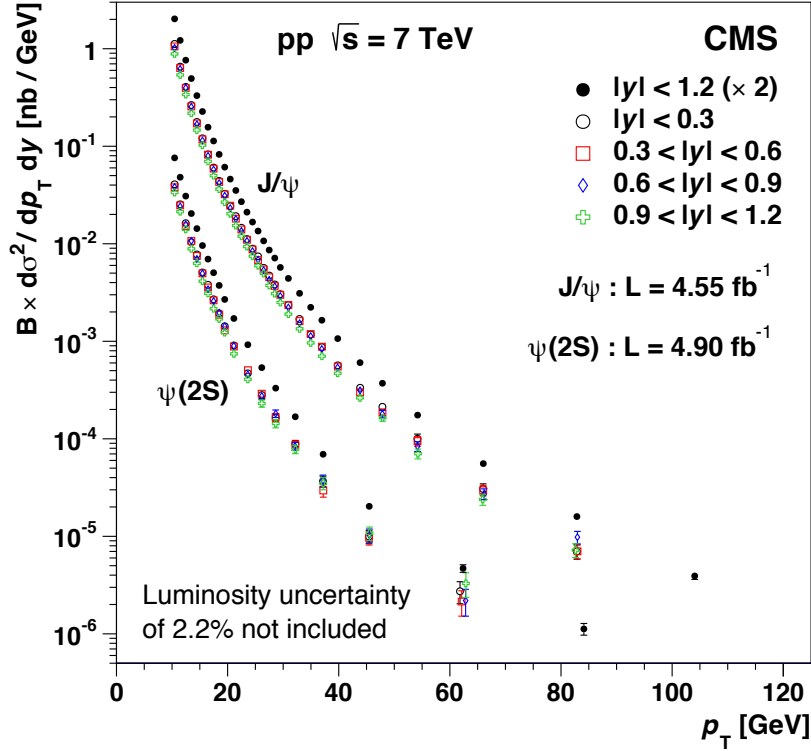


Figure 5.24: Prompt J/ψ and $\psi(2S)$ double-differential production cross sections, in the dimuon decay channel assuming no polarization, as a function of charmonium p_T for four consecutive rapidity bins. The results for the integrated rapidity bin, $|y| < 1.2$, are also depicted, scaled up by a factor of 2. The error bars represent the statistical and systematic uncertainties, added in quadrature. The global uncertainty corresponding to the integrated luminosity of 2.2% is not shown [13].

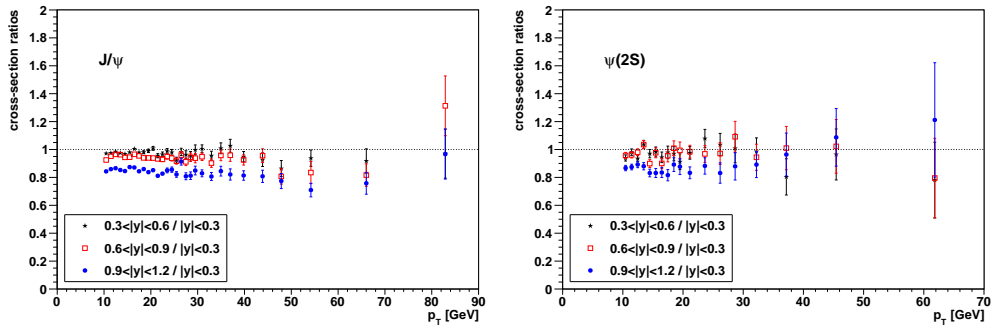


Figure 5.25: Ratios of the production cross sections measured in the different rapidity bins with respect to the rapidity interval $|y| < 0.3$ for the J/ψ (left) and $\psi(2S)$ (right).

5.6.1 Ratio of $\psi(2S)$ to J/ψ cross sections

The ratio of $\psi(2S)$ to J/ψ cross sections is also determined for $|y| < 1.2$ over the range $10 < p_T < 100$ GeV. For this measurement, the event yields of the J/ψ are recomputed in the p_T bins of the $\psi(2S)$ analysis. First, the yields of both the J/ψ and the $\psi(2S)$ are determined without any corrections from the acceptance or single muon and dimuon efficiencies since the corrections cancel to a large extent in the ratio, thus significantly reducing the systematic uncertainties. Then, independently of the yield extraction, the ratios of all corrections are calculated. The corrections to the integrated luminosity and ε_{vtx} cancel completely in the ratio over the full p_T range. The corrections due to the acceptance and the product of single muon efficiencies cancel for $p_T > 20$ GeV, but increase with decreasing p_T reaching 1.065 and 1.012 at 10 GeV, respectively, as shown in Fig. 5.26-left. The same figure shows that the correction factor ρ cancels up to $p_T = 30$ GeV in the ratio and increases afterwards with increasing p_T . It reaches 1.038 in the highest p_T bin, $75 < p_T < 100$ GeV.

The displayed correction values are affected by statistical fluctuations. Therefore, the values represented by the lines, reflecting a reasonable interpolation of the observed values, are used to correct the ratio of unweighted event yields.

The systematic uncertainties due to the acceptance, single muon efficiencies and ρ are evaluated by looking at the maximum difference between the correction ratios obtained in the four rapidity bins used in the analysis. They are added in quadrature. Figure 5.26-right shows the stacked and squared systematic uncertainties assigned to the $\psi(2S)$ over J/ψ cross section ratio.

The uncertainty on ρ dominates for $p_T > 30$ GeV, while the uncertainties due to the single muon efficiencies and the acceptance are the leading contribution for $p_T < 20$ GeV. The total uncertainties are below 3% except for $p_T > 75$ GeV, when they reach 5%.

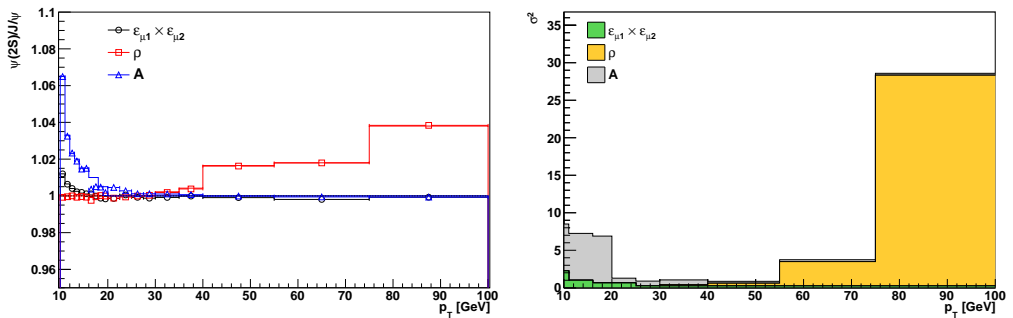


Figure 5.26: Left: Ratio of corrections from the product of single muon efficiencies ($\varepsilon_{\mu 1} \times \varepsilon_{\mu 2}$), the correction factor ρ and the acceptance \mathcal{A} as a function of p_T . Right: Stacked and squared systematic uncertainties corresponding to the product of single muon efficiencies ($\varepsilon_{\mu 1} \times \varepsilon_{\mu 2}$), the correction factor ρ and the acceptance \mathcal{A} on $\psi(2S)$ over J/ψ cross section ratio as a function of p_T .

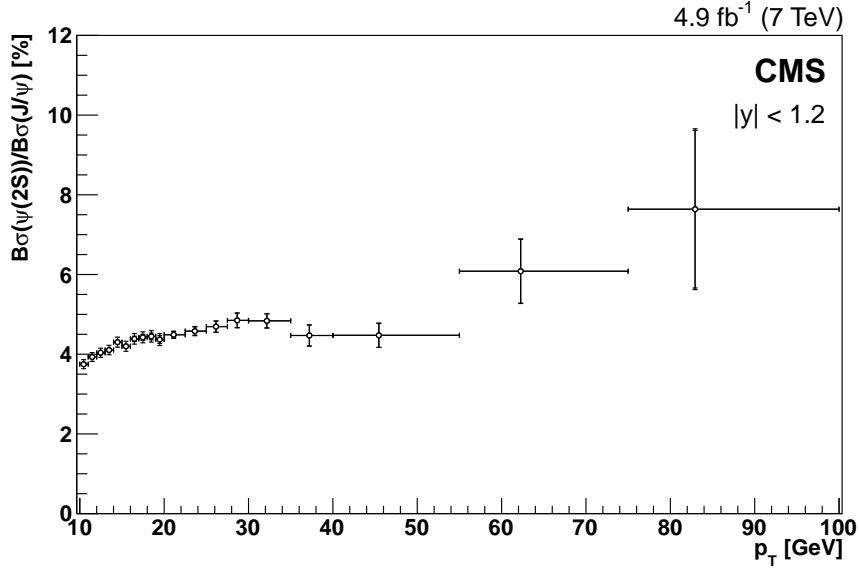


Figure 5.27: Ratio of $\psi(2S)$ to J/ψ cross section times their dimuon branching fractions as a function of p_T for $|y| < 1.2$.

Figure 5.27 shows the ratio of the $\psi(2S)$ to J/ψ cross sections times their branching fractions. The ratio increases with p_T , seemingly reaching a plateau at around 28 GeV. However, the data for $p_T > 35$ GeV is not sufficient to obtain a clear trend.

The numerical values of the $\psi(2S)$ over J/ψ cross section ratio and the corresponding statistical and systematic uncertainties are reported in Ref. [84].

CHAPTER 6

DISCUSSION OF RESULTS

Sometimes the truth is arrived at by adding all the little lies together and deducting them from the totality of what is known.

– Terry Pratchett, Going Postal

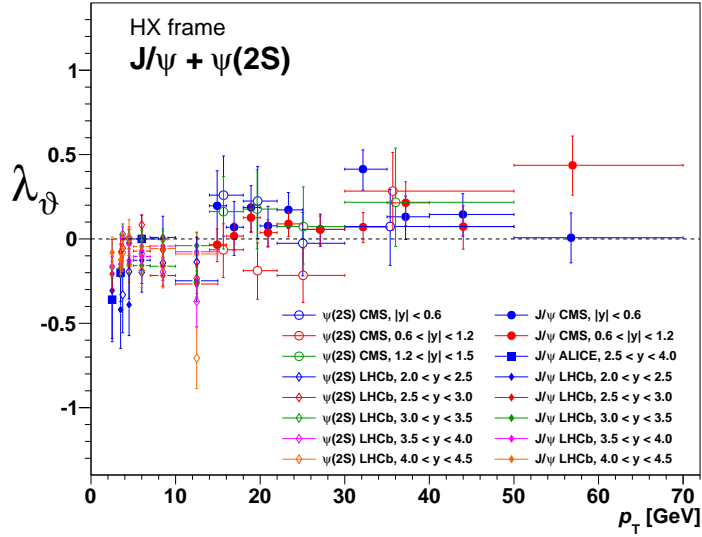
6.1 Prompt $\psi(nS)$ polarization

Three LHC experiments presented results on prompt $\psi(nS)$ polarizations: The CMS measurements in a kinematical range between 10 and 70 (50) GeV are complemented with low p_T measurements by LHCb [85, 86] and ALICE [87], as shown in Fig. 6.1. The three measurements cover very different rapidity regions, but no dependence of the polarization on the rapidity is observed.

The consistency between the results shows that all the experimental challenges and inconsistencies are finally overcome by using the technique suggested in Ref. [10].

The CMS measurements of the prompt $\psi(nS)$ polarizations made it clear that the existing Next-to-Leading Order (NLO) NRQCD predictions, such as Refs. [88, 89] based on fits to cross section data, did not describe the data. Particularly interesting is the polarization of the $\psi(2S)$ as the $\psi(2S)$ is – unlike the other S-wave quarkonium states – not affected by feed-down contributions from heavier P-wave states. Figure 6.2 shows the three polarization parameters λ_θ , λ_φ and $\lambda_{\theta\varphi}$ in comparison to the NLO NRQCD predictions made by Ref. [88]. The measured λ_θ parameters of both charmonium states are in clear disagreement with the predictions while the λ_φ and $\lambda_{\theta\varphi}$ parameters are well described by the theoretical curves. The theoretical calculations are, however, only made for directly produced charmonia. Experimentally, the directly produced charmonia

Figure 6.1: Polarization parameter λ_ϑ in the HX frame as a function of p_T for the J/ψ and $\psi(2S)$, as measured by CMS [13], LHCb [85, 86] and ALICE [87].



and those coming from feed-down decays have not been separated. Therefore, the predictions for the J/ψ may get closer to the experimental findings for the prompt polarization if the feed-down contribution is accounted for. The $\psi(2S)$ does not suffer from any feed-down, and the disagreement between experiment and theory remains.

Figure 6.3 shows the λ_ϑ parameter again in comparison to the calculations published in Ref. [88] as well two additional NLO NRQCD calculations [89, 90], which are also in disagreement with the data. The main differences between the very different predictions is the use of different datasets to obtain the LDMEs and the inclusion of feed-down contributions. Reference [88] uses hadro- as well as photoproduction data to calculate the polarization of only directly produced $\psi(nS)$'s. The authors of Refs. [89, 90] fit only the hadroproduction yield, but also consider contributions from $\psi(2S)$ and χ_c mesons. Reference [90] additionally includes the CDF polarization results [4] in the fits. All predictions have in common that they use data starting at very low p_T (> 3 GeV). The fits are therefore driven by the data at low p_T because those have the smallest uncertainties.

Recently, there has been some development in the theoretical description of quarkonium production. The Leading Power (LP) fragmentation corrections to the direct J/ψ and $\psi(2S)$ production are calculated by the authors of Ref. [91, 92]. When combining the fragmentation corrections with the perturbative corrections through NLO in α_s , a good fit to the production cross section data from CDF and CMS is obtained, as can be seen in Fig. 6.4. Only data with $p_T > 10$ GeV are used in the fit. In case of the $\psi(2S)$, the cross section measurement up to 100 GeV, which is presented in this thesis, are already included. The production cross sections are found to be dominated by the unpolarized $^1S_0^{[8]}$ channel while the sum of the contributions from the $^3S_1^{[8]}$ and $^3P_J^{[8]}$ channels, that are transversely polarized at high p_T , are small. Thus, the $\psi(nS)$'s are produced unpolarized for $p_T > 10$ GeV. This is in good agreement with the polarization

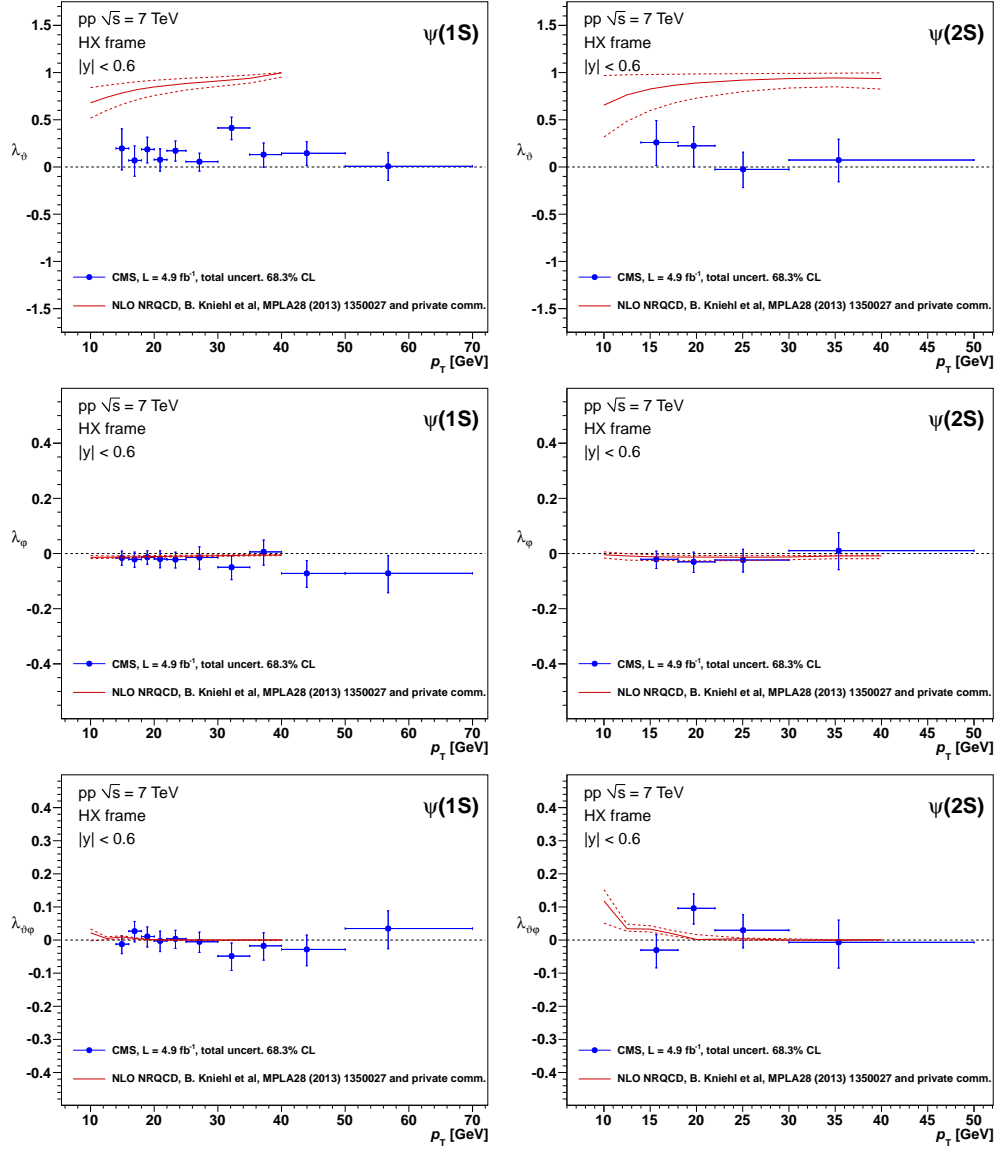


Figure 6.2: Polarization parameters λ_θ , λ_ϕ and $\lambda_{\theta\phi}$ (top to bottom) of the prompt J/ψ (left) and $\psi(2S)$ (right), measured in the HX frame as a function of the dimuon p_T , for the rapidity range $|y| < 0.6$ compared to predictions for the directly produced $\psi(nS)$ from NLO NRQCD [88]. This figure is published in Ref. [76].

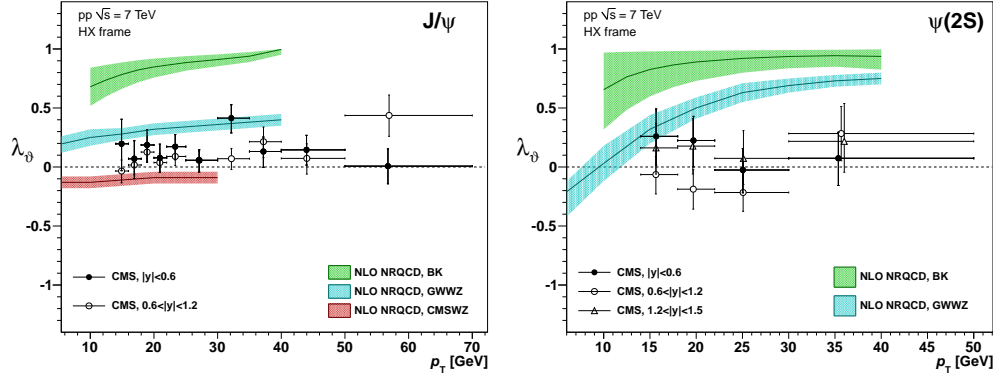


Figure 6.3: Polarization parameter λ_θ of the prompt J/ψ (left) and $\psi(2S)$ (right), measured in the HX frame as a function of the dimuon p_T , for different rapidity ranges, compared to several predictions for the $\psi(nS)$ polarization from NLO NRQCD: BK [88], GWWZ [89], CMSWZ [90].

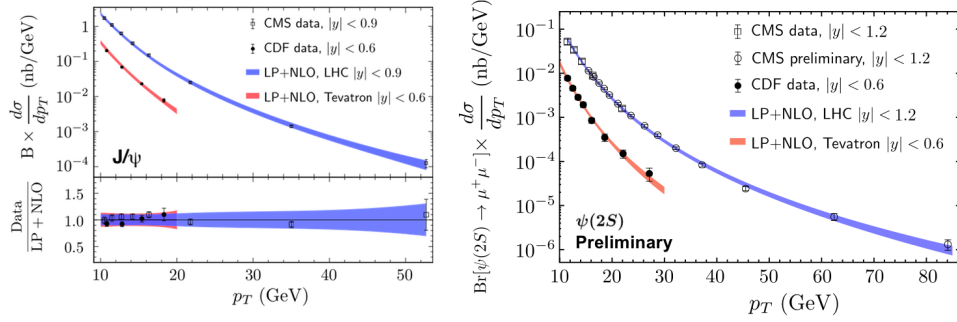


Figure 6.4: LP+NLO predictions for the J/ψ (left) and $\psi(2S)$ (right) differential production cross sections. The predictions are compared to data from CDF [2] and CMS [84, 73].

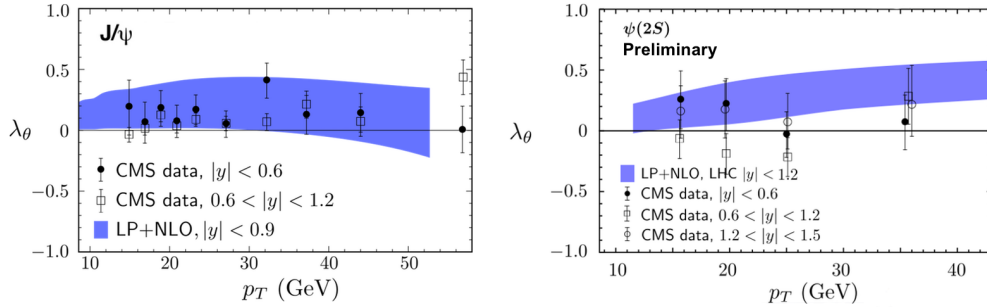


Figure 6.5: LP+NLO predictions for the polarization parameter λ_θ in the HX frame in case of the J/ψ (left) and the $\psi(2S)$ (right). The predictions are compared to data from CMS [13].

measured by CMS as is shown in Fig. 6.5. However, the prediction is made for directly produced J/ψ 's not including the feed-down contribution.

The authors of Ref. [91] also found that a fit to the production cross sections at $p_T > 10$ GeV using only NLO SDCs without the LP fragmentation corrections does not constrain the LDMEs and hence does not give a definite prediction for the polarization. The NLO NRQCD calculations from Refs. [88, 89] rely on low p_T data to constrain the LDMEs and lead to predictions of transverse polarization that are in disagreement with the measurements.

Another recent study [93] puts the focus on the polarization measurements. The authors use $\psi(2S)$ and $\Upsilon(3S)$ measurements at the LHC to perform a search for a kinematic domain where the polarization and production cross sections can be described simultaneously. By systematically scanning the phase-space and correctly taking into account the experimental uncertainties including the dependence of experimental acceptances on the polarizations, a safe kinematic domain with $p_T/m_Q > 3$ is determined. Moreover, the authors found that quarkonia are predominantly produced through the unpolarized $^1S_0^{[8]}$ channel.

The LDMEs obtained in the fit to the $\psi(2S)$ and $\Upsilon(3S)$ data in the safe kinematic domain are then used to extrapolate the predictions for the cross sections and polarizations up to higher p_T as is shown in Fig. 6.6 and 6.7. This provides predictions for future LHC measurements.

6.2 Prompt $\psi(nS)$ production cross sections

The prompt $\psi(nS)$ cross sections can be described very well by the power-law function given in Eqn. 4.3. Figure 6.8 shows that the data and the fit are in (almost) perfect agreement for both charmonium states.

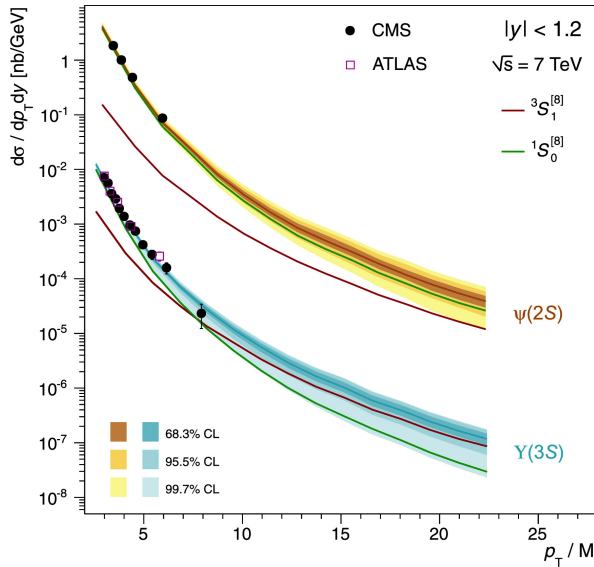


Figure 6.6: Predictions (shaded bands) for $\psi(2S)$ and $\Upsilon(3S)$ mass-scaled p_T differential cross sections extrapolated to much higher p_T than the ranges covered by the data used in the fit (black and purple dots). The partial contributions from the $^1S_0^{[8]}$, $^3S_1^{[8]}$ and $^3P_J^{[8]}$ channels are also shown [93].

Figure 6.7: Predictions (shaded bands) for $\psi(2S)$ and $\Upsilon(3S)$ mass-scaled p_T differential polarizations extrapolated to much higher p_T than the ranges covered by the data used in the fit (black and purple dots). The partial contributions from the $^1S_0^{[8]}$, $^3S_1^{[8]}$ and $^3P_J^{[8]}$ channels are also shown [93].

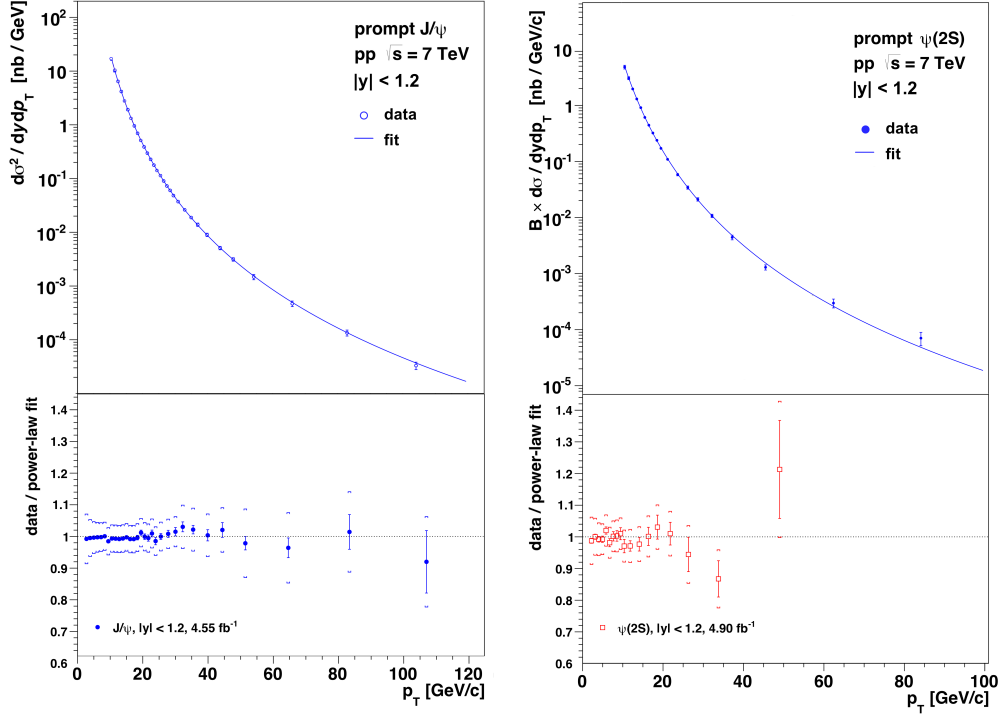
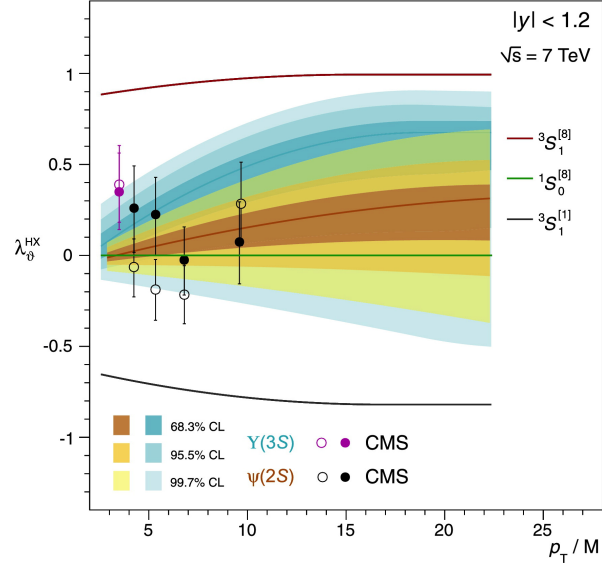


Figure 6.8: Prompt J/ψ (left) and $\psi(2S)$ (right) cross sections assuming isotropic decays as function of p_T in the $|y| < 1.2$ range, fit with a power-law function. The error bars correspond to the total uncertainties (not including the uncertainty on the luminosity), but the fit is obtained by only taking into account the statistical uncertainties since the systematic uncertainties are correlated. The ratio of the data over the power-law function is also shown. The inner error bars in the ratio correspond to the statistical uncertainties while the outer bars represent the statistical and systematic uncertainties added in quadrature, not including the global uncertainty on the luminosity (adapted from [83]).

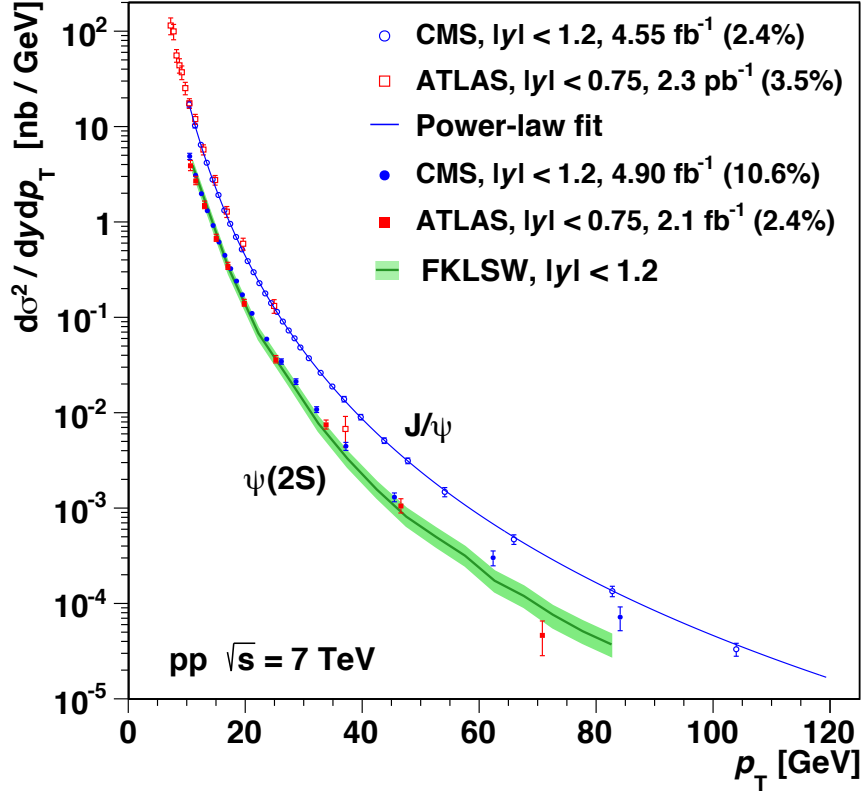


Figure 6.9: Prompt J/ψ and $\psi(2S)$ cross sections assuming isotropic decays as function of p_T in the $|y| < 1.2$ range are compared to the results of ATLAS [94, 95]. The error bars show the statistical and systematic uncertainties, added in quadrature. Global uncertainties from the integrated luminosities and branching fractions are not included, but indicated in brackets in the legend. The J/ψ cross section is fitted with a power-law function. The $\psi(2S)$ cross section is compared to a calculation using LDMEs determined with lower p_T LHC data (FKLSW) [93]. The figure is published in Ref. [84].

The CMS measurement also agrees with the result of ATLAS [94, 95] after rescaling the cross sections according to their branching fractions, as shown in Fig. 6.9. The results differ only for the highest p_T bins where the uncertainties are large.

The $\psi(2S)$ cross sections are also compared to the prediction from Ref. [93]. The prediction tends to be lower than the cross section measurement at high p_T . However, the calculation is essentially determined from cross section results with $p_T < 30$ GeV. The J/ψ and $\psi(2S)$ cross sections measured to $p_T = 120$ and 100 GeV reported in this thesis will help to further constrain the LDMEs and will thus contribute to an improved understanding of quarkonium production.

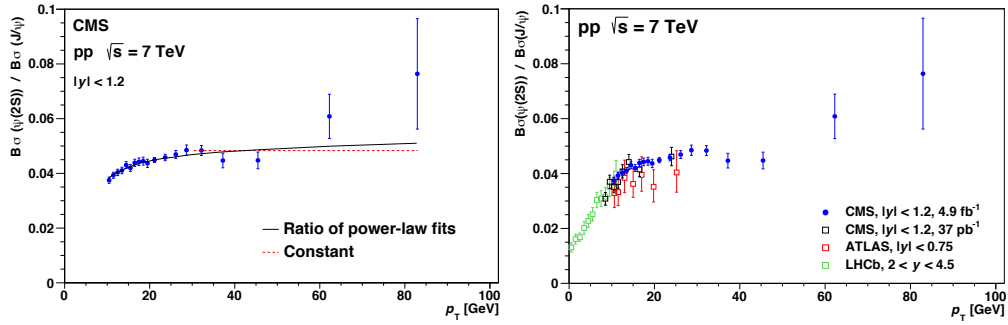


Figure 6.10: Ratio of $\psi(2S)$ to J/ψ cross sections compared to the ratio of power-law fits to the $\psi(2S)$ and J/ψ cross sections and to a constant [84] (left) and to ATLAS [94, 95], LHCb [96] and previous CMS measurements [73] (right). The ratio is not explicitly determined in these measurements, but instead it is constructed from the cross sections of the prompt J/ψ and $\psi(2S)$ mesons.

6.2.1 Ratio of $\psi(2S)$ to J/ψ cross sections

Figure 6.10-left shows the ratio of $\psi(2S)$ to J/ψ cross sections in comparison to the ratio of the power-law functions, shown in Fig. 6.8, and to a constant. Both the constant and the ratio of power-law fits describes the measurement for $p_T > 35$ GeV, given the large uncertainties. Larger data samples are needed to obtain a clear trend.

Figure 6.10-right compares the CMS results to previous measurements conducted by CMS [73], ATLAS [94, 95] and LHCb [96] where the prompt $\psi(2S)$ and J/ψ cross sections were determined. The ratio is not explicitly measured, but calculated by simply dividing the $\psi(2S)$ and J/ψ cross sections. The errors of these three ratios are therefore likely overestimated. The four ratios are in very good agreement.

6.3 Impact of the results

Apart from the prompt J/ψ and $\psi(2S)$ production cross section and polarization results presented in this thesis, CMS also measured the production cross sections and polarizations of the $\Upsilon(nS)$ states up to the highest p_T values to date. Theory relies on these measurements to obtain the LDMEs and test their polarization predictions. High p_T measurements are especially important because the NRQCD factorization approach is conjectured to hold for $p_T \gg m_Q$.

In particular, the prompt $\psi(2S)$ polarization measurement had a big impact on quarkonium physics as it showed that existing NLO NRQCD calculations are incorrect. The absence of feed-down contributions in case of the $\psi(2S)$ allows a direct comparison of the theory to data, which revealed a significant discrepancy. Also in case of the J/ψ and the $\Upsilon(3S)$ states, some deviations between the experiment and theoretical calculations were found. But these states are highly

affected by feed-down decays whose properties are experimentally not very well known. The fit to obtain the LDMEs has therefore excessive freedom to adjust to the data when the practically free feed-down contributions are included.

The proof that the existing NLO NRQCD calculations are not sufficient to describe the measured polarization triggered new developments in phenomenology and theory such as Refs.[91, 93] where the cross sections and the polarizations can be reasonably described at the same time. CMS has significantly contributed to the recent developments and thus “heads towards solving a decades-long quarkonium puzzle” [97].

CHAPTER 7

CONCLUSIONS

I may not have gone where I intended to go, but I think I have ended up where I needed to be.

– Douglas Adams, The Long Dark Tea-Time of the Soul

7.1 Summary

Quarkonium production is the ideal probe to study the formation of bound states and the long-distance strong force. Due to the slow relative velocity of the heavy quarks inside the quarkonium, the creation of the initial quark-antiquark pair and their transformation to a bound state happen at very different time scales. This conjectured factorization is used in the non-relativistic effective field theory, NRQCD, that describes quarkonium production. The NRQCD factorization approach relies on experimental input to determine the non-perturbative long-distance transformation of the initial quark pair to a bound state. The theory was very successful in describing the cross sections measured at the Tevatron, but was unable to also reproduce the measured polarizations. However, the experimental results were ambiguous and inconsistent, which diminished the impact of the large discrepancy between the measured and calculated polarizations.

In order to clarify the inconsistencies in the measurements at the Tevatron, an improved technique was put forward that makes use of all the polarization information available from data. The use of the improved technique helped to obtain consistent experimental results from the LHC detectors.

The LHC with its much higher collision energy and luminosity than the Tevatron can be regarded as a quarkonium factory. The CMS experiment at the LHC is ideally suited for polarization measurements because of its high p_T coverage and its excellent dimuon mass and decay length resolutions. Indeed, it

provides numerous results on quarkonia. In particular, the production cross sections and polarizations of all five S-wave quarkonium states were unambiguously determined by CMS up to the highest p_T values to date.

This thesis discussed the prompt J/ψ and $\psi(2S)$ production cross sections and polarizations measured by the CMS experiment at the LHC in pp collisions at $\sqrt{s} = 7$ TeV. The measurements are based on a dimuon data sample corresponding to a total integrated luminosity of 4.9 fb^{-1} . The polarization analysis determined the full angular decay distribution, i.e. the three frame-dependent polarization parameters λ_θ , λ_φ and $\lambda_{\theta\varphi}$, in three reference frames (HX, CS, PX), thus avoiding inconsistencies. Moreover, the frame-invariant quantity $\tilde{\lambda}$ was measured in the three reference frames, which does not only provide additional physical information, but also constitutes a convenient systematic check.

The polarization results are obtained in two (three) rapidity bins and extend up to $p_T = 70$ (50) GeV in case of the J/ψ ($\psi(2S)$). The measured polarization values are close to zero, showing no evidence of any strong polarization. This is in disagreement with the NLO NRQCD calculations, which predict strong transverse polarization, especially at high p_T values.

The comparison between theory and experiment is often tricky because of feed-down contributions from heavier quarkonium states that have experimentally not been separated from the directly produced quarkonia. The properties of feed-down states and their feed-down fractions have a great impact on the theoretical results, but are not very well known. A notable exception is the $\psi(2S)$ meson which is not affected by feed-down decays from heavier charmonium states. The experimental values and the theoretical predictions can therefore be directly compared. The measurement clearly showed that the NLO NRQCD calculations are incorrect and thus triggered new developments in theory.

The prompt J/ψ and $\psi(2S)$ production cross sections are determined in four equidistant rapidity bins as well as integrated in rapidity, $|y| < 1.2$. Four different polarization scenarios are considered, including two extreme, the unpolarized and a data-inspired scenario. The cross sections have been measured up to $p_T = 120$ and 100 GeV for the J/ψ and $\psi(2S)$, respectively, thereby tremendously extending the previous CMS measurements into a region where the theoretical calculations are most reliable. Moreover, the ratio of $\psi(2S)$ to J/ψ cross sections was explicitly determined. Most systematic uncertainties cancel in the ratio. The total uncertainties are therefore greatly reduced.

In summary, CMS provided production cross section measurements up to the highest p_T values to date and consistent polarization measurements for all five S-wave quarkonium states. These results have already contributed significantly to an improved understanding of quarkonium production in the scope of NRQCD and other theoretical approaches to hadron formation.

7.2 Outlook

Despite the significant theoretical and experimental progress in quarkonium production, in particular of the S-wave states, achieved in the last few years, several open issues remain. The polarization measurements of the S-wave quarkonia have to be extended to even higher p_T and conducted with higher precision, in particular the ones of the $\psi(2S)$ and $\Upsilon(3S)$ states. To disentangle effects from the directly produced quarkonia and the feed-down contributions, it is required to measure the production cross sections and polarizations of the P-wave quarkonium states. Due to the experimental difficulties in the reconstruction of low-energy photons, measurements of P-wave states are more challenging. While some results for absolute production cross sections and cross section ratios of P-wave states are already available [98, 99, 100, 101], no measurements of χ_c or χ_b polarizations have been published so far.

Only once the full set of quarkonium states in pp collisions is measured, a complete picture of the dependence of the bound state formation from all possible quantum number configurations can be obtained. It will be interesting to see if there are any significant differences between the charmonium and bottomonium states due to the different heavy quark masses.

The measurements also have to be extended to other processes as well as datasets other than pp collisions to test the conjectured universality of NRQCD. Possible studies include the measurement of the production of quarkonia in association with other particles, such as photons, the Z or W bosons. ATLAS already made a first observation of the J/ψ produced in association with Z [102] and W bosons [103].

Once the universal mechanism of quarkonium production is understood, the knowledge can be applied to other processes like $H \rightarrow J/\psi + \gamma$. This process is considered to be the golden channel for the measurement of the Higgs coupling to second generation quarks.

With the restart of the LHC this year at $\sqrt{s} = 13$ TeV, the first measurements of the polarizations of P-wave quarkonia, the determination of polarizations of S-wave quarkonia with higher precision and extended studies of the associated quarkonium production are close. Due to the excellent detector performance and the already acquired knowledge about quarkonium measurements, CMS will continue to play a driving role in the field of quarkonium physics.

BIBLIOGRAPHY

- [1] G.T. Bodwin, E. Braaten, G.P. Lepage. Rigorous QCD analysis of inclusive annihilation and production of heavy quarkonium. *Phys.Rev.*, D51:1125–1171, 1995. Erratum-ibid. D55:5853, 1997.
- [2] CDF Collaboration. Measurement of the J/ψ meson and b -hadron production cross sections in $p\bar{p}$ collisions at $\sqrt{s} = 1960$ GeV. *Phys.Rev.*, D71:032001, 2005.
- [3] CDF Collaboration. Measurement of J/ψ and $\psi(2S)$ polarization in $p\bar{p}$ collisions at $\sqrt{s} = 1.8$ TeV. *Phys.Rev.Lett.*, 85:2886–2891, 2000.
- [4] CDF Collaboration. Polarization of J/ψ and ψ_{2S} mesons produced in $p\bar{p}$ collisions at $\sqrt{s} = 1.96$ TeV. *Phys.Rev.Lett.*, 99:132001, 2007.
- [5] CDF Collaboration. Υ production and polarization in $p\bar{p}$ collisions at $\sqrt{s} = 1.8$ TeV. *Phys.Rev.Lett.*, 88:161802, 2002.
- [6] CDF Collaboration. CDF Public Note 9966. 2009.
- [7] D0 Collaboration. Measurement of the polarization of the $\Upsilon(1S)$ and $\Upsilon(2S)$ states in $p\bar{p}$ collisions at $\sqrt{s} = 1.96$ TeV. *Phys.Rev.Lett.*, 101:182004, 2008.
- [8] P. Faccioli, C. Lourenço, J. Seixas, H. Wöhri. J/ψ polarization from fixed-target to collider energies. *Phys.Rev.Lett.*, 102:151802, 2009.
- [9] P. Faccioli, C. Lourenço, J. Seixas, H. Wöhri. Towards the experimental clarification of quarkonium polarization. *Eur.Phys.J.*, C69:657–673, 2010.
- [10] P. Faccioli, C. Lourenço, J. Seixas. A new approach to quarkonium polarization studies. *Phys.Rev.*, D81:111502, 2010.
- [11] P. Faccioli, C. Lourenço, J. Seixas, H. Wöhri. Rotation-invariant observables in parity-violating decays of vector particles to fermion pairs. *Phys.Rev.*, D82:096002, 2010.
- [12] P. Faccioli, C. Lourenço, J. Seixas, H. Wöhri. Model-independent constraints on the shape parameters of dilepton angular distributions. *Phys.Rev.*, D83:056008, 2011.

- [13] CMS Collaboration. Measurement of the prompt J/ψ and $\psi(2S)$ polarizations in pp collisions at $\sqrt{s} = 7$ TeV. *Phys.Lett.*, B727:381–402, 2013.
- [14] I. Krätschmer. Understanding muon detection efficiencies for quarkonium polarization measurements at the compact muon solenoid. Master’s thesis, Vienna University of Technology, 2012.
- [15] CMS Collaboration. Muon ID performance: low- p_T muon efficiencies. *CMS-DP-2014-020*, 2014.
- [16] J.J. Aubert, et.al. Experimental Observation of a Heavy Particle J . *Phys.Rev.Lett.*, 33:1404–1406, 1974.
- [17] J.-E. Augustin, et.al. Discovery of a Narrow Resonance in e^+e^- Annihilation. *Phys.Rev.Lett.*, 33:1406–1408, 1974.
- [18] S.W. Herb, et.al. Observation of a Dimuon Resonance at 9.5 GeV in 400 GeV Proton-Nucleus Collisions. *Phys.Rev.Lett.*, 39:252–255, 1977.
- [19] K.A. Olive, et. al. (Particle Data Group). Review of Particle Physics. *Chin. Phys. C*, 38, 2014.
- [20] P. Faccioli, C. Lourenço, J. Seixas, H. Wöhri. Study of ψ' and χ_c decays as feed-down sources of J/ψ hadro-production. *JHEP*, 0810:004, 2008.
- [21] LHCb Collaboration. Study of χ_b meson production in pp collisions at $\sqrt{s} = 7$ and 8 TeV and observation of the decay $\chi_b(3P) \rightarrow \Upsilon(3S)\gamma$. *Eur.Phys.J.*, C74(10):3092, 2014.
- [22] N. Brambilla, et.al. Heavy quarkonium: progress, puzzles, and opportunities. *Eur.Phys.J.*, C71:1534, 2011.
- [23] Private Communication from P. Faccioli.
- [24] R. Baier, R. Rückl. Hadronic Collisions: A Quarkonium Factory. *Z.Phys.C*, 19:251, 1983.
- [25] E. Braaten, J. Russ. J/ψ and Υ Polarization in Hadronic Production Processes. *Ann.Rev.Nucl.Part.Sci.*, 64:221–246, 2014.
- [26] G.A. Schuler. Quarkonium production: Velocity scaling rules and long distance matrix elements. *Int.J.Mod.Phys.*, A12:3951–3964, 1997.
- [27] G.C. Nayak, J.-W. Qiu, G.F. Sterman. Fragmentation, factorization and infrared poles in heavy quarkonium production. *Phys.Lett.*, B613:45–51, 2005.
- [28] G.C. Nayak, J.-W. Qiu, G.F. Sterman. Fragmentation, NRQCD and NNLO factorization analysis in heavy quarkonium production. *Phys.Rev.*, D72:114012, 2005.
- [29] Z.-B. Kang, J.-W. Qiu, G.F. Sterman. Heavy quarkonium production and polarization. *Phys.Rev.Lett.*, 108:102002, 2012.

- [30] J.C. Collins, D.E Soper. Parton Distribution and Decay Functions. *Nucl.Phys.*, B194:445, 1982.
- [31] J.C. Collins, D.E Soper. Angular Distribution of Dileptons in High-Energy Hadron Collisions. *Phys.Rev.*, D16:2219, 1977.
- [32] E. Braaten, D. Kang, J. Lee, C. Yu. Optimal spin quantization axes for the polarization of dileptons with large transverse momentum. *Phys.Rev.*, D79:014025, 2009.
- [33] P. Faccioli, C. Lourenço, J. Seixas, H. Wöhri. Determination of χ_c and χ_b polarizations from dilepton angular distributions in radiative decays. *Phys.Rev.*, D83:096001, 2011.
- [34] E. Braaten, B. Kniehl, J. Lee. Polarization of prompt J/ψ at the Tevatron. *Phys.Rev.D*, 62:094005, 2000.
- [35] M. Butenschön, B. Kniehl. J/ψ polarization at Tevatron and LHC: Nonrelativistic-QCD factorization at the crossroads. *Phys.Rev.Lett.*, 108:172002, 2012.
- [36] P. Artoisenet, J.P. Lansberg, F. Maltoni. Hadroproduction of J/ψ and Υ in association with a heavy-quark pair. *Phys.Lett.B*, 653:60, 2007.
- [37] J.M. Campbell, F. Maltoni, F. Tramontano. QCD corrections to J/ψ and Υ production at hadron colliders. *Phys.Rev.Lett.*, 98:252002, 2007.
- [38] B. Gong, J.X. Wang. Next-to-leading-order QCD corrections to J/ψ polarization at Tevatron and Large-Hadron-Collider energies. *Phys.Rev.Lett.*, 100:232001, 2008.
- [39] B. Gong, J.X. Wang. QCD corrections to polarization of J/ψ and Υ at Tevatron and LHC. *Phys.Rev.D*, 78:074011, 2008.
- [40] B. Gong, X.Q. Li, J.X. Wang. QCD corrections to J/ψ production via color octet states at Tevatron and LHC. *Phys.Lett.B*, 673:197, 2009. Erratum-ibid. 693:612-613, 2010.
- [41] Y.Q. Ma, K. Wang, K.T. Chao. QCD radiative corrections to χ_{cJ} production at hadron colliders. *Phys.Rev.D*, 83:111503, 2011.
- [42] CMS Collaboration. Measurement of the $\Upsilon(1S)$, $\Upsilon(2S)$ and $\Upsilon(3S)$ polarizations in pp collisions at $\sqrt{s} = 7$ TeV. *Phys.Rev.Lett.*, 110(8):081802, 2013.
- [43] B. Gong, L.-P. Wan, J.-X. Wang, H.-F. Zhang. Complete next-to-leading-order study on the yield and polarization of $\Upsilon(1S, 2S, 3S)$ at the Tevatron and LHC. *Phys.Rev.Lett.*, 112(3):032001, 2014.
- [44] Y. Feng, B. Gong, L.-P. Wan, J.-X. Wang. An Updated Study for Υ Production and Polarization at the Tevatron and LHC. *arXiv:1503.08439*, 2015.

- [45] G. T. Bodwin, F. Petriello, S. Stoynev, M. Velasco. Higgs boson decays to quarkonia and the $H\bar{c}c$ coupling. *Phys.Rev.*, D88(5):053003, 2013.
- [46] T. Matsui, H. Satz. J/ψ suppression by quark-gluon plasma formation. *Phys.Lett.*, B178:416, 1986.
- [47] S. Digal, P. Petreczky, H. Satz. Quarkonium feed-down and sequential suppression. *Phys.Rev.*, D64:094015, 2001.
- [48] N. Brambilla, et. al. QCD and Strongly Coupled Gauge Theories: Challenges and Perspectives. *Eur.Phys.J.*, C74(10):2981, 2014.
- [49] L. Evans, P. Bryant (editors). LHC Machine. *JINST*, 3:S08001, 2008.
- [50] CMS Collaboration. CMS Physics Technical Design Report Volume I: Detector Performance and Software. *CERN-LHCC-2006-001*, 2006.
- [51] CMS Collaboration. CMS Physics Technical Design Report, Volume II: Physics Performance. *J.Phys.G:Nucl.Part.Phys.*, 34:995, 2007.
- [52] CMS Collaboration. The CMS experiment at the CERN LHC. *JINST*, 3:S08004, 2008.
- [53] CERN Accelerator Complex. <http://te-dep-epc.web.cern.ch/te-dep-epc/machines/pagesources/Cern-Accelerator-Complex.jpg>, Feb. 2015.
- [54] M. Lamont on behalf of the LHC team. The LHC's first long run. *CERN Courier*, 53, 2013.
- [55] LHCb Collaboration. Angular analysis of the $B^0 \rightarrow K^{*0} \mu^+ \mu^-$ decay, 2015.
- [56] ATLAS Collaboration. Observation of a new χ_b state in radiative transitions to $\Upsilon(1S)$ and $\Upsilon(2S)$ at ATLAS. *Phys.Rev.Lett.*, 108:152001, 2012.
- [57] ATLAS Collaboration. Observation of a new particle in the search for the Standard Model Higgs boson with the ATLAS detector at the LHC. *Phys.Lett.*, B716:1–29, 2012.
- [58] CMS Collaboration. Observation of a new boson at a mass of 125 GeV with the CMS experiment at the LHC. *Phys.Lett.*, B716:30–61, 2012.
- [59] CMS detector design. <http://cms.web.cern.ch/news/cms-detector-design>, Feb. 2015.
- [60] How CMS detects particles. <http://cms.web.cern.ch/news/how-cms-detects-particles>, Feb. 2015.
- [61] CMS Collaboration. *The CMS tracker system project: Technical Design Report*. Technical Design Report CMS. CERN, Geneva, 1997.
- [62] CMS Collaboration. *The CMS tracker: addendum to the Technical Design Report*. Technical Design Report CMS. CERN, Geneva, 2000.

- [63] <https://twiki.cern.ch/twiki/bin/view/CMSPublic/LumiPublicResults>, Mar. 2015.
- [64] CMS Collaboration. The CMS high level trigger. *Eur.Phys.J.*, C46:605–667, 2006.
- [65] <https://twiki.cern.ch/twiki/bin/view/CMSPublic/PhysicsResultsMUO>, Mar. 2015.
- [66] CMS Collaboration. Performance of CMS muon reconstruction in pp collision events at $\sqrt{s} = 7$ TeV. *JINST*, 7:P10002, 2012.
- [67] CMS Collaboration. Particle-Flow Event Reconstruction in CMS and Performance for Jets, Taus, and MET. *CMS-PAS-PFT-09-001*, 2009.
- [68] CMS Collaboration. Measurements of Inclusive W and Z Cross Sections in pp Collisions at $\sqrt{s} = 7$ TeV. *JHEP*, 1101:080, 2011.
- [69] CMS Collaboration. Prompt and non-prompt J/ψ production in pp collisions at $\sqrt{s} = 7$ TeV. *Eur. Phys. J. C*, 71, 2011.
- [70] D.J. Lange. The evtgen particle decay simulation package. *Nucl. Instrum. Meth.*, A462:152, 2001.
- [71] E. Barberio, B. van Eijk, Z. Was. Photos - a universal monte carlo for qed radiative corrections in decays. *Comput. Phys. Commun.*, 66:115, 1991.
- [72] E. Barberio, Z. Was. Photos - a universal monte carlo for qed radiative corrections: version 2.0. *Comput. Phys. Commun.*, 79:291, 1994.
- [73] CMS Collaboration. J/ψ and $\psi(2S)$ production in pp collisions at $\sqrt{s} = 7$ TeV. *J. High Energy Phys.*, 02:011, 2012.
- [74] HERA-B Collaboration. Kinematic distributions and nuclear effects of J/ψ production in 920 GeV fixed-target proton-nucleus collisions. *Eur. Phys. J. C*, 60, 2009.
- [75] W.K. Hastings. Monte Carlo Sampling Methods Using Markov Chains and Their Applications. *Biometrika*, 57:97–109, 1970.
- [76] CMS Collaboration. Prompt J/ψ and $\psi(2S)$ polarizations in pp collisions at $\sqrt{s} = 7$ TeV. <https://twiki.cern.ch/twiki/bin/view/CMSPublic/PhysicsResultsBPH13003>, Apr. 2015.
- [77] V. Knünz. *Measurement of Quarkonium Polarization to probe QCD at the LHC*. PhD thesis, Vienna University of Technology, 2015.
- [78] W. Verkerke and D. Kirkby. The RooFit toolkit for data modeling. *arXiv:physics/0306116*, 2003.
- [79] Minuit. <http://seal.web.cern.ch/seal/snapshot/work-packages/mathlibs/minuit/>, Mar. 2015.

- [80] M.J. Oreglia. *A study of the Reactions $\psi(2S) \rightarrow \gamma\gamma\psi$* . PhD thesis, Stanford University, 1980.
- [81] G. Punzi. Comments on likelihood fits with variable resolution. *eConf*, C030908:WELT002, 2003.
- [82] J. Mayer, K. Khairy, J. Howard. Drawing an elephant with four complex parameters. *American Journal of Physics*, 78(6):648–649, 2010.
- [83] CMS Collaboration. Prompt J/ψ and $\psi(2S)$ double-differential production cross sections in pp collisions at 7 TeV. <https://twiki.cern.ch/twiki/bin/view/CMSPublic/PhysicsResultsBPH14001>, Apr. 2015.
- [84] CMS Collaboration. Measurement of J/ψ and $\psi(2S)$ prompt double-differential cross sections in pp collisions at $\sqrt{s} = 7$ TeV. *arXiv:1502.04155*, 2015. Accepted by *Phys. Rev. Lett.* on April 13, 2015.
- [85] LCHb Collaboration. Measurement of J/ψ polarization in pp collisions at $\sqrt{s} = 7$ TeV. *Eur.Phys.J.*, C73(11):2631, 2013.
- [86] LCHb Collaboration. Measurement of $\psi(2S)$ polarisation in pp collisions at $\sqrt{s} = 7$ TeV. *Eur.Phys.J.*, C74(5):2872, 2014.
- [87] ALICE Collaboration. J/ψ polarization in pp collisions at $\sqrt{s} = 7$ TeV. *Phys.Rev.Lett.*, 108:082001, 2012.
- [88] M. Butenschön, B.A. Kniehl. Next-to-leading-order tests of NRQCD factorization with J/ψ yield and polarization. *Mod.Phys.Lett.*, A28:1350027, 2013.
- [89] B. Gong, L.-P. Wan, J.-X. Wang, H.-F. Zhang. Polarization for Prompt J/ψ and $\psi(2S)$ Production at the Tevatron and LHC. *Phys.Rev.Lett.*, 110(4):042002, 2013.
- [90] K.-T. Chao, Y.-Q. Ma, H.-S. Shao, K. Wang, Y.-J. Zhang. J/ψ Polarization at Hadron Colliders in Nonrelativistic QCD. *Phys.Rev.Lett.*, 108:242004, 2012.
- [91] G.T. Bodwin, H.S. Chung, U-R. Kim, J. Lee. Fragmentation contributions to J/ψ production at the Tevatron and the LHC. *Phys.Rev.Lett.*, 113(2):022001, 2014.
- [92] H.S. Chung. Fragmentation contributions to J/ψ production at the Tevatron and the LHC. Presented at Quarkonium 2014, CERN, Geneva, Switzerland.
- [93] P. Faccioli, V. Knünz, C. Lourenço, J. Seixas, H.K. Wöhri. Quarkonium production in the LHC era: a polarized perspective. *Phys.Lett.*, B736:98–109, 2014.
- [94] ATLAS Collaboration. Measurement of the differential cross-sections of inclusive, prompt and non-prompt J/ψ production in proton-proton collisions at $\sqrt{s} = 7$ TeV. *Nucl.Phys.*, B850:387–444, 2011.

- [95] ATLAS Collaboration. Measurement of the production cross-section of $\psi(2S) \rightarrow J/\psi(\rightarrow \mu^+ \mu^-) \pi^+ \pi^-$ in pp collisions at $\sqrt{s} = 7$ TeV at ATLAS. *JHEP*, 1409:79, 2014.
- [96] LHCb Collaboration. Updated measurements of exclusive J/ψ and $\psi(2S)$ production cross-sections in pp collisions at $\sqrt{s} = 7$ TeV. *J.Phys.*, G41:055002, 2014.
- [97] CMS heads towards solving a decades-long quarkonium puzzle. *CERN Courier*, 55, 2015.
- [98] CMS Collaboration. Measurement of the relative prompt production rate of χ_{c2} and χ_{c1} in pp collisions at $\sqrt{s} = 7$ TeV. *Eur.Phys.J.*, C72:2251, 2012.
- [99] CMS Collaboration. Measurement of the production cross section ratio $\sigma(\chi_{b2}(1P))/\sigma(\chi_{b1}(1P))$ in pp collisions at $\sqrt{s} = 8$ TeV. *Phys.Lett.*, B743:383–402, 2015.
- [100] ATLAS Collaboration. Measurement of χ_{c1} and χ_{c2} production with $\sqrt{s} = 7$ TeV pp collisions at ATLAS. *JHEP*, 1407:154, 2014.
- [101] LHCb Collaboration. Measurement of the relative rate of prompt χ_{c0} , χ_{c1} and χ_{c2} production at $\sqrt{s} = 7$ TeV. *JHEP*, 1310:115, 2013.
- [102] ATLAS Collaboration. Observation and measurements of the production of prompt and non-prompt J/ψ mesons in association with a Z boson in pp collisions at $\sqrt{s} = 8$ TeV with the ATLAS detector. *arxiv:1412.6428*, 2014. Submitted to *Eur.Phys.J.*
- [103] ATLAS Collaboration. Measurement of the production cross section of prompt J/ψ mesons in association with a W^\pm boson in pp collisions at $\sqrt{s} = 7$ TeV with the ATLAS detector. *JHEP*, 1404:172, 2014.

ACRONYMS

ALICE	A Large Ion Collider Experiment	22
APD	Avalanche PhotoDiode	27
ATLAS	A Toroidal LHC ApparatuS	22
BSM	Beyond the Standard Model	24
CB	Crystal Ball	53
CDF	Collider Detector at Fermilab	10
CERN	Conseil Européen pour la Recherche Nucléaire	21
CL	Confidence Level	50
CMS	Compact Muon Solenoid	22
CS	Collins-Soper	12
CSC	Cathode Strip Chamber	28
CSM	Color Singlet Model	9
DT	Drift Tube	28
ECAL	Electromagnetic CALorimeter	26
GCT	Global Calorimeter Trigger	30
GMT	Global Muon Trigger	30
GT	Global Trigger	30
HCAL	Hadron CALorimeter	26
HEPHY	Institute of High Energy Physics	2
HLT	High Level Trigger	30
HX	Helicity	12
L1	Level-1	30
L2	Level-2	33
L3	Level-3	34
LDME	Long-Distance Matrix Element	11
LHC	Large Hadron Collider	21

LHCb	Large Hadron Collider beauty experiment	22
LINAC2	LInear ACcelerator	21
LIP	Laboratory of Instrumentation and Experimental Particle Physics	2
LO	Leading Order	15
LP	Leading Power	102
LSB	Left SideBand	54
MC	Monte Carlo	35
MCMC	Markov Chain Monte Carlo	49
MuSclFit	Muon momentum Scale calibration Fit	82
NLO	Next-to-Leading Order	16
NNLO	Next-to-Next-to-Leading Order	11
NPSR	NonPrompt Signal Region	61
NPLSB	NonPrompt Left SideBand	61
NPRSB	NonPrompt Right SideBand	61
NR	Non Relativistic	8
NRQCD	Non Relativistic QuantumChromoDynamics	1
PDG	Particle Data Group	40
PDF	Probability Density Function	53
pp	proton-proton	19
PPD	Posterior Probability Density	49
PRSR	PRompt Signal Region	60
PRLSB	PRompt Left SideBand	61
PRRSB	PRompt Right SideBand	61
PS	Proton Synchrotron	22
PSB	Proton Synchrotron Booster	22
PU	Pile-Up	30
PX	Perpendicular Helicity	12
QCD	Quantum ChromoDynamics	8
QGP	Quark-Gluon Plasma	18
r.m.s.	root mean square	60
RPC	Resistive Plate Chamber	28
RSB	Right SideBand	54
SDC	Short-Distance Coefficient	11
SM	Standard Model	18
SPS	Super Proton Synchrotron	22
SR	Signal Region	54

TnP	Tag-and-Probe	35
TEC	Tracker EndCap	26
TIB	Tracker Inner Barrel	26
TID	Tracker Inner Disk	26
TOB	Tracker Outer Barrel.....	26
VPT	Vacuum PhotoTriode.....	27
WLS	WaveLength-Shifting.....	28

LIST OF FIGURES

2.1	Quarkonium spectra	6
2.2	Fractions of feed-down from $\chi_b(nP)$ to the $\Upsilon(nS)$ states	7
2.3	Two steps of quarkonium production	9
2.4	Prompt J/ψ and $\psi(2S)$ differential cross sections times branching ratios measured by CDF compared to CSM predictions	10
2.5	Definition of the polar and azimuthal angles	13
2.6	Definition of the production plane and the reference frames	13
2.7	Extreme angular decay distributions	14
2.8	Allowed phase-space regions of the polarization parameters	15
2.9	Measured λ_ϑ parameter for the prompt J/ψ and $\Upsilon(1S)$ states in the HX frame	16
2.10	Measured λ_ϑ parameter for the prompt J/ψ in the HX frame compared to LO and NLO NRQCD predictions	16
2.11	λ_ϑ parameter in case of the $\Upsilon(nS)$ states in the HX frame	17
2.12	λ_ϑ parameter in the HX frame compared to NLO NRQCD in case of the $\Upsilon(nS)$ states	17
2.13	Relative deviations in the branching ratio $H \rightarrow J/\psi + \gamma$ and $H \rightarrow \Upsilon(1S) + \gamma$ as function of κ_Q	19
3.1	CERN accelerator complex	22
3.2	CMS detector layout	25
3.3	Particle identification in CMS	25
3.4	Cross section of the CMS tracking system	27
3.5	Layout of one quarter of the muon system	29
3.6	Architecture of the L1 trigger	31
3.7	Invariant dimuon mass with events collected in 2010 and 2011	32
3.8	Efficiencies of three muon identification algorithms	34

3.9	Integrated luminosity	36
3.10	Average number of pp interactions	36
4.1	Distribution of single muons in the $p_T \eta $ plane	39
4.2	y - p_T distribution of the dimuon events within a $\pm 3\sigma$ mass window around the $\psi(nS)$ pole masses	40
4.3	Dimuon angular distribution for prompt J/ψ events after cuts	42
4.5	Parametrization of TnP efficiencies	45
4.6	Examples of ρ as function of $\cos\vartheta^{PX}$	47
4.7	Distribution of triggered over reconstructed J/ψ MC events in the $ \Delta\eta $ - $\Delta\varphi$ and $\Delta\varphi^{\text{elliptic}}$ - Δp_T planes	48
4.8	Contours of the two-dimensional projections of the PPD on λ_ϑ^{PX} and λ_φ^{PX} at 68.3% CL for different iterations of n_{fit}	50
4.9	Projection of the PPD on λ_ϑ (left) and λ_φ (right) in the HX frame	51
4.10	Contours of the PPD	51
4.11	Frequency distributions of the $\cos\vartheta$ and ϕ angular variables in the HX frame	52
4.12	Dimuon invariant mass distribution	54
4.13	CB parameters μ_{CB} , α_{CB} and σ_m as function of p_T and $ y $ for the J/ψ and $\psi(2S)$	55
4.14	Parameter of the background exponential λ_{BG} as function of p_T and $ y $ for the J/ψ and $\psi(2S)$	55
4.15	Relative yield of signal events contaminating the LSB and RSB regions for the J/ψ and $\psi(2S)$	56
4.16	Error distribution of the pseudo-proper decay length for the J/ψ and $\psi(2S)$	58
4.17	Pseudo-proper decay length distribution	59
4.18	B-fractions	60
4.19	r.m.s. of the parameters ℓ and L_{xy} as function of p_T and $ y $	61
4.20	Sketch of the six individual $m_{\mu\mu} - \ell$ regions	62
4.21	Fractions of prompt, nonprompt $\psi(nS)$ and continuum background events in the PRSR	62
4.22	Fractions of the prompt, nonprompt and background contributions in the NPSR	63
4.23	Parameter f_{LSB} as function of p_T and $ y $	63
4.24	Angular distributions in the PX frame of the background events in the PRSR	65
4.25	Squared systematic and statistical uncertainties for the J/ψ	69

4.26	Squared systematic and statistical uncertainties for the $\psi(2S)$. . .	70
4.27	Squared systematic and statistical uncertainties for the $\psi(2S)$ in the range $1.2 < y < 1.5$	71
4.28	Differences between the $\tilde{\lambda}$ parameters in the different reference frames	72
4.29	Frame-invariant $\tilde{\lambda}$ parameter in the HX frame	72
4.30	Polarization parameters in the HX frame	73
5.1	Efficiency ε_{vtx} as a function of p_{T}	77
5.2	Correction factor ρ as a function of p_{T}	77
5.3	J/ψ and $\psi(2S)$ acceptance for different polarization scenarios . . .	78
5.4	J/ψ and $\psi(2S)$ acceptance for two rapidity intervals	79
5.5	Expected mean of the CB function, μ_{CB} , as function of p_{T}	82
5.6	CB function with different sets of $(\alpha_{\text{CB}}, n_{\text{CB}})$ parameters	82
5.7	Slopes of the left-sided and double-sided exponentials describing the pseudo-proper decay length distribution of the background dimuons for the J/ψ	83
5.8	Slopes of the left-sided and double-sided exponentials describing the pseudo-proper decay length distribution of the background dimuons for the $\psi(2S)$	84
5.9	Mass and pseudo-proper decay length fit in the bin $30 < p_{\text{T}} < 32$ GeV and $0.6 < y < 0.9$ for the J/ψ	84
5.10	Mass and pseudo-proper decay length fit in the $22 < p_{\text{T}} < 23$ GeV and $ y < 0.3$ for the $\psi(2S)$	85
5.11	B-fractions	86
5.12	Dimuon mass resolution	86
5.13	Dimuon pseudo-proper decay length resolution	86
5.14	Mass and pseudo-proper decay length fit in the bin $21 < p_{\text{T}} < 22$ GeV and $ y < 1.2$ for the J/ψ	88
5.15	Mass and pseudo-proper decay length fit in the bin $12 < p_{\text{T}} < 13$ GeV and $ y < 1.2$ for the $\psi(2S)$	89
5.16	Systematic uncertainties on the extraction of the prompt signal yield	91
5.17	Systematic uncertainty due to the TnP approach	92
5.18	Mean of the inverse of the average dimuon efficiency when changing the parametrization parameters	92
5.19	Systematic uncertainty due to the parametrization of efficiencies .	93
5.20	Absolute value of the difference between the value of ρ evaluated on MC and unity	93

5.21	Correction factor ρ evaluated on data and its relative difference to ρ evaluated on MC	94
5.22	Statistical and systematic uncertainties	95
5.23	Statistical and systematic uncertainties	96
5.24	Prompt $\psi(nS)$ production cross sections in the dimuon decay channel	98
5.25	Ratios of the charmonium cross sections measured in the different rapidity bins	98
5.26	Ratio of corrections and the systematic uncertainties on the $\psi(2S)$ over J/ψ cross section ratio	99
5.27	Ratio of $\psi(2S)$ to J/ψ cross section times their dimuon branching fractions	100
6.1	Parameter λ_ϑ as measured by CMS, LHCb and ALICE	102
6.2	Comparison of the measured polarization parameters in the HX frame with NLO NRQCD predictions	103
6.3	Comparison of the measured λ_ϑ in the HX frame with different NLO NRQCD predictions	104
6.4	LP+NLO predictions for the J/ψ and $\psi(2S)$ differential production cross sections	104
6.5	LP+NLO predictions for the polarization parameter λ_ϑ^{HX} in case of the J/ψ and $\psi(2S)$	104
6.6	Predictions for $\psi(2S)$ and $\Upsilon(3S)$ mass-scaled p_T differential cross sections	105
6.7	Predictions for $\psi(2S)$ and $\Upsilon(3S)$ mass-scaled p_T differential polarizations	106
6.8	J/ψ and $\psi(2S)$ cross sections fitted with a power-law function . .	106
6.9	J/ψ and $\psi(2S)$ cross sections compared to results from ATLAS .	107
6.10	Ratio of $\psi(2S)$ to J/ψ cross sections compared to the ratio of power-law fits and a constant and other LHC measurements. . . .	108

LIST OF TABLES

2.1	Properties of quarkonium mesons	8
3.1	LHC parameters during Run I and their design values	23
5.1	Parameters of the dimuon mass and pseudo-proper decay length fit	81

CURRICULUM VITAE

CONTACT: ilse.kraetschmer@gmx.at

EDUCATION

- 2012–
present **Doctoral program in Engineering Sciences**, *Vienna University of Technology*, Austria
- 2005–2012 **Diploma program in Technical Physics**, *Vienna University of Technology*, Austria, passed with distinction
Degree Dipl.-Ing./M.Sc. obtained in April 2012
Diploma thesis: Understanding Muon Detection Efficiencies for Quarkonium Polarization Measurements at the Compact Muon Solenoid.
Supervisors: Univ. Prof. Dipl.Ing. Dr. Christian Fabjan, Dr. Josef Strauss & Dipl.Ing. Dr. Hermine Wöhri
- 2008-2009 **Erasmus program**, *University of Linköping*, Sweden
Exchange student in physics
- 2003–2005 **College for printing technique and media management**, *Höhere Graphische Bundes- Lehr- und Versuchsanstalt Wien XIV*, Austria, passed with distinction
Degree obtained in September 2005
Thesis: Messungen von Siebdruck- und Digitaldruckfarben auf diversen Bedruckstoffen in Bezug auf Lichtechtheit zur Erstellung einer Kundengarantie.
Supervisors: Andreas Galehr & Prof. Mag. Karl Olbrich
- 1995–2003 **Secondary school**, *Bundesgymnasium Tamsweg*, Austria, passed with distinction
General qualification for university entrance obtained in June 2003

EXPERIENCE

RESEARCH

- 2012–
present **Research for doctoral thesis**, *Institute of High Energy Physics*, Vienna, Austria
Research on the spin alignment (polarization) and production of quarkonia to probe quantum chromodynamics with the CMS experiment at the Large Hadron Collider
- 2011–2012 **Research for diploma thesis**, *Institute of High Energy Physics*, Vienna, Austria
Research on the spin alignment (polarization) of quarkonia with special focus on the determination and understanding of muon detection efficiencies
- 2010–2012 **Project work**, *CNGS, CERN*, Geneva, Switzerland
Performance analysis of the CERN Neutrinos to Gran Sasso project conducted each year in December
- 2010 **Summer internship**, *CNGS, CERN*, Geneva, Switzerland
Performance analysis of the CERN Neutrinos to Gran Sasso project
- 2010 **Project work**, *Institute for Quantum Optics and Quantum Information*, Vienna, Austria
Direct coupling of a fiber tip to PPKTP waveguides
- 2010 **Project work**, *ATLAS, CERN*, Geneva, Switzerland
Work on the ATLAS Beam Conditions Monitor
- 2009 **Project work**, *University of Linköping*, Sweden
Characterization of black polymer solar cells

TEACHING

- 2014 **Co-supervision of a master student**, *Institute of High Energy Physics*, Vienna, Austria
- 2010–2011, **Tutor**, *Vienna University of Technology*, Austria
2008 Teaching of the exercise “Experimental Exercises in Physics”
- 2008 **Tutor**, *Vienna University of Technology*, Austria
Teaching of the exercise “Basic Principles of Physics II”

MANAGEMENT

- End 2013 **BPH muon contact**
- Mar. 2015 Muon object expert, contact between the CMS B-physics and quarkonia group and the muon physics object group

- End 2013 **BPH efficiency trigger contact**
–Mar. 2015 Object expert for trigger especially designed for measuring efficiencies

MISCELLANEOUS

- 2007 **Summer internship, Infineon, Villach, Austria**
 Work placement in the process management of a sensor for pressure
- 2004–2007 **Miscellaneous summer internships and jobs, Austria**

AWARDS

- 2014 Nuclear Physics B/Physics Letter B Young Scientist Award (2nd prize) awarded for the best poster “Muon reconstruction and identification in CMS Run I and towards Run II” at the *37th International Conference on High Energy Physics*, Valencia, Spain
- 2011 Award for the most artistic poster “Towards the Measurement of Quarkonium Polarization” at the *CMS Physics Week*, Brussels, Belgium

SELECTED LIST OF PUBLICATIONS

I. Krätschmer for the CMS Collaboration. Quarkonium production measurements and searches for exotic quarkonia at CMS. *J. Phys.: Conf. Ser.* 556:012012, 2014.

CMS Collaboration. Measurement of J/ψ and $\psi(2S)$ prompt double-differential cross sections in pp collisions at $\sqrt{s} = 7$ TeV. Accepted by *Phys. Rev. Lett.*, April 13, 2015.

I. Krätschmer for the CMS Collaboration. Measurements of Quarkonium production and polarization at CMS. *Proceedings of the European Physical Society Conference on High Energy Physics*, PoS(EPS-HEP 2013) 437.

CMS Collaboration. Measurement of the prompt J/ψ and $\psi(2S)$ polarizations in pp collisions at $\sqrt{s} = 7$ TeV. *Phys. Lett. B* 727:381, 2013.

CMS Collaboration. Measurement of the $\Upsilon(1S)$, $\Upsilon(2S)$ and $\Upsilon(3S)$ polarizations in pp collisions at $\sqrt{s} = 7$ TeV. *Phys. Rev. Lett.*, 110:081802, 2013.

I. Krätschmer for the CMS and CDF Collaborations. $\Upsilon(nS)$ Polarization Results: Summary from CMS and CDF. *Proceedings of 14th International Conference on B-Physics at Hadron Machines*, PoS(Beauty2013) 017.

I. Krätschmer for the CMS Collaboration. $\Upsilon(nS)$ polarization in pp collisions at the LHC with the CMS experiment. *Nucl. Phys. Proc. Suppl.* 234, 2013.

E. Gschwendtner, et al. CNGS, CERN Neutrinos to Gran Sasso, Five Years of Running a 500 Kilowatt Neutrino Beam Facility at CERN. *Proceedings of the 4th International Particle Accelerator Conference*, MOPEA058, 2013.

Yi Zhou, et al. Black Polymers in Bulk-Heterojunction Solar Cells. *JSTQE*, Vol. 16, No. 6, 2010.

CONFERENCE CONTRIBUTIONS

TALKS

Quarkonium production and polarization in pp collisions with the CMS detector. Presented at *Kruger2014: Third Biennial Workshop on Discovery Physics at the LHC*, 1-6 December 2014, Skukuza, South Africa.

Quarkonium polarization measurements with CMS. Presented at *Quarkonium 2014: 10th International Workshop on Heavy Quarkonium 2014*, 10-14 November 2014, CERN, Geneva, Switzerland.

Quarkonium production measurements and searches for exotic quarkonia at CMS. Presented at the *XI International Conference on Hyperons, Charm and Beauty Hadrons*, 21-26 July 2014, Birmingham, United Kingdom.

Measurements of Heavy Flavour Properties at ATLAS and CMS. Presented at the *26th Rencontre de Blois - Particle Physics and Cosmology*, 18-23 May 2014, Blois, France.

Quarkonium production and polarization in pp collisions with the CMS detector. Presented at the *Lake Louise Winter Institute*, 16-22 February 2014, Lake Louise, Canada.

Measurement of Quarkonium Production and Polarization at CMS. Presented at the *European Physical Society Conference on High Energy Physics*, 18-24 July 2013, Stockholm, Sweden.

$\Upsilon(nS)$ Polarization Results from CMS and CDF. Presented at the *14th International Conference on B-Physics at Hadron Machines*, 8-12 April 2013, Bologna, Italy.

Measurement of $\Upsilon(nS)$ Polarization with CMS. Presented at the *62nd Annual Meeting of the Austrian Physical Society Meeting*, 18-21 September 2012, Graz, Austria.

Measurement of Quarkonium Polarization with the CMS experiment. Presented at the *16th International Conference in Quantum Chromodynamics*, 2-7 July 2012, Montpellier, France.

Challenges and Perspectives in Quarkonium Polarization Measurements. Presented at the *Nordic Conference of Particle Physics: Spatind 2012*, 2-7 January 2012, Skeikampen, Norway.

POSTERS

Muon reconstruction and identification in CMS Run I and towards Run II. Presented at the *37th International Conference on High Energy Physics*, 2-9 July 2014, Valencia, Spain.

Measurement of Prompt $\psi(2S)$ Polarization With CMS or The Tale of Psi Prime. Presented at the *2013 European School of High Energy Physics*, 5-18 June 2013, Parádfürdő, Hungary.

Towards the Measurement of Quarkonium Polarization. Presented at the *CMS Physics Week*, 11-15 September 2011, Brussels, Belgium.